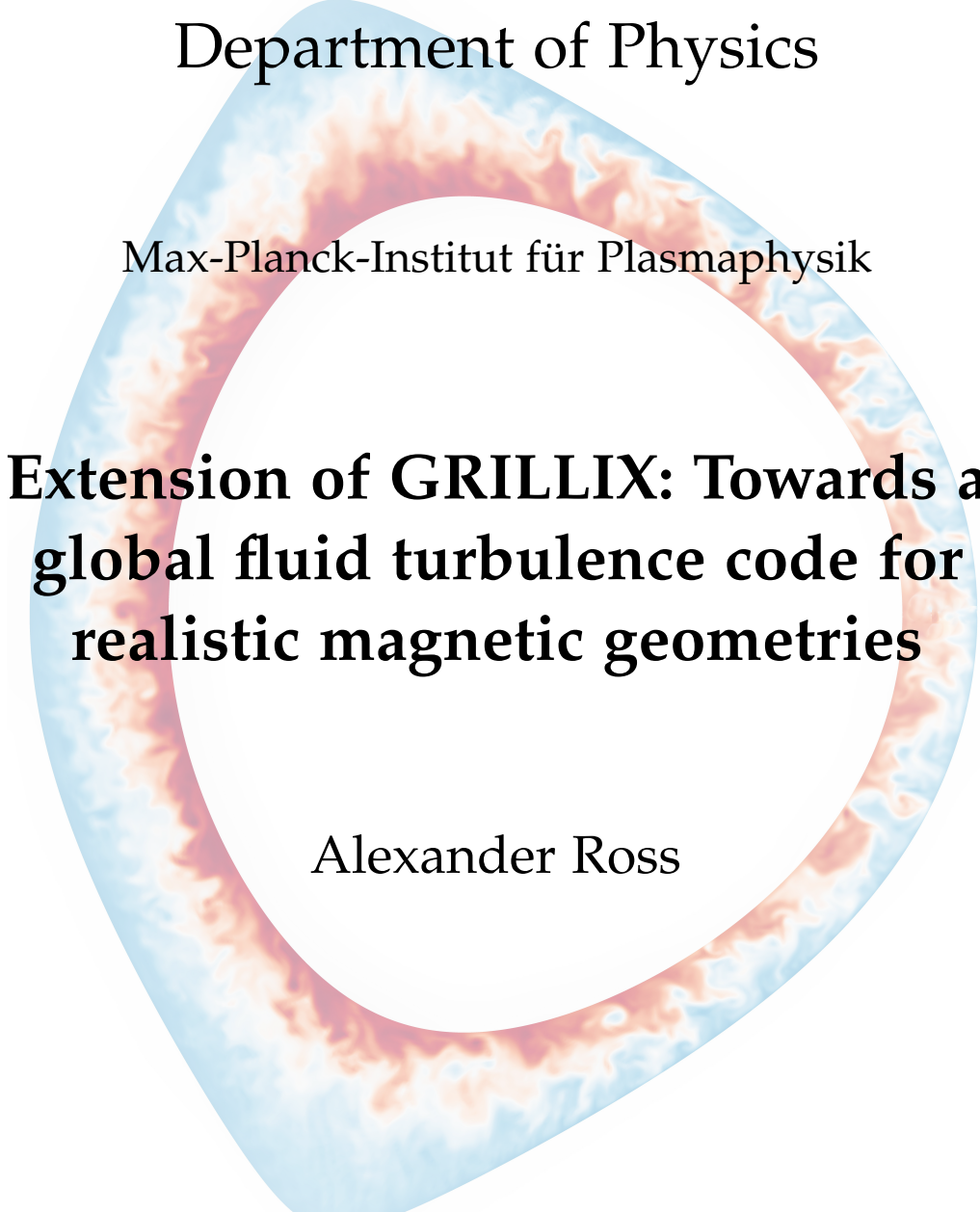




TECHNISCHE UNIVERSITÄT MÜNCHEN

Department of Physics

Max-Planck-Institut für Plasmaphysik

A large, stylized ring-shaped visualization of a plasma ring, showing turbulent structures in shades of blue, orange, and red, serving as a background for the central text.

**Extension of GRILLIX: Towards a
global fluid turbulence code for
realistic magnetic geometries**

Alexander Ross





Technische Universität München

Max-Planck-Institut für Plasmaphysik

Extension of GRILLIX: Towards a global fluid turbulence code for realistic magnetic geometries

Alexander Ross

Vollständiger Abdruck der von der Fakultät für Physik der Technischen Universität München zur Erlangung des akademischen Grades eines Doktors der Naturwissenschaften genehmigten Dissertation.

Vorsitzender:

Prof. Dr. Stephan Paul

Prüfer der Dissertation:

1. Hon.-Prof. Dr. Sibylle Günter
2. Prof. Dr. Martin Zacharias

Die Dissertation wurde am 14.08.2018 bei der Technischen Universität München eingereicht und durch die Fakultät für Physik am 16.10.2018 angenommen.

ABSTRACT

In order to understand the physics in the scrape-off layer (SOL) of tokamaks and simulate the turbulent cross field transport, numerical codes have become an important tool. The simulation of the edge and SOL poses a major challenge, due to the complex physics and geometry. The widely used field or flux-aligned coordinate systems become ill defined at the X-point and separatrix of a tokamak. The solution to this issue was presented with the plasma turbulence code GRILLIX, which uses a flux-coordinate independent approach (FCI), enabling the simultaneous simulation of the closed and open field line region. A cylindrical grid is used, posing no singularities at the X-point and separatrix. Parallel operators are discretized via a field line map along a field line. Moreover the Cartesian grid within each poloidal plane allows an efficient and consistent simulation of the plasma turbulence.

The functionality of the FCI approach was demonstrated within the simple Hasegawa-Wakatani plasma turbulence model. However this model is not suited for the simulation of the complex physics in the SOL. In this work the turbulence simulation efforts within the FCI approach are taken to further depth. The drift-reduced Braginskii model, which is more suited for the SOL, is implemented in GRILLIX. Along this line, the focus is on the consistent and tested implementation of a global electrodynamic model, finally posing a solid and reliable foundation for further development of GRILLIX and turbulence simulations. In this context 'global' means, that nowhere in the model any assumptions about the density and temperature fluctuations amplitude are made. For this goal, many subtle points regarding the widely used Boussinesq approximation, which was relaxed in this thesis, conservation properties of the model and electromagnetic dynamics are considered. In order to reduce the complexity, firstly simulations are performed within a simplified slab geometry, where also a comparison to experimental turbulence data from LAPD device was possible. Finally it helped to perform the transition to more realistic and complex geometries, where the FCI approach shows successfully its capabilities.

ZUSAMMENFASSUNG

Für das Verständnis der Plasma Abschältschicht in Tokamaks und des turbulenten Transports sind numerische Programme immer wichtiger geworden. Die Simulation des Plasmarands und Abschältschicht stellt wegen der komplexen Physik und Geometrie eine große Herausforderung dar.

Die häufig benutzten Feldlinien-angepassten Koordinatensysteme sind am X-Punkt und der Separatrix singularär. Die Lösung dieses Problems wurde mit dem Plasmaturbulenz-Simulationsprogramm GRILLIX präsentiert, welches einen feldlinienunabhängigen Ansatz benutzt, was eine gleichzeitige Simulation der offenen und geschlossenen Feldlinien ermöglicht. Es wird ein zylindrisches Gitter benutzt, wo keine Singularitäten am X-Punkt und der Separatrix auftreten. Parallele Operatoren werden entlang einer Feldlinie diskretisiert. Es wird ein kartesisches Gitter in jeder poloidalen Ebene benutzt, was eine effiziente und konsistente Simulation der Plasmaturbulenz ermöglicht.

Die Funktionalität des feldlinienunabhängigen Ansatzes wurde mit einem einfachen Hasegawa-Wakatani Plasmaturbulenz-Modell demonstriert. Dieses Modell ist jedoch nicht geeignet, die komplexe Physik in der Abschältschicht zu simulieren. In dieser Arbeit werden die Turbulenz-Simulationen mit dem feldlinienunabhängigen Ansatz auf eine neue Stufe gestellt. Das drift-reduzierte Braginskii-Modell, was sich für die Simulation der Abschältschicht mehr eignet, wurde in GRILLIX implementiert. Dahingehend liegt der Fokus auf einer konsistenten und getesteten Implementierung des globalen elektromagnetischen Modells, was am Ende eine solide und verlässliche Grundlage für weitere Entwicklungen von GRILLIX und Turbulenz-Simulationen darstellt. In diesem Kontext bedeutet 'global', dass keine Annahmen im System über die Fluktuationsamplituden der Dichte und Temperatur gemacht worden sind. Für dieses Ziel mussten viele subtile Punkte beachtet werden, betreffend die Boussinesq Näherung, die in dieser Arbeit abgeschafft wurde, Erhaltungseigenschaften des Modells und elektromagnetische Dynamik. Um die Komplexität zu reduzieren, wurden die Simulationen zunächst in einer vereinfachten Slab-Geometrie durchgeführt, was auch einen Vergleich mit experimentellen Turbulenzdaten von LAPD erlaubte. Schließlich half es zu komplexeren Geometrien zu gehen, wo der feldlinienunabhängiger Ansatz seine Möglichkeiten erfolgreich zeigt.

ACKNOWLEDGEMENTS

First of all I want to thank Andreas Stegmeir, David Coster and Sibylle Günter for advice and help. The door of Andreas Stegmeir's office was always open for me. He could always help with his deep understanding of the physics and the techniques of the project. Through discussions and meetings with him, I was able to stay motivated and focused even in the hardest phases (I call the time around Christmas 2016 now ironically 'Christmas of my life'). Moreover, he has created a supportive atmosphere, which makes the work with him extremely valuable in a personal and professional way. David Coster always contributed to the project with his experienced and pragmatic view. Sibylle Günter gave me the freedom to pursue the scientific goals of the project.

Furthermore I want to thank Peter Manz. He often changed my perspective and could provide rich physical insights. Many thanks to Bruce Scott for the discussions about the important aspects of the model. I want to cordially thank Frank Jenko for his belief in the project, which motivated all participants in many ways.

Special thanks go to my office mates Ivan Erofeev and Thomas Body. The fruitful discussions with Ivan often changed my perspective on physical aspects. Thanks to Thomas, I could improve the quality of my English writing.

Finally, I thank my wife Oxana Ross. She strongly supported and encouraged me during difficult phases of my work ('in good times and in bad' can be tested during a PhD). Of course, I thank my family, that made this path possible for me and provided priceless support.

CONTENTS

1	THE PATH TO A VIRTUAL TOKAMAK	1
1.1	Tokamak	1
1.2	Scrape-off layer and power exhaust	3
1.3	Modeling the edge and SOL	6
1.4	GRILLIX	9
1.5	Motivation and outline	13
2	MODEL AND IMPLEMENTATION	15
2.1	Braginskii equations	16
2.2	Standard simplifications	19
2.3	Drift Approximation	19
2.4	Drift reduced equations	23
2.5	Energy conservation	25
2.6	Debye Sheath boundaries	26
2.7	Additional simplification and its implications	30
2.7.1	New advective derivative	30
2.7.2	Boussinesq approximation	30
2.8	Numerical implementation	34
2.8.1	Geometry	34
2.8.2	Normalization	36
2.8.3	Sources, Dissipation and radial boundary conditions	38
2.8.4	Discretization	38
2.8.5	Time-Stepping scheme	43
2.8.6	Helmholtz solver	43
2.8.7	Method of manufactured solutions	45
3	SIMULATIONS IN SLAB GEOMETRY	49
3.1	Blob dynamics	50
3.1.1	Qualitative blob dynamics	54
3.1.2	Scaling with the width	57
3.1.3	Scaling with the amplitude	59
3.1.4	Impact of the Boussinesq approximation	62
3.2	Turbulence on closed field lines	65
3.2.1	Alfvén dynamics	65
3.2.2	Conservation properties	72
3.3	Large plasma device (LAPD)	80
3.3.1	LAPD experiment	81

3.3.2	Dominant Instabilities	82
3.3.3	Modeling	84
3.3.4	Validation	85
4	FLUX-COORDINATE INDEPENDENT APPROACH	93
4.1	Discretization	94
4.2	Geometries	96
4.3	Simulation and Diagnostics	99
5	SUMMARY, CONCLUSIONS AND OUTLOOK	114
5.1	Summary and conclusions	114
5.2	Outlook	116
5.3	Conclusion	118
	Bibliography	119

THE PATH TO A VIRTUAL TOKAMAK

In order to prepare for ITER (International Thermonuclear Experimental Reactor)¹ operation, interpret the future results and facilitate the design of future fusion power plants like DEMO (DEMONstration Power Plant)², the plasma community needs to perform the transition from postdiction to prediction. For this aim interdisciplinary efforts between physics, computer science, mathematics and engineering are crucial, and there exists a consensus that the creation of a virtual fusion plasma is of great importance for the future of fusion energy research. Such a virtual fusion plasma needs to have *reliable*, *validated* and *predictive* capabilities. In fact, the tokamak concept has proven to be a promising candidate for plasma confinement and future power plants. Consequently, the creation of a virtual tokamak is necessary.

1.1 TOKAMAK

A plasma consists of free charged particles (electrons and ions) and needs to be insulated against thermal losses in order to establish and sustain a fusion reaction. In contrast to the sun where gravity confines the particles, on earth magnetic fields are used to confine a plasma.

A charged particle in a magnetic field is subject to the Lorentz force which leads to a helical orbit around the magnetic field line of the particle. It means that the particle is still allowed to stream freely along the magnetic field lines, but the motion in the perpendicular plane is constrained to the helical trajectory. This leads to the idea of magnetic plasma confinement where particles are confined along the magnetic field lines. Compared to other magnetic configurations the tokamak has proven to be the most successful one. Another promising candidate is the Stellarator c.f. Wendelstein 7-X [1].

-
- 1 ITER is a research tokamak, which is currently under construction in Cadarache, France. First hydrogen plasma is planned for the year 2025. The reactor is planned to show a higher electrical energy output compared to the energy input.
 - 2 DEMO is the successor of ITER. It is planned to produce electrical energy for the power grid. Moreover, the reactor is planned to demonstrate a closed tritium circle.

In a tokamak configuration the particles are confined in the parallel direction by closing the magnetic field lines in toroidal direction. The toroidal magnetic field is created by a set of planar magnetic coils, see figure 1.1.1.

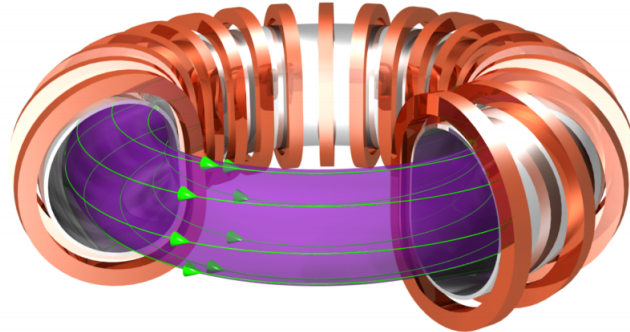


Figure 1.1.1: Toroidal magnetic field (green) produced by centric ordered coils [2].

However, the confinement properties of such a configuration are quite poor. The reason is the inhomogeneity of the toroidal magnetic field $B_{tor} \propto R^{-1}$, where R is the radial distance from the symmetry axis of the machine. The magnetic field strength is maximum in the machine close to the symmetry axis. This region is called the High Field Side (HFS). Consequently the region at the outboard of the torus is called the Low Field Side (LFS). In combination with the curvature of the magnetic field lines, a vertical drift is created. The direction of this drift depends on the charge of the particles. It means that electrons and ions drift in opposite directions, which leads to a charge separation. Consequently an electric field is created, which causes an additional radial drift for both species. This leads to a loss of the plasma confinement. The solution of this issue is an additional magnetic field in the poloidal direction, induced by the toroidal electric current, see figure 1.1.2. The toroidal current is induced via the principle of a transformer, where the secondary winding is the plasma column. In the primary winding (poloidal coils) a rising current needs to flow in order to maintain a constant toroidal current subject to a finite resistivity of the plasma. Therefore the tokamak concept is constrained to a pulsed regime³.

³ Advanced operation scenarios for ITER are under research, which are supposed to enable a steady-state operation [3].

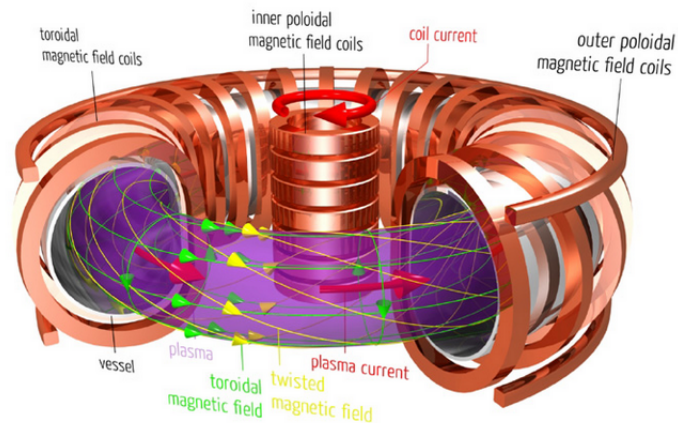


Figure 1.1.2: Twisted magnetic field lines compensate for the vertical drift of the particles [4].

The toroidal and poloidal magnetic field creates helically twisted magnetic field lines. This compensates for the drift of the particles, which are now confined on the magnetic field lines crossing the LFS and HFS. The whole configuration is axisymmetric. The poloidal field of a tokamak is usually much smaller than the toroidal component. The resulting magnetic field forms toroidally nested flux surfaces.

1.2 SCRAPE-OFF LAYER AND POWER EXHAUST

Even on the nested flux surfaces in a helically twisted magnetic field the confinement is not perfect, since stability against perturbations has to be considered. Microplasma instabilities saturate on a nearly constant turbulence level, which causes an increase in the transport of particles and heat [5]. Macroscopic instabilities lead to disruptions [6], which poses a serious issue, since they can damage the first wall. At some place in the tokamak the plasma will have contact with the wall, causing a sputtering of material into the main core region, that leads to a dilution of the plasma or even an interrupted fusion reaction. In order to have a controlled contact between the plasma and material surfaces a limiter can be used, see figure 1.2.1.

Modern Tokamaks are however based on the divertor concept, which has important advantages over the limiter concept. Additional coils create a poloidal magnetic field null at one or more points. This area is called the X-point. Compared to the limiter concept, the influx of impurities and

helium ash into the confined core region is reduced because of the use of additional pumps in the divertor region. Thus, the confined plasma is more pure leading to better confinement properties. In addition, a new operation mode of improved confinement, called the H-mode, has been discovered in a diverted geometry at ASDEX [7].

The region of the outer flux surfaces with closed field lines is called plasma edge. The area where the magnetic field lines hit the material surfaces forms the scrape-off layer (SOL), which plays a crucial role in plasma confinement [8]. Plasma coming out of the core streams along the magnetic field towards the target plates before it can reach the wall. The separatrix or last closed flux surface (LCFS) separates the edge and the SOL.

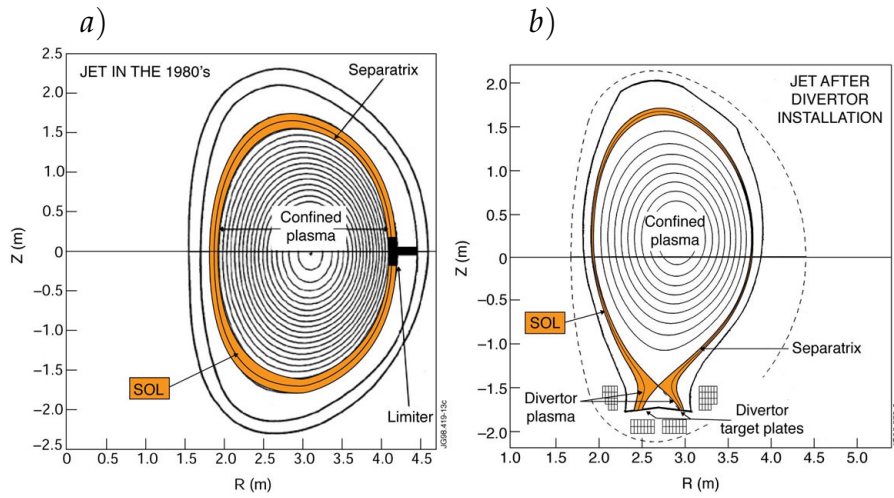


Figure 1.2.1: Poloidal cross sections of the tokamak geometries: a) Limiter b) Divertor [9]

In a very simplified picture one can estimate the scrape-off layer dimensions by assuming that for a magnetized plasma, subject to a laminar flow, the ratio of the electron-ion collision frequency ν_{ei} to the gyro-frequency ω_{ce} is given by $\nu_{ei}/\omega_{ce} \ll 1$. This leads to a scale separation of the parallel and radial electron fluxes Γ_{\parallel} and Γ_{\perp} , competing with each other, finally determining the SOL width. Particles traveling along the magnetic field lines will gyro-rotate many times before a collision, which subsequently causes a radial flux. Consequently, the parallel flux is much bigger than the radial flux giving $\Gamma_{\perp}/\Gamma_{\parallel} \approx (\nu_{ei}/\omega_{ce})^2 \ll 1$ [10]. If no other volumetric sources are present in the scrape-off layer, $\nabla \cdot \Gamma \approx 0$, one finds that it holds $\Gamma_{\perp}/\Gamma_{\parallel} \sim L_{\perp}/L_{\parallel} \ll 1$, where L_{\parallel} is half of the magnetic connection length between solid targets and L_{\perp} is a typical length scale perpendicular to the

magnetic field [10]. With the constraint of a constant loss of particles along the magnetic field one gets an exponential radial decay of the parallel particle flux towards the target plates [10]. In the best case the SOL protects the wall by scraping-off the plasma coming out of the core. In the reality, the physics is much more complicated. The characteristics of the SOL are a low plasma density and temperature, a high plasma collisionality and large scale turbulent behavior $L_{\perp}^{turb} \gtrsim \rho_s$, $L_{\parallel}^{turb} > \lambda_{mfp}$ (where $\rho_s = c_s/\omega_{ci}$ is the ion sound radius; ion gyro-frequency ω_{ci} ; mean free path λ_{mfp}) of order unity amplitudes in the normalized density, electrostatic potential and electron temperature [11]. Radial profiles have been measured experimentally. The findings confirmed the exponential decay of the radial profiles and the large amplitude fluctuations [5]. In the near scrape-off layer one observes a strong electric potential given approximately by the electron temperature $\phi \approx 3T_e$ which leads to a strong poloidal shear flow [10]. In the far SOL the profiles are almost flat and the fluctuation level is increased towards the wall. The typical SOL width is of the order of several cm in the limited geometry [12] and a few mm for the diverted case [13].

The thin SOL width in the diverted geometries introduces also new problems: With an increasing fusion machine size and power, the power exhaust from the core into the SOL also increases. This leads to very high parallel heat fluxes onto the divertor across the SOL. As was pointed out in [14, 15] the parallel heat flux width λ_q does not seem to be sensitive to the major radius of the machine but rather decreases with an increasing toroidal magnetic field which will be used in future power plants. Combined with the higher power deposition from the core for bigger machines the reduced SOL width worsens the heat flux problem. Rough approximations for DEMO showed in [16] that the power exhaust from the core into the SOL will be in the order of $P_{SOL} = 150 \text{ MW}$, which leads to the heat flux on the divertor plates $q \sim 250 \text{ MW/m}^2$, where the major radius was assumed with $R_0 = 9 \text{ m}$ and $\lambda_q \sim 1 \text{ cm}$ [17]. This by far exceeds the thermal robustness of present materials for the divertor which can hold up to 20 MW/m^2 [18]. In order to achieve a reliable and economically meaningful source of energy, damage or strong stress of the divertor needs to be avoided. A possible solution is a combination of an increase of the divertor area, magnetic flux expansion and impurities seeding (N_2 , Ne) which radiate the power before it reaches the surface such that detachment occurs [19]. For ITER, which will operate in partially detached regime, these techniques will be sufficient. However, the power loads in DEMO are expected to be five times larger and remain a major challenge still under research. Thus a deep understanding of the edge

and SOL is crucial for the future realization of power plants and plasma control.

1.3 MODELING THE EDGE AND SOL

Modeling the edge and SOL is in many ways more complicated than the rest of the device. As was pointed out in the review article [20] the physics becomes very rich in the edge and SOL, which includes radiation losses, sheath [8] and atomic physics. In addition to that, phenomena occur on many time scales ranging from the gyro-motion to the turbulence time scale. Plasma structures range from the electron gyro-radius to the machine size showing steep perpendicular gradients and also strong gradients along the magnetic field lines. We have already mentioned in the previous section that the fluctuations are of the order of unity compared to the background. This means that for modeling efforts a linearization of the quantities (splitting in a constant background part and a perturbation e.g for density $n = \delta n + n_0$) is prohibited. On top of the challenges from both, the physics and model side, the geometry of a diverted device is complex.

In the past years several numerical fluid codes have been developed in order to tackle the complexity of the edge and SOL. The GBS code [21] treated limited geometries and has been used for the studies of the SOL and plasma turbulence characterization [22–24]. BOUT++ [25] has been used for the simulation of e.g. peeling-ballooning modes in circular geometry [26], edge localized modes (ELMs) [27] and turbulence studies [28] in diverted geometries. With TOKAM3X [29], both edge transport and turbulence have been investigated [30]. The recently developed GBD code also studied plasma turbulence in a limited geometry confirming spontaneous $E \times B$ -rotation of the plasma [31]. These developments pose an important advance for the understanding of the edge and SOL in the community. However, they have one thing in common: all of the mentioned codes are based on field or flux aligned coordinates, which are singular on the separatrix and the X-point. This will be clarified in the following. A comprehensive review of flux coordinates can be found in [32]. For any ideal axisymmetric MHD equilibrium [33] the magnetic field can be written in the form

$$\mathbf{B} = I(\Psi)\nabla\varphi + \nabla\Psi \times \nabla\varphi, \quad (1.3.1)$$

where φ denotes the toroidal angle and $\Psi(R, Z)$ is the poloidal flux function, which is a solution of the Grad-Shafranov-Schlüter (GSS) equation [34, 35] and $I(\Psi)$ is a scalar function of Ψ . Eq. (1.3.1) ensures $\nabla \cdot \mathbf{B} = 0$. For a

toroidally symmetric magnetic equilibrium the poloidal flux is independent of the toroidal angle $\nabla\varphi \cdot \nabla\Psi = 0$. Furthermore $\mathbf{B} \cdot \nabla\Psi = 0$, which follows from Eq. (1.3.1), meaning that the contour lines of $\nabla\Psi$ pose flux surfaces where the poloidal basis vector is always perpendicular to the magnetic field. Assuming nested flux surfaces, one can construct from a toroidal coordinate system $\rho(\Psi), \theta, \varphi$, where the flux surface label is given by ρ and the poloidal θ and toroidal angle φ can have arbitrary representations, a coordinate system (ρ, ξ, ζ) where one of the coordinates ξ, ζ is aligned along the magnetic field. The desired form of the safety factor q , which measures the number of toroidal turns as one advances along a magnetic field line one poloidal turn, is the one of a flux function $q(\rho)$. This motivates the use of a coordinate system where the magnetic field lines are straight if rolled out on a flux surface $(\rho, \theta_S, \varphi_S)$, see figure 1.3.1 giving

$$\frac{d\theta_S}{d\varphi_S} = \frac{1}{q(\rho)}, \quad (1.3.2)$$

with the safety factor

$$q(\rho) = \frac{1}{2\pi} \int_0^{2\pi} d\theta \frac{\mathbf{B} \cdot \nabla\varphi}{\mathbf{B} \cdot \nabla\theta}. \quad (1.3.3)$$

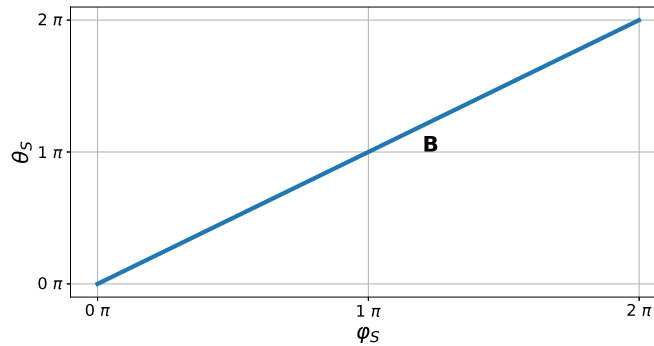


Figure 1.3.1: Representation of the magnetic field line in the straight coordinate system $(\rho, \theta_S, \varphi_S)$.

A field aligned coordinate system is constructed out of it in two ways. Either the poloidal angle is chosen as the parallel coordinate giving

$$\zeta_{pol} = \theta_S, \quad \xi_{pol} = \varphi_S - q\theta_S, \quad (1.3.4)$$

or the toroidal angle is the parallel coordinate

$$\zeta_{tor} = \varphi_S, \quad \tilde{\zeta}_{tor} = \theta_S - \frac{1}{q}\varphi_S. \quad (1.3.5)$$

On the separatrix the definition of the straight field line angles (1.3.2) breaks down as $q \rightarrow \infty$ and consequently any set of field aligned coordinates (1.3.4), (1.3.5). This is also shown in figure 1.3.2 (b), where the contours of the poloidal field line angle θ_s are sucked into the X-point. It was shown that the definition of $\rho(\Psi), \theta, \varphi$ is ill defined on the X-point, which is a saddle point in Ψ , since the Jacobian of the coordinate transformation is divergent i.e. $J = (\nabla\Psi \cdot \nabla\alpha \times \nabla\varphi)^{-1} \rightarrow \infty$ ($\nabla\Psi = 0$), where α defines a third basis vector [9]. The freedom of choice of the third basis vector allows the construction of many field aligned coordinate systems [32, 36, 37], but none of them is able to cross the separatrix. It is possible to construct a field aligned coordinate system for the core and separately to that for the open field line region. Treating both regions simultaneously using one field aligned coordinate system is not possible. Only with a special treatment of either, the coordinate system or the topology, these challenges can be overcome to some extent. The GBS code was recently extended to diverted geometries by using a toroidal coordinate system [38], where a diverted magnetic equilibrium was inserted into a torus topology. The BOUT++ code is able to cross the separatrix by using a flux aligned grid. In a similar fashion TOKAM3X performs a domain decomposition for the geometry. The magnetic equilibrium is defined separately in the core and SOL region [29]. In both codes the X-point remains special, surrounded by eight cells instead of four having a low resolution, see figure 1.3.2 (a) which was taken from [29]. Moreover there is a huge resolution imbalance between the LFS, HFS and X-point, which is problematic for turbulence simulations due to the isotropic behavior of the turbulence within the poloidal planes. Resolving the X-point with an appropriate resolution can lead either to a very expensive simulation or the simulation becomes even not feasible due to a heavy limit on the time step from the extremely high resolution on the LFS. Important effects like e.g. X-point MARFEs [39, 40], a sonic event in a high-density detached regime plasma around the X-point need an appropriate resolution around the X-point for simulations. In the worst case, the change of topology around the X-point and the resolution imbalance can lead to numerical artefacts, influencing the rest of the domain. Even if the X-point is not present, the resolution imbalance remains an issue because the flux surfaces are stretched into the direction of the X-point, making calculation of turbulent plasma transport difficult even in the core region in the vicinity of the separatrix.

These issues motivated the development of GRILLIX, a plasma turbulence code based on a flux coordinate independent approach, which is able to cross the separatrix and overcome the mentioned issues.

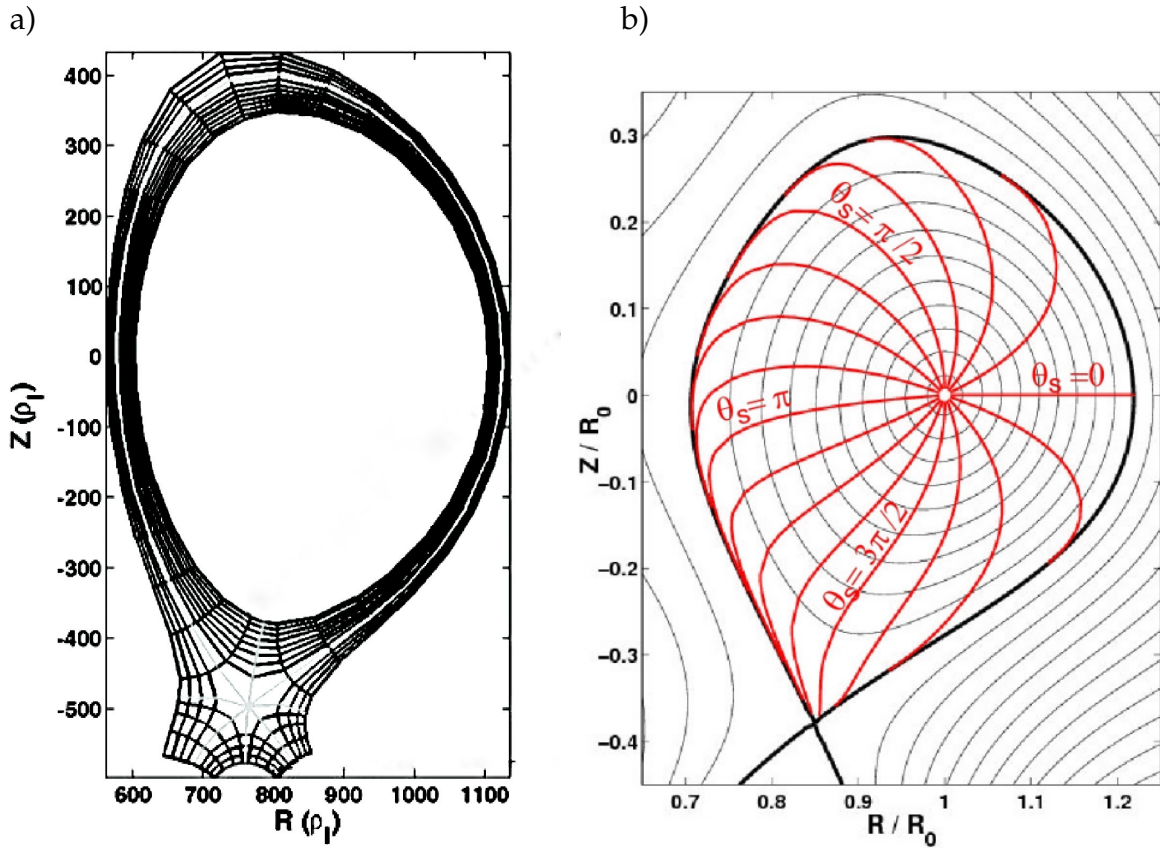


Figure 1.3.2: a) The TOKAM3X grid shows the distinct position of the X-point and resolution imbalances. b) Poloidal cross section of the contours of the poloidal flux (black) are stretched into the direction of the X-point. The poloidal straight angle (red) is sucked into the X-point [41].

1.4 GRILLIX

GRILLIX was developed from scratch by A. Stegmeir during his PhD [9]. Here a brief introduction into the code and basic concepts are given. More detailed information about the flux coordinate independent approach (FCI) can be found in [42–45].

First, a code curing the disadvantages of flux aligned coordinates should not have any singularities in the coordinate system. A cylindrical coordinate system (R, φ, Z) is well defined everywhere in a tokamak. Thus the cylindrical

computational grid (R_i, φ_k, Z_j) bounded by two limiting surfaces ψ_{min}, ψ_{max} is chosen in GRILLIX, see figure 1.4.1.

Second, the code should be computationally efficient by making use of the flute mode character of turbulent structures in a tokamak ($k_{\parallel} \ll k_{\perp}$) meaning that a relatively low toroidal resolution is sufficient. This is accomplished in GRILLIX by choosing a relatively low number of equivalently spaced poloidal planes (e.g. 6 in figure 1.4.1) where the quantities of interest are derived.

Finally, the code should avoid resolution imbalances. In GRILLIX a Cartesian grid (R_i, Z_j) is chosen within each poloidal plane providing everywhere the same resolution and numerical accuracy. Within the Cartesian grid the X-point has no distinction. It is treated in the same way like every other grid point in the domain. In GRILLIX the challenge is shifted from grid creation and singularities of the coordinate system to the discretization of parallel operators. The parallel operators are discretized with a finite difference method along the magnetic field lines.

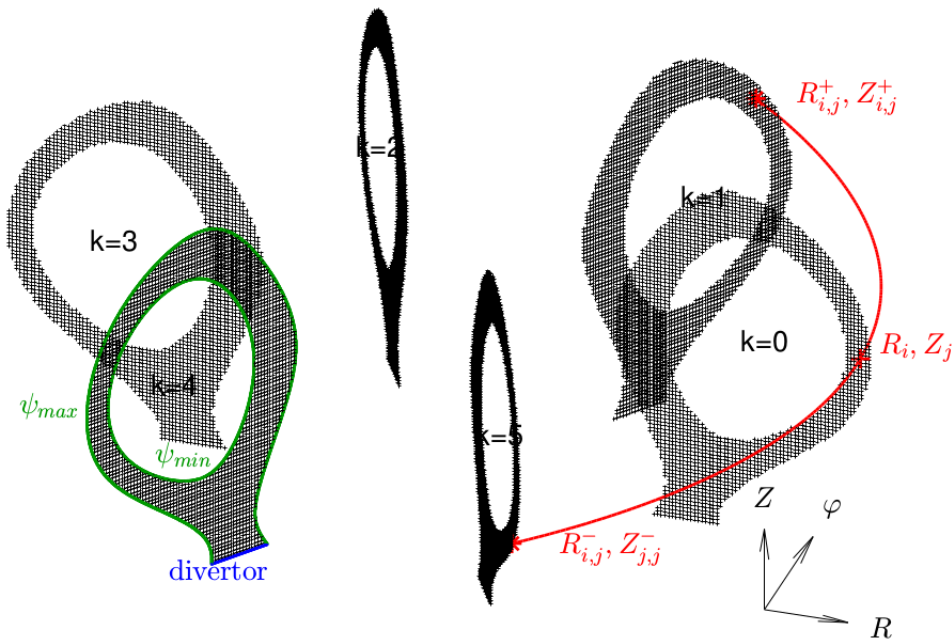


Figure 1.4.1: Schematic view of the FCI approach. The grid is coarsened in the toroidal direction φ . Within each poloidal plane a Cartesian grid is used. The magnetic field line is traced along the geometry. Penetration points on neighboring planes are calculated via an interpolation. Picture was taken from [46].

FIELD LINE TRACING Every parallel operator connects points on neighboring poloidal planes ($R_{i,j}^-, Z_{j,j}^- \leftrightarrow R_i, Z_j \leftrightarrow R_{i,j}^+, Z_{i,j}^+$) along the magnetic field line. The magnetic field is assumed to be static $\partial_t \mathbf{B} = 0$. In order to get a high directional accuracy, the magnetic field line is traced from a given grid point to the next poloidal plane, where the intersection point in general does not coincide with a grid point. An interpolation within the poloidal plane needs to be applied in order to get the intersection point. For static and axisymmetric equilibria the field line tracing procedure needs to be applied only once at the beginning of the simulation on one single plane. For 3D equilibria (e.g. Stellarator) the field line tracing has to be applied on each plane [47]. The following ODEs have to be solved for the field line tracing procedure needed for the establishment of parallel operators [46]

$$R'(\varphi) = \frac{B^R}{B\varphi}, \quad R(0) = R_0 \quad (1.4.1)$$

$$Z'(\varphi) = \frac{B^Z}{B\varphi}, \quad Z(0) = Z_0 \quad (1.4.2)$$

$$s'(\varphi) = \frac{B}{B\varphi}, \quad s(0) = 0 \quad (1.4.3)$$

$$v'(\varphi) = \frac{1}{B\varphi}, \quad v(0) = 0 \quad (1.4.4)$$

where R', Z' define the shift from the initial position R_0, Z_0 of the radial coordinate R and the poloidal coordinate Z on the neighboring poloidal planes, respectively. Eq. (1.4.3) defines the length of a magnetic field line. The last equation solves for the flux box volumes around a magnetic field. Having obtained the intersection points, the length along the magnetic field line and the flux box volume, parallel operators can be constructed.

PARALLEL GRADIENT Here a general coordinate free representation of the parallel gradient used in GRILLIX is presented. It allows the discretization of the parallel gradient on field lines which are strongly converging or diverging leading to map distortions, which is discussed in more details in [45,46]. The parallel gradient can be expressed via a surface integral

$$\nabla_{\parallel} f = \lim_{V \rightarrow 0} \frac{1}{BV} \int_{\partial V} f \mathbf{B} \cdot d\mathbf{n} \quad (1.4.5)$$

with an arbitrary volume parametrization V and f being some quantity of interest. This expression is given in its simplest form by a finite difference along the magnetic field line

$$\nabla_{\parallel} f \rightarrow \frac{f_{k+1}(R_{i,j}^+, Z_{i,j}^+) - f_k(R_{i,j}^-, Z_{i,j}^-)}{s_j^+ + s_j^-}. \quad (1.4.6)$$

The discrete version of further parallel operators appearing in the model, i.e. parallel divergence and parallel diffusion, are obtained via the support operator method, which is discussed in detail in chapter 4.

1.5 MOTIVATION AND OUTLINE

The FCI concept allows the simulation of complex and diverted geometries treating the X-point in a very natural way. Once the parallel operators are discretized correctly along the field line, they can be applied on different models. In GRILLIX the FCI concept was applied for the first time in a diverted geometry [9] using the well established Hasegawa-Wakatani turbulence model [48]. This model evolves disturbances on a constant background. As was pointed out in chapter 1.2 the physics of the edge and SOL is rather complex including turbulent high amplitude plasma fluctuations prohibiting a splitting of the quantities in a constant background and disturbances. However using the Hasegawa-Wakatani model was a necessary step for the implementation of the FCI concept, reducing the complexity and proving that the FCI approach is able to tackle the simulation of turbulence in the edge and SOL simultaneously, see figure 1.5.1.

The next logical step, which motivated this thesis, is the application of the FCI approach in GRILLIX on a more advanced model capturing the complex physics of the edge and SOL. In particular this model should be 'global', meaning that no assumptions are made about the density and temperature fluctuation amplitudes anywhere in the equations. As was pointed out at the beginning of this chapter 'a virtual fusion plasma needs to have *reliable, validated* and *predictive* capabilities'. Thus the final goal of this thesis is the implementation of a turbulence model (global electromagnetic drift-reduced Braginskii model) in a reliable, tested and validated way, posing a solid foundation for turbulence simulations with GRILLIX in complex geometries. To achieve this, the following procedure was necessary:

In chapter 2 the target model, based on global electromagnetic drift reduced Braginskii equations, are derived. The starting point is on a kinetic level, which allows the most complete description of the plasma. Several simplifications and the drift approximation are necessary in order to bring the model into a form ready for discretization. The energy conservation properties of the model are emphasized. The widely used Boussinesq approximation, which is not valid in the edge and SOL, is relaxed and the impact of it on the conservation properties is described. Finally the details of the discretization and implementation in a slab geometry of the model are discussed. The slab geometry acts as a tool in order reduce the complexity of the implementation. The knowledge gained in this simplified geometry helps to perform the transition to more complex geometries. The implementation of the global electromagnetic drift reduced model is verified with the method of manufactured solutions.

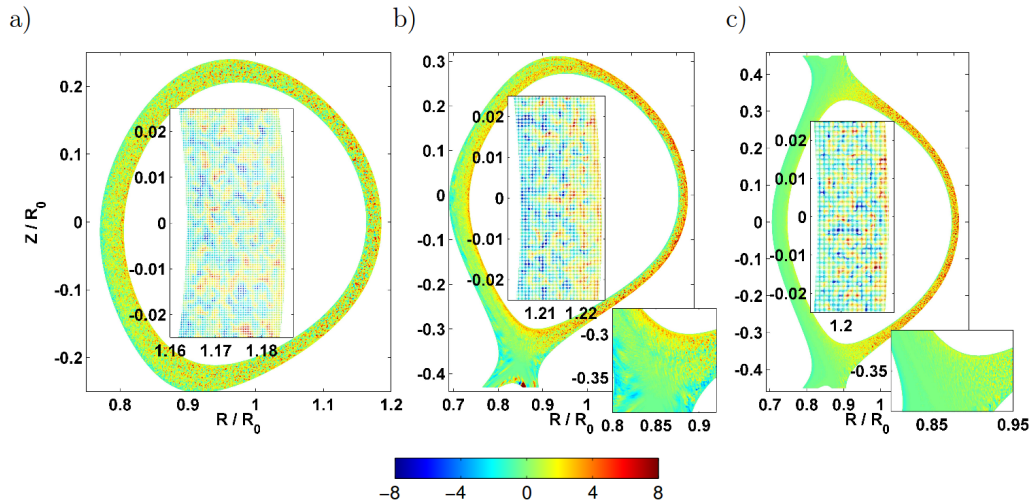


Figure 1.5.1: GRILLIX in the year 2015 within Hasegawa-Wakatani model. Snapshots of density fluctuations n at a poloidal plane. a) closed field line region b) single-null c) double-null; Insets show outboard midplane region and X-point region enlarged. Plots are taken from [49]

In chapter 3 the complexity of simulations is successively increased. Starting with qualitative description of blob propagation, a high amplitude event often observed in the edge and SOL, analytic expression for scalings with the width and the amplitude of the blob are derived and compared to GRILLIX results. The impact of the Boussinesq approximation on blob propagation is investigated. Fundamental tests are performed in order to check the electromagnetic dynamics comparing the propagation of an Alfvén wave in GRILLIX with analytical predictions. It was found that the extension of GRILLIX to an electromagnetic model is crucial from a numerical and physical point of view. The simulation of turbulence on closed field lines in slab geometry is performed in order to check the conservation properties (energy and particles) in GRILLIX. After that the Large Plasma Device (LAPD) is modeled in GRILLIX. The turbulence results are compared to experimental data validating GRILLIX simulations.

Finally the FCI approach is applied in chapter 4 comparing turbulence dynamics in a circular, single-null and double-null geometries on closed magnetic field lines. The radial plasma transport is derived and compared in these geometries.

MODEL AND IMPLEMENTATION

In order to describe plasma in the edge and SOL region of a fusion device a model which is able to capture the main turbulence dynamics is required. The Hasegawa-Wakatani model [48] which was implemented in GRILLIX in [9] is not suitable for the scrape-off layer since it describes only small amplitude fluctuations on a constant background. The fluctuations in the SOL can reach an amplitude which is several orders higher than the background plasma [50]. In the edge region the plasma is found to have low temperatures and a high collisionality such that the assumption $\omega/\nu_c \ll 1$ with the frequency of interest ω and ν_c the collision frequency is valid. For such a situation the Braginskii model can be applied. Collisions are important because they bring the plasma into an equilibrium state, defined by a Maxwellian distribution. It is the collisional part of the equations which fails at higher temperatures [51], the rest of the system is a general set of fluid equations. The Braginskii system evolves vector quantities on very diverse time scales ranging from the ion cyclotron frequency up to the confinement time scale. In order to take out the fast time scales from the equations and keep only the frequencies of interest for plasma turbulence a drift approximation is performed. Along with the drift approximation a set of other assumptions are made in order to simplify the equations further which yields the reduced fluid model. The derivation of the reduced fluid model follows mainly the works by B. Scott [52], A. Zeiler [53] and the original work by S. Braginskii [54]. The final model contains thermal and electromagnetic effects which were absent in many previous works [21,29,44]. It is shown that the model conserves energy. Furthermore the use of the Boussinesq approximation [55], which is popular in the plasma community, is discussed. The impact of it on the energy theorem will be derived. It is shown that it was used often in a non-conservative form, breaking the entire conservation properties of the complete system [21].

2.1 BRAGINSKII EQUATIONS

The most complete and detailed description of plasma dynamics is obtained by solving the underlying equation of motion for each particle in the electric and magnetic field. Each particle has 6 degrees of freedom (3 spatial, 3 velocity) leading to a 6D phase space with $6N$ unknowns for N particles. Thus, following the trajectory of each particle is computationally impossible even for low densities in a tokamak.

A simplification is the statistical kinetic approach describing a hydrogen plasma by a particle distribution function $f_j(t, \mathbf{r}, \mathbf{v})$ for the particle species (j : electrons e , single charged ions i) being evolved with respect to Boltzmann's equation [56]

$$\frac{\partial f_j(t, \mathbf{r}, \mathbf{v})}{\partial t} + \mathbf{v}_j \cdot \nabla_{\mathbf{r}} f_j(t, \mathbf{r}, \mathbf{v}) + \frac{\mathbf{F}_j}{m_j} \nabla_{\mathbf{v}} f_j(t, \mathbf{r}, \mathbf{v}) = \left(\frac{\partial f_j(t, \mathbf{r}, \mathbf{v})}{\partial t} \right)_{collisions}. \quad (2.1.1)$$

The interaction of particles in the plasma is described in Eq. (2.1.1) via the long ranging Lorentz force

$$\mathbf{F} = q_j(\mathbf{E} + \mathbf{v} \times \mathbf{B}) \quad (2.1.2)$$

and the short ranging collisions, described by the term $\left(\frac{\partial f_j(t, \mathbf{r}, \mathbf{v})}{\partial t} \right)_{collisions}$ on the right hand side. The Debye length separates these two scales. The electromagnetic fields can be computed self-consistently via the Maxwell equations. This reduces the required computational resources, however its demand is too high for present computers.

In Gyrokinetics the 6D phase-space is reduced to 5D by averaging the fast gyro-motion out of the equations. The system of equations is a gyro-averaged kinetic Boltzmann equation. This makes direct numerical computations possible in a reasonable time [57, 58].

A further reduction of the dimensions to 3D leads to a fluid description of the plasma. This approach is more suited for a collisional plasma in the edge region. In a fluid model the plasma is characterized by moments M^n which are integrations over the particle distribution function

$$M^{(n)} = \int_{-\infty}^{+\infty} \mathbf{v}^n f(\mathbf{r}, \mathbf{v}) d^3v \quad (2.1.3)$$

with the volume element d^3v in the velocity space. The moments define unknowns of the fluid equations. The first three moments of the Boltzmann equation can be identified with the density $n_j(t, \mathbf{r})$, momentum $m_j n_j \mathbf{v}_j(t, \mathbf{r})$

and temperature $T_j(t, \mathbf{r})$ of a fluid segment, respectively. In principle an infinite number of equations is produced in this way and for closure of the moment n , the moment $n + 1$ is required. An extra equation expressing the last equation independent of the others is needed. Braginskii used a collisional closure for this purpose which requires the distribution function to be close to a local Maxwellian in velocity space

$$f_j = \frac{n_j}{(2\pi T_j k_B / m_j)^{3/2}} \exp(-(\mathbf{v} - \mathbf{u})^2 / v_T^2). \quad (2.1.4)$$

With this distribution the right hand side of the Boltzmann equation is zero, meaning that the collision term vanishes, regardless of its actual form.

Furthermore it is assumed that the macroscopic time variations are slower than the collisional time. The scale length perpendicular to the magnetic field is longer than the ion gyro radius. More, the scale length along the magnetic field is longer than the mean free path. As was pointed out in [59,60] this can actually become questionable. Heat carrying electrons have a much longer mean free path compared to thermal electrons. They can travel very long distances without experiencing a single collision. In particular this lead to a deviation from the Maxwellian distribution for high energy electrons, which make a kinetic approach useful. Higher moments of the distribution function e.g. parallel heat conduction (2.1.13) are sensitive to the tails. This is the reason why the fluid approach fails first for these terms. However this topic is still under research [59] and out of the scope of this thesis.

The Maxwellian distribution vanishes when the velocity approaches $\pm\infty$.

The first three moments of the Boltzmann equation yield a set of equations for the density, momentum and the temperature for each species

$$\frac{\partial n_j}{\partial t} + \nabla_{\mathbf{r}} \cdot (\mathbf{u}_j n_j) = 0, \quad (2.1.5)$$

$$m_j n_j \left(\frac{\partial}{\partial t} + \mathbf{u}_j \cdot \nabla_{\mathbf{r}} \right) \mathbf{u}_j + \nabla_{\mathbf{r}} \cdot \mathbf{\Pi}_j = q_j n_j (\mathbf{E} + (\mathbf{u}_j \times \mathbf{B})) + \mathbf{R}_j, \quad (2.1.6)$$

$$\frac{3}{2} n_j \left(\frac{\partial}{\partial t} + \mathbf{u}_j \cdot \nabla_{\mathbf{r}} \right) T_j + p_j \nabla_{\mathbf{r}} \cdot \mathbf{u}_j = -\nabla_{\mathbf{r}} \cdot \mathbf{q}_j - \mathbf{\Pi}_j \cdot \nabla_{\mathbf{r}} \cdot \mathbf{u}_j + Q_j \quad (2.1.7)$$

where the fluid element velocity is \mathbf{u}_j . The pressure tensor $\mathbf{\Pi}_j$ consists of an isotropic part $p_j = \text{Tr}(\mathbf{\Pi}_j)/3$ which is the pressure of the fluid element and an anisotropic part π_j which is called the stress tensor, giving $\mathbf{\Pi}_j = p_j + \pi_j$. The full expression of the stress tensor is given in [54]. The collision term \mathbf{R}_j represents momentum exchange between particles and consists of

$$\mathbf{R}_j = \mathbf{R} \equiv \mathbf{R}_{ei} = -\mathbf{R}_{ie} = \mathbf{R}_u + \mathbf{R}_T = ne \mathbf{b} j_{\parallel} / \sigma_{\parallel} - 0.71 n \mathbf{b} \nabla_{\parallel} T_e, \quad (2.1.8)$$

where the term \mathbf{R}_u describes friction between the species. The conductivity is given by

$$\sigma_{\parallel} = e^2 n / (0.51 m_e \nu_e) \quad (2.1.9)$$

with $\nu_e = 1/\tau_e$ being the electron collision frequency with the collision time

$$\tau_e = \frac{3T_e^{3/2}}{4n_e \Lambda e^4} \sqrt{m_e / 2\pi}, \quad (2.1.10)$$

the Coulomb logarithm

$$\Lambda = 24 - \ln(n_e^{1/2} / T_e) \quad (2.1.11)$$

and the parallel current

$$j_{\parallel} = en(u_{\parallel i} - v_{\parallel e}). \quad (2.1.12)$$

The last term in Eq. (2.1.8) is the thermal force in parallel direction. As pointed out in [53] the friction in perpendicular direction is neglected, keeping only the parallel component of \mathbf{R}_j due to its importance for plasma turbulence. The species heat fluxes are given by

$$\mathbf{q}_i = -\kappa_{\parallel i} \mathbf{b} \nabla_{\parallel} T_i + \kappa_{\perp i} \mathbf{b} \times \nabla_{\perp} T_i \quad (2.1.13)$$

$$\mathbf{q}_e = -0.71 T_e \mathbf{b} j_{\parallel} / e - \kappa_{\parallel e} \mathbf{b} \nabla_{\parallel} T_e + \kappa_{\perp e} \mathbf{b} \times \nabla_{\perp} T_e \quad (2.1.14)$$

with $\kappa_{\parallel i} = 3.9 \frac{p_i \tau_i}{m_i}$, $\kappa_{\perp i} = \frac{5p_i}{2m_i \omega_{ci}}$, $\kappa_{\parallel e} = 3.2 \frac{p_e \tau_e}{m_e}$ and $\kappa_{\perp e} = \frac{5p_e}{2m_e \omega_{ce}}$. The energy transfer due to collisions is Q_j . The full expressions for these quantities and the pressure tensor are given in [54].

The unit vector along the magnetic field is given by $\mathbf{b} = \vec{b}/B$ and the subscript $\parallel, (\perp)$ denotes the direction along (perpendicular to) the magnetic field. In the energy transfer Q_j only the thermal part is kept [53], giving

$$Q_e = \frac{j_{\parallel}^2}{\sigma_{\parallel}} - \frac{0.71}{q} j_{\parallel} \nabla_{\parallel} T_j \quad (2.1.15)$$

In addition to the fluid equations the Maxwell equations have to be added to the system. The Braginskii model needs further simplifications which are pointed out in the next section.

2.2 STANDARD SIMPLIFICATIONS

For the reduction of the complexity of the Braginskii model some standard assumptions are made. For fusion plasmas even a small charge separation leads to a very large electric fields driving the plasma towards a neutral state. This yields the plasma oscillations with the frequency $\omega_{pe} = \sqrt{4\pi n_e e^2 / m_e} \sim 10^{11} s^{-1}$, describing an oscillation of the electrons with respect to the ions which are assumed fixed here, due to the much higher mass. This frequency is much faster compared to the time scales of plasma turbulence giving

$$\omega \ll \omega_{pe}, \Omega_e, ck \quad (2.2.1)$$

where ck is the frequency of light and the electron gyro frequency is $\Omega_e = eB / (m_e c)$. In this regime the electron density fluctuations $n_e - n_0$ remains close to thermodynamic equilibrium

$$n_e - n_0 \simeq n_0 \frac{e\phi}{T_e} \sim (n_i - n_e) \frac{L^2}{\lambda_D^2} \quad (2.2.2)$$

where L is the characteristic scale length of the turbulence and the relation between the electron density and electrostatic potential was used

$$n_e = n_0 \exp\left[\frac{e\phi}{T_e}\right] \simeq n_0 \left[1 + \frac{e\phi}{T_e}\right]. \quad (2.2.3)$$

Assuming that the scales of interest are much bigger than the Debye length $\lambda_D = \sqrt{T_e / 4\pi e^2 n}$ the relation between ion and electron densities follows as

$$n_i \approx n_e \equiv n \quad (2.2.4)$$

In the following n is used for the density of the plasma.

2.3 DRIFT APPROXIMATION

If the plasma disturbances in the parallel direction (along the magnetic field) are on very different length scales compared to the perpendicular direction, the frequencies of the corresponding Alfvén oscillations are also disparate. This can be found in a fusion device with a very strong guiding magnetic field. In such a situation, if one assumes low frequency dynamics in parallel direction, the compressional Alfvén waves in transverse direction are not excited. This leads to a quasi static force balance in the perpendicular

direction without the fast compressional waves. Under these assumptions plasma dynamics becomes plasma drift dynamics describing scalar quantities (density, momentum, temperature).

The definition of drift approximation

The strong guiding magnetic field in a fusion device leads to structures strongly elongated along the magnetic field lines compared to the perpendicular direction or in terms of wavenumber

$$k_{\perp} \gg k_{\parallel} \quad (2.3.1)$$

This is the flute mode character saying that the corresponding Alfvén oscillations in perpendicular and parallel direction are also disparate. The fluid drift motion is of the same order as the shear Alfvén dynamics. Thus, the frequencies of interest are in the range of

$$\omega \sim k_{\parallel} v_A \quad (2.3.2)$$

where v_A is the Alfvén speed. Combining these two relations yields

$$\omega \ll k_{\perp} v_A. \quad (2.3.3)$$

An assumption is that $\omega \ll \Omega_i$, that the dynamics of interest is also much slower than the ion gyro-motion. It follows, that the time scales of motion are much slower compared to compressional waves, thus these are not excited. A further inequality Eq. (2.3.4) implies, that the perpendicular spatial scale L_{\perp} is much bigger then the drift scale ρ_s ,

$$\delta \equiv \frac{\rho_s}{L_{\perp}} \ll 1, \quad (2.3.4)$$

where $\rho_s = c\sqrt{m_i T_e}/eB$ is the sound radius, which also implies $c_s/L_{\perp} \sim \delta$. The magnetic pressure is also assumed be much bigger the the gas pressure, resulting in a additional assumption

$$\beta_e \equiv \frac{4\pi p_e}{B^2} \ll 1. \quad (2.3.5)$$

These assumptions can be interpreted as a quasi static force balance across magnetic field lines, meaning without dynamical oscillations. The perpendicular motion remains incompressible. This leads to a separation of the parallel and perpendicular dynamics, which can be then expressed with the help

of stream functions being scalar quantities among the dependent variables. This gives a drift reduction of the initial Braginskii system, which evolved vector quantities in a wide range of frequencies.

Perpendicular force balance

In order to obtain more insight into the perpendicular drift dynamics the velocity of a fluid element is split up in a parallel and perpendicular part from the previously stated assumptions

$$\mathbf{u}_j = u_{\parallel j} \mathbf{b} + \mathbf{u}_{\perp j} \quad (2.3.6)$$

With respect to δ we expand the perpendicular velocity as

$$\mathbf{u}_{\perp j} = \mathbf{u}_{\perp}^* + \delta \mathbf{u}_{\perp}^{(0)} + \delta^2 \mathbf{u}_{\perp}^{(1)} + \dots, \quad (2.3.7)$$

where the lowest order velocity \mathbf{u}_{\perp}^* denotes the gyro-motion. Now the momentum Eq. (2.1.6) is written for each species (e electrons, i ions) neglecting \mathbf{R} , the electron inertia $m_e \ll m_i$ [52] and assuming a single charged fluid with $n_e = n_i = n$,

$$m_i n \left(\frac{\partial}{\partial t} + \mathbf{u}_i \cdot \nabla_{\mathbf{r}} \right) \mathbf{u}_i + \nabla_{\mathbf{r}} \cdot \pi_i = -\nabla_{\mathbf{r}} p_i + en \left(\mathbf{E} + \frac{1}{c} (\mathbf{u}_i \times \mathbf{B}) \right), \quad (2.3.8)$$

$$0 = -\nabla_{\mathbf{r}} p_e - en \left(\mathbf{E} + \frac{1}{c} (\mathbf{v}_e \times \mathbf{B}) \right). \quad (2.3.9)$$

Assuming that the parts on left side of the ion momentum equation are one order smaller in δ compared to the right side [52], the equations are solved for $\mathbf{u}_{\perp j}$ in the perpendicular plane by applying the drift operator $\frac{c}{B^2} \mathbf{B} \times$ to the both equations assuming the perpendicular electric field to be electrostatic

$$\mathbf{E}_{\perp} = -\nabla_{\perp} \phi, \quad E_{\parallel} = -\frac{1}{c} \frac{\partial A_{\parallel}}{\partial t} - \nabla_{\parallel} \phi. \quad (2.3.10)$$

which yields the lowest order solution in δ ,

$$\mathbf{u}_{i\perp}^{(0)} = \frac{c}{B^2} \mathbf{B} \times \nabla_{\perp} \phi + \frac{1}{ne} \frac{c}{B^2} \mathbf{B} \times \nabla_{\mathbf{r}} p_i, \quad (2.3.11)$$

$$\mathbf{v}_{e\perp}^{(0)} = \frac{c}{B^2} \mathbf{B} \times \nabla_{\perp} \phi - \frac{1}{ne} \frac{c}{B^2} \mathbf{B} \times \nabla_{\mathbf{r}} p_e. \quad (2.3.12)$$

The single parts of the velocity vector are given by

$$\mathbf{v}_{E \times B} = \frac{c}{B^2} \mathbf{B} \times \nabla_{\perp} \phi, \quad \mathbf{v}_{Di} = \frac{1}{ne} \frac{c}{B^2} \mathbf{B} \times \nabla p_i, \quad \mathbf{v}_{De} = -\frac{1}{ne} \frac{c}{B^2} \mathbf{B} \times \nabla p_e, \quad (2.3.13)$$

which are respectively, the $E \times B$ -drift (which is equal for both species) and the diamagnetic drift for ions and electrons. In the following the gradient will be always in spatial coordinates such that the notation \mathbf{r} will be omitted in $\nabla_{\mathbf{r}}$. In order to calculate the next order drift in δ , the lowest order drifts are inserted in the ion momentum equation

$$m_i \left(\frac{\partial}{\partial t} + \mathbf{u}_i \cdot \nabla \right) \mathbf{u}_{\perp i}^{(0)} + \nabla \cdot \pi_i = \frac{en}{c} (\mathbf{u}_{\perp i}^{(1)} \times \mathbf{B}), \quad (2.3.14)$$

Again the drift operator is applied

$$\frac{m_i}{e} \frac{c}{B^2} \mathbf{B} \times \left(\frac{\partial}{\partial t} + \mathbf{u}_{\perp} \cdot \nabla \right) \mathbf{u}_{\perp i}^{(0)} + \frac{c}{B^2} \mathbf{B} \times \nabla \cdot \pi_i = \bar{\mathbf{u}}_{\perp i}^{(1)}, \quad (2.3.15)$$

The diamagnetic part of the ion stress tensor $-m_i n \mathbf{v}_{Di} \cdot \nabla \mathbf{u}_{\perp i}^{(0)}$ cancels the advection with the diamagnetic velocity, a procedure known as the diamagnetic cancellation. In the temperature equation the diamagnetic advection is canceled by the diamagnetic heat flux. Consequently, the diamagnetic drift does not contribute to particle and heat transport, which are dominated by the $E \times B$ -drift. The diamagnetic drift is a pure fluid drift. No particles are moving due to a pressure gradient. However more or faster particles are gyro-rotating along the pressure gradient causing a net fluid flow. The polarization drift follows from Eq. (2.3.15)

$$\begin{aligned} \mathbf{u}_{\perp i}^{(1)} &= \frac{m_i}{e} \frac{c}{B^2} \mathbf{B} \times \left(\frac{\partial}{\partial t} + \mathbf{u}_i \cdot \nabla \right) \mathbf{u}_{\perp i}^{(0)} + \frac{c}{B^2} \mathbf{B} \times \left\{ p_i \left(\nabla \times \frac{\mathbf{b}}{\omega_{ci}} \right) \cdot \nabla \mathbf{u}_{\perp i}^{(0)} + \right. \\ &\quad \left. \nabla_{\perp} \left(\frac{p_i}{2\omega_{ci}} \nabla \cdot \mathbf{b} \times \mathbf{u}_{\perp i}^{(0)} \right) + \mathbf{b} \times \nabla \left(\frac{p_i}{2\omega_{ci}} \nabla_{\perp} \cdot \mathbf{u}_{\perp i}^{(0)} \right) + G\mathbf{k} - \nabla G/3 \right\} \\ &=: \mathbf{v}_p, \end{aligned} \quad (2.3.16)$$

where here the velocity vector is given up to first order $\mathbf{u}_i = \mathbf{v}_{E \times B} + \mathbf{v}_p + \mathbf{v}_{Di} + u_{\parallel i} \mathbf{b}$ and $\mathbf{k} = \mathbf{b} \cdot \nabla \mathbf{b}$ is the field line curvature vector. It is important to answer the question: Why does the polarization drift has to be kept in the equations even if it is formally one order below the other drifts? First, as will be shown later, the polarization drift is important for energy conservation. Second, although \mathbf{v}_p is one order below the other drifts its divergence $\nabla \cdot \mathbf{v}_p$ is not [52]. It may be seen in more detail if one assumes the scale of motion

comparable to ρ_s and the dynamical frequency to c_s/L_\perp . The $E \times B$ -drift advection is then in the order of magnitude

$$\mathbf{v}_{E \times B} \cdot \nabla n \sim \frac{c}{B} \frac{\phi}{\rho_s} \frac{n}{L_\perp}. \quad (2.3.17)$$

The divergence of the polarization drift is comparable to that assuming $\frac{\partial}{\partial t} \sim \frac{c_s}{L_\perp}$

$$n \nabla \cdot \mathbf{v}_p \sim \frac{n}{\rho_s} \frac{c_s/L_\perp}{\Omega_i} \frac{c}{B} \frac{\phi}{\rho_s} \sim \frac{c}{B} \frac{\phi}{\rho_s} \frac{n}{L_\perp}. \quad (2.3.18)$$

It means that advection by $E \times B$ -drift and the divergence of the polarization drift are of the same order of magnitude. The divergence of the polarization drift will be required for the vorticity equation later on.

2.4 DRIFT REDUCED EQUATIONS

With the result from the last section one can derive a closed set of equations for the scalar quantities: the density n , the parallel ion momentum $u_{\parallel i}$, the potential ϕ and the electron temperature T_e . From here on we assume cold ions $T_i = 0$, which simplifies the equations due to $p_i, \mathbf{v}_{Di} = 0$.

Continuity equation

The electron continuity equation has been chosen, due to the absence of the polarization drift

$$\frac{\partial}{\partial t} n + \nabla \cdot n \left(\mathbf{v}_{E \times B} + \mathbf{v}_{De} + v_{\parallel e} \mathbf{b} \right) = 0. \quad (2.4.1)$$

Vorticity

In order to obtain an equation for the electrostatic potential, one can subtract the continuity equations for both species and using the quasi-neutrality condition yielding $\nabla \cdot \mathbf{j} = 0$ which is given in terms of $\mathbf{j} = \mathbf{j}_p + \mathbf{j}_{De} + \mathbf{j}_{\parallel}$,

$$\nabla \cdot \left(n \mathbf{v}_{pol} - n (\mathbf{v}_{De}) + \frac{j_{\parallel}}{e} \mathbf{b} \right) = 0. \quad (2.4.2)$$

Generalized Ohm's law

In order to receive the current conservation equation the momentum equations for both species are used in parallel direction

$$m_e n \left(\frac{\partial}{\partial t} + \mathbf{v}_e \cdot \nabla \right) \mathbf{b} v_{\parallel e} = -neE_{\parallel} - \nabla_{\parallel} p_e - \nabla_{\parallel} \pi_e + \mathbf{R}, \quad (2.4.3)$$

$$m_e n \left(\frac{\partial}{\partial t} + \mathbf{u}_i \cdot \nabla \right) \mathbf{b} u_{\parallel i} = \frac{m_e}{m_i} neE_{\parallel} - \frac{m_e}{m_i} \mathbf{R}, \quad (2.4.4)$$

where the ion momentum equation was multiplied by $\frac{m_e}{m_i}$. Subtracting these two equations

$$m_e n \left(\frac{\partial}{\partial t} + \mathbf{v}_e \cdot \nabla \right) \mathbf{b} v_{\parallel e} - m_e n \left(\frac{\partial}{\partial t} + \mathbf{u}_i \cdot \nabla \right) \mathbf{b} u_{\parallel i} = -neE_{\parallel} - \nabla_{\parallel} p_e - \nabla_{\parallel} \pi_e + \mathbf{R}, \\ + \frac{m_e}{m_i} neE_{\parallel} + \frac{m_e}{m_i} \mathbf{R}. \quad (2.4.5)$$

Neglecting the electron stress tensor and the terms with the mass ratio $\frac{m_e}{m_i}$ and using that it holds $u_{\parallel i} \ll v_{\parallel e}$ yields the generalized Ohm's law with the vector potential A_{\parallel}

$$\frac{j_{\parallel}}{\sigma_{\parallel}} = -\nabla_{\parallel} \phi + \frac{1}{c} \frac{\partial}{\partial t} A_{\parallel} + \frac{1}{en} \nabla_{\parallel} p_e + 0.71 \nabla_{\parallel} T_e / e - m_e / e \left(\frac{\partial}{\partial t} + (\mathbf{v}_{E \times B} + v_{\parallel e} \mathbf{b}) \cdot \nabla \right) \frac{j_{\parallel}}{en} \quad (2.4.6)$$

Parallel ion momentum

The parallel ion momentum equation is obtained by taking again the parallel component of the momentum equation for both species

$$m_e n \left(\frac{\partial}{\partial t} + \mathbf{v}_e \cdot \nabla \right) \mathbf{b} v_{\parallel e} = -neE_{\parallel} - \nabla_{\parallel} p_e + \mathbf{R}, \quad (2.4.7)$$

$$m_i n \left(\frac{\partial}{\partial t} + \mathbf{u}_i \cdot \nabla \right) \mathbf{b} u_{\parallel i} = -\mathbf{R}. \quad (2.4.8)$$

Summing up these two equations yields the parallel ion momentum equation taking into account the cold ion assumption

$$\left(\frac{\partial}{\partial t} + \mathbf{u}_i \cdot \nabla\right) u_{\parallel i} \mathbf{b} = -\frac{1}{m_i n} \nabla_{\parallel} p_e \quad (2.4.9)$$

electron Temperature

The electron temperature equation follows directly from the Braginskii equations

$$\begin{aligned} \frac{3}{2} n \left(\frac{\partial}{\partial t} + (\mathbf{v}_{E \times B} + v_{\parallel e} \mathbf{b} + \mathbf{v}_{De}) \cdot \nabla \right) T_e &= -\nabla \cdot \mathbf{q}_e + Q_e + \frac{5c}{2e} p_e \left(\nabla \times \frac{\mathbf{b}}{B} \right) \cdot \nabla T_e \\ &\quad - p_e \nabla \cdot (\mathbf{v}_{E \times B} + \mathbf{v}_{De} + v_{\parallel e} \mathbf{b}). \end{aligned} \quad (2.4.10)$$

2.5 ENERGY CONSERVATION

In [53] it is shown that the energy is perfectly conserved for the whole system. Here only the final energy theorem is given.

Total energy theorem

Summarizing the energies contained in the system yields the perpendicular kinetic, parallel kinetic, thermal and electromagnetic energies

$$\frac{\partial}{\partial t} \frac{1}{2} n m_i \mathbf{v}_{E \times B}^2 + \nabla \cdot \left[\frac{1}{2} n m_i \mathbf{v}_{E \times B}^2 \mathbf{u}_i + \phi \mathbf{j} + \mathbf{v}_{E \times B} p_e \right] = j_{\parallel} \nabla_{\parallel} \phi + p_e \cdot \nabla \mathbf{v}_{E \times B}, \quad (2.5.1)$$

$$\frac{\partial}{\partial t} \frac{1}{2} n m_i u_{\parallel i}^2 + \nabla \cdot \left[\frac{1}{2} m_i n u_{\parallel i}^2 \mathbf{u}_i \right] = p_e \nabla_{\parallel} u_{\parallel i}, \quad (2.5.2)$$

$$\begin{aligned} \frac{3}{2} \frac{\partial}{\partial t} p_e + \nabla \cdot \left[\frac{3}{2} \mathbf{v}_{E \times B} p_e + \frac{5}{2} p_e v_{\parallel e} \mathbf{b} - q_{\parallel e} \mathbf{b} - \frac{5c}{2B^2} \mathbf{B} \times \nabla \frac{p_e T_e}{e} \right] &= v_{\parallel e} \nabla_{\parallel} p_e - p_e \nabla \cdot \mathbf{v}_{E \times B} \\ &\quad + Q_e. \end{aligned} \quad (2.5.3)$$

$$\begin{aligned} \frac{\partial}{\partial t} \left(\frac{1}{2} n m_e \left(\frac{j_{\parallel}}{en} \right)^2 + \frac{B_{\perp}^2}{8\pi} \right) + \nabla \cdot \left[\frac{1}{2} n m_e \left(\frac{j_{\parallel}}{en} \right)^2 \mathbf{v}_{\parallel e} - \frac{\nabla_{\perp} A_{\parallel}}{4\pi} \frac{\partial}{\partial t} A_{\parallel} \right] &= -j_{\parallel} \nabla_{\parallel} \phi - p_e \nabla_{\parallel} u_{\parallel i} \\ &\quad - v_{\parallel e} \nabla_{\parallel} p_e - Q_e \end{aligned} \quad (2.5.4)$$

Each term on the right hand side of Eq. (2.5.1-2.5.4) has a corresponding term in another equation balancing each other, representing a transfer of energy from one form to another. The energy theorem in integral form shows then, that the energy is perfectly conserved in the whole system:

$$\begin{aligned}
& \frac{\partial}{\partial t} \int dV \left[\frac{1}{2} n m_i \mathbf{v}_{E \times B}^2 + \frac{n m_e}{2} \left(\frac{j_{\parallel}}{en} \right)^2 + \frac{1}{2} n m_i u_{\parallel i}^2 + \frac{3}{2} p_e + \frac{1}{8\pi} (|\nabla_{\perp} A_{\parallel}|^2) \right] = \\
& - \int dV \nabla \cdot \left[\frac{1}{2} n M_i \mathbf{v}_{E \times B}^2 \mathbf{u}_i + \phi \mathbf{j} + \frac{1}{2} m_i n u_{\parallel i}^2 \mathbf{u}_i + \frac{3}{2} \mathbf{v}_{E \times B} p_e + \frac{5}{2} p_e v_{\parallel e} \mathbf{b} \right. \\
& \left. - \frac{5}{2} \frac{c}{B^2} \mathbf{B} \times \nabla \frac{p_e T_e}{e} + \mathbf{v}_{E \times B} p_e - q_{\parallel e} \mathbf{b} + \frac{1}{2} n m_e \left(\frac{j_{\parallel}}{en} \right)^2 \mathbf{v}_{e\parallel} - \frac{\nabla_{\perp} A_{\parallel}}{4\pi} \frac{\partial}{\partial t} A_{\parallel} \right] = 0
\end{aligned} \tag{2.5.5}$$

The remaining sinks and sources for the energy are the terms under the divergence, which are in fact energy flows over the boundaries of the integration domain.

2.6 DEBYE SHEATH BOUNDARIES

In the SOL charged particles moving along the magnetic field line hit the solid surface of the divertor or limiter. This interaction between the plasma and a solid surface is crucial for the local plasma dynamics. The solid acts as a plasma sink. The electrons and ions recombine on the wall and are injected back into the plasma as neutrals. The mass difference between the electrons and the ions leads to a large space-charge electrostatic potential ϕ which occurs in a narrow region of the order of a Debye length $\lambda_D = \sqrt{T_e / (4\pi n_e e^2)}$ caused by the accumulation of the electrons at the wall. The accumulation of the electrons on the surface proceeds until an equilibrium state is reached such that only very fast electrons can overcome the potential drop. In contrast the ions are accelerated by the same potential towards the wall. An ambipolar flow to the wall, meaning an equal flux of electrons and ions to the wall occurs. This region is called 'sheath plasma'. The typical length of the Debye sheath for a hydrogen plasma with the density $n_e = n_i = 10^{19} m^{-3}$ and $T_e = T_i = 10 eV$ is $\lambda_D = 10^{-5} m$. The quasi-neutrality does not hold in the Debye sheath, see figure 2.6.1. Although the thickness of this region is very small, it influences the rest of the plasma, where quasi-neutrality holds. Here we are following the calculation in [8] for the cold ion case. Assuming that the electrons are following a Maxwellian distribution in the

sheath, because they are in an almost perfect force balance and no sources or sinks are present, one obtains for the electron density

$$n_e = n_{se} \exp[e(\phi - \phi_{se})/kT_e] \quad (2.6.1)$$

The reference potential is set to zero in some distance to the sheath. ϕ_{se} describes the potential drop at the sheath entrance 'se'. For the solution of the pre-sheath potential drop simple energy and particle conservation properties of the sheath are applied. Finding the potential drop transforms into finding the sheath entrance velocity v_{se} which is obvious from

$$\frac{1}{2} m_i v_{se}^2 = -e\phi_{se} \quad (2.6.2)$$

All ions are assumed to start at the same position upstream of the sheath edge and it is further assumed that the ions travel collisionlessly over the potential drop. Particle conservation states that $n_{se} v_{se} = n_i v_i$ giving

$$n_i = n_{se} (\phi_{se}/\phi)^{\frac{1}{2}} \quad (2.6.3)$$

Now Eq. (2.6.1) and Eq. (2.6.3) are inserted into the Poisson equation $d^2/dx^2\phi = -e(n_i - n_e)/\epsilon_0$ giving

$$\frac{d^2}{dx^2}\phi = -en_{se} [(\phi_{se}/\phi)^{\frac{1}{2}} - \exp(e(\phi - \phi_{se})/kT_e)]/\epsilon_0 \quad (2.6.4)$$

Linearizing the square root and the exponential terms yields

$$\frac{d^2}{dx^2}(\phi_{se} - \phi) \approx -en_{se}(\phi_{se} - \phi) \left[\frac{e}{kT_e} - \frac{1}{2|\phi|} \right] / \epsilon_0 \quad (2.6.5)$$

In order to exclude non-oscillatory solutions, which would be unphysical, the expression in the bracket need to fulfill

$$\frac{e}{kT_e} \geq \frac{1}{2|\phi|} \quad (2.6.6)$$

which finally gives the Bohm-condition

$$v_{se} \geq c_s \quad (2.6.7)$$

for the ions velocity along the sheath. Taking into account continuity of fluxes and the subsonic dynamics of the plasma, it follows at the sheath

entrance $v_i = c_s$. The situation is summarized in figure 2.6.1. With this condition it is now possible to calculate the wall potential ϕ_w using the ambipolar flow condition $\Gamma_i^w = \Gamma_e^w$. The electron flux on the wall is obtained via the distribution function in the half-velocity space [8] (positive towards the wall)

$$\Gamma_e^w = n_{e,w} \sqrt{\frac{kT_e}{2\pi m_e}} \quad (2.6.8)$$

This flux must be equal to the ion flux and both are equal to the flux entering the sheath $n_{se}c_s$. Using a Boltzmann relation for the wall density $n_{e,w} = n_{se} \exp[e\phi_w/kT_e]$ the wall potential relative to the plasma potential ($\phi = 0$) follows as

$$\phi_w = \frac{kT_e}{e} \ln\left(\sqrt{2\pi \frac{m_e}{m_i}}\right) \quad (2.6.9)$$

This sets a boundary condition on the parallel current $j_{\parallel}^w = e(\Gamma_i^w - \Gamma_e^w)$ giving

$$j_{\parallel}^w = \pm n_{se} c_s e \left[1 - \exp\left(\Lambda - \frac{e\phi_{se}}{kT_e}\right)\right] \quad (2.6.10)$$

with the parameter $\Lambda = \ln\left(2\pi \frac{m_i}{m_e}\right)$, which is between 2 and 3 for a typical plasma. It is important to emphasize that the Debye sheath is collisionless [8] meaning that a fully kinetic approach is necessary in order to resolve this region [59]. However in fluid codes the effect of the sheaths is captured via the boundary conditions Eq. (2.6.10) and (2.6.7) and modification of them [61, 62].

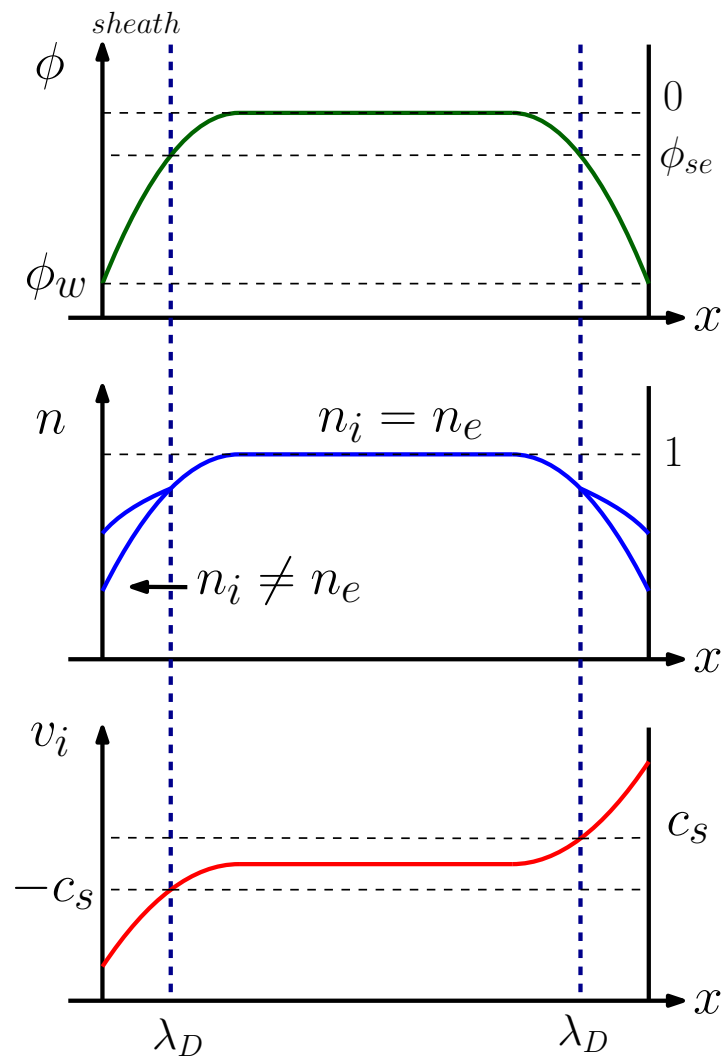


Figure 2.6.1: The potential drop ϕ_{se} breaks the quasi-neutrality in the sheath region forcing the ions $v_{se} \geq c_s$.

2.7 ADDITIONAL SIMPLIFICATION AND ITS IMPLICATIONS

In addition to the drift approximation further simplifications are still needed in order to make the system relative simple to solve from a numerical point of view. As mentioned before, the polarization drift is very small. However the divergence of it is not, thus we neglect the polarization drift if it is in front of a divergence. This simplifies the system, because now one does not have to keep track of the time dependent polarization in the equations. It should be noted that this affects the energy conservation properties of the system by introducing new terms in the energy theorem.

The other simplification is the already mentioned Boussinesq approximation which was relaxed in GRILLIX during this thesis. In the following the subtle impact of these two simplifications is going to be discussed.

2.7.1 *New advective derivative*

We neglect the polarization drift in the ion advective derivative in the perpendicular force balance calculation giving

$$\frac{d^i}{dt} = \frac{\partial}{\partial t} + (\mathbf{v}_{E \times B} + u_{\parallel i} \mathbf{b}) \cdot \nabla = \frac{\partial}{\partial t} + \mathbf{u}_i \cdot \nabla. \quad (2.7.1)$$

This approximation leads to new terms on the right side of Eq. (2.5.5)

$$\dots = \int dV \frac{1}{2} m_i (u_{\parallel i}^2 + \mathbf{v}_{E \times B}^2) \nabla \cdot (n \mathbf{v}_p),$$

indicating that the energy is not conserved anymore. This is the price for the simplifications of the equations for numerical purposes. However these terms are very small, which will be shown in section 3.2.2.

2.7.2 *Boussinesq approximation*

The Boussinesq approximation is widely used in the plasma turbulence community. The main point of it is the assumption that the fluctuations of the density are very small. This assumption is problematic for several reasons. First as was pointed out in the introduction of this chapter, this does not hold in the SOL. Moreover models which make use of the Boussinesq approximation are not global in a strict sense. They are a hybrid between a model where no assumptions about the density are made (e.g. continuity equation) and a model which makes explicit assumptions about the fluctuation

level of the density in the vorticity equation. However, the use of different assumptions in a coupled system of equations is not consistent. The main motivation for the Boussinesq approximation is not of physical nature but rather the numerical solution of the vorticity equation becomes much easier within this approximation. Thus the relaxation of the Boussinesq approximation is of crucial importance on the way towards a model and a code suitable for the SOL. In previous works different forms of the Boussinesq approximation can be found. The first form is called here the conservative Boussinesq approximation.

Conservative form

The conservative Boussinesq approximation was used e.g. in [28,29,44]. One neglects the spatial and temporal dependence of the density ($n \rightarrow n_0 = 1$) in the polarization part of the vorticity equation leading to a simplification:

$$n_0 \nabla \cdot \mathbf{v}_p = \nabla \cdot \left(n \mathbf{v}_{De} - \frac{j_{\parallel}}{e} \mathbf{b} \right) \rightarrow \nabla \cdot \mathbf{j} = 0 \quad (2.7.2)$$

This form of the Boussinesq approximation keeps the charge conservation properties of the system. An energy theorem can be constructed within the conservative Boussinesq approximation giving a modified perpendicular kinetic energy

$$\frac{\partial}{\partial t} \left[\frac{1}{2} \frac{n_0}{B^2} |\nabla_{\perp} \phi|^2 \right] = (\phi \mathbf{v}_{E \times B} + \phi u_{\parallel i} \mathbf{b}) \cdot \nabla \omega - \phi \nabla \cdot \left(\frac{j_{\parallel}}{e} \mathbf{b} \right) + \phi \nabla \cdot (n \mathbf{v}_{De}), \quad (2.7.3)$$

where the vorticity is $\omega = \nabla_{\perp}^2 \phi$. First the perpendicular kinetic energy becomes independent of n . Second additional terms arise on the right side having no counterpart in the total energy theorem, indicating a loss of energy conservation. In order to bring Eq. (2.7.3) to a conserved form, one has to neglect the advection by parallel ion velocity

$$u_{\parallel i} \mathbf{b} \cdot \nabla \omega = 0, \quad (2.7.4)$$

which is problematic on open magnetic field lines where parallel velocity can reach the sound velocity (see section 2.6). Furthermore, one has to assume that the divergence of the $E \times B$ -drift is negligible, such that

$$\phi \mathbf{v}_{E \times B} \cdot \nabla \omega = \nabla \cdot [\phi \omega \mathbf{v}_{E \times B}] - \underbrace{\omega \mathbf{v}_{E \times B} \nabla \cdot \phi}_{=0} - \underbrace{\omega \phi \nabla \cdot \mathbf{v}_{E \times B}}_{\approx 0}, \quad (2.7.5)$$

where the second term vanishes because of a vector identity. Eq. (2.7.5) does not hold in general. This gives the perpendicular kinetic energy in the Boussinesq approximation depending only on surface terms taking into account counterparts from other energies

$$\frac{\partial}{\partial t} \left[\frac{1}{2} \frac{n_0}{B^2} |\nabla_{\perp} \phi|^2 \right] + \nabla \cdot [\phi \omega \mathbf{v}_{E \times B}] = 0 \quad (2.7.6)$$

Consequently the conservative Boussinesq approximation is much more than just neglecting spatial and temporal dependence of the density in the vorticity equation. It requires two more strong assumptions which are not generally satisfied in the edge region and realistic geometries. Nevertheless charge is conserved and the perpendicular delta-f energy has to be equal to the right side of Eq. (2.7.3). From this perspective the second form of the Boussinesq approximation, which is called here non-conservative Boussinesq approximation, is more problematic.

Non-conservative form

Another possibility of using the Boussinesq approximation is keeping the spatial and temporal dependence of the density in the polarization part of the vorticity equation

$$n \nabla \cdot \mathbf{v}_p = \nabla \cdot \left(n \mathbf{v}_{De} - \frac{j_{\parallel}}{e} \mathbf{b} \right) \rightarrow \nabla \cdot \mathbf{j} \neq 0 \quad (2.7.7)$$

This clearly breaks the charge conservation of the entire system! A consequence of this is that no energy theorem can be constructed anymore and the conservation properties are completely lost. This form of the Boussinesq approximation was used in other models such as [21–23, 63, 64].

The impact of the non-conservative Boussinesq approximation will be discussed in the section 3.2.

Summary

In this section the model which is finally implemented in GRILLIX was derived. Starting from the Braginskii equations, many simplifications needed to be applied in order to bring the system into a form which can be solved numerically. We employ the drift approximation and assume cold ions. It was shown that the chosen model conserves energy. The subtle impact of the conservative form of the Boussinesq approximation was discussed. The conservative Boussinesq approximation leads to a modified energy theorem, however it keeps the charge conservation. In contrast the non-conservative form of the Boussinesq approximation (which can be still found in recent works) breaks completely the conservation properties of the model. The Boussinesq approximation is not suitable for the treatment of the SOL and its use is not consistent with the rest of the global electromagnetic model, where no assumptions about the density are made. In GRILLIX the Boussinesq approximation was relaxed. The comparison between the full model and the Boussinesq approximation will be discussed in the next section.

2.8 NUMERICAL IMPLEMENTATION

In this section the numerical implementation of the final set of equations is discussed. An important point is the chosen geometry. As was discussed before, the powerful feature of GRILLIX is the treatment of realistic geometries. However this is an additional layer of complexity during the model development. Here the focus is on the correct model discretization, implementation and verification. For this purpose a simple slab geometry is chosen. In order to discretize the equations we use finite difference methods [65]. The spatial and temporal discretization of each operator is shown. Before doing this the model needs to be normalized. Special attention is required for the relaxation of the Boussinesq approximation. The discretization of the corresponding operators is discussed. The results can be easily transferred to more complex geometries using the flux-coordinate independent approach, see chapter 4.

2.8.1 Geometry

In the following a 3D flux tube set up is chosen as the computational domain, see figure 2.8.1. The flux box follows the magnetic field lines across the circular domain of the tokamak hitting the limiter plates. The coordinate system (x, z, y) for the slab geometry consists of the radial coordinate x , the poloidal coordinate y , where periodic boundary conditions are applied and the coordinate z which is parallel to the magnetic field lines, where Bohm boundary conditions are used, see the discussion on boundary conditions in section 2.6. Alternatively periodic boundary conditions can be applied. The direction of the curvature of the magnetic field is denoted by κ . The flux box is unwound to a straight box having the length L_{\parallel} , see figure 2.8.2. Although the magnetic field lines are straight, the curvature can still be modeled yielding a flux box around the torus with a low-field side (LFS) and high-field side (HFS). Without the curvature a linear device can be modeled within this set up. Despite the simplicity of the geometry many phenomena can be studied e.g. blob dynamics (chapter 3.1), basic plasma turbulence (chapter 3.2 - 3.3), conservation properties of the model (section 3.2.2) and electromagnetic effects (section 3.2.1). For more complex geometries which are going to be investigated in chapter 4 the coordinate system is given by (R, φ, Z) with the poloidal angle θ and the toroidal angle φ .

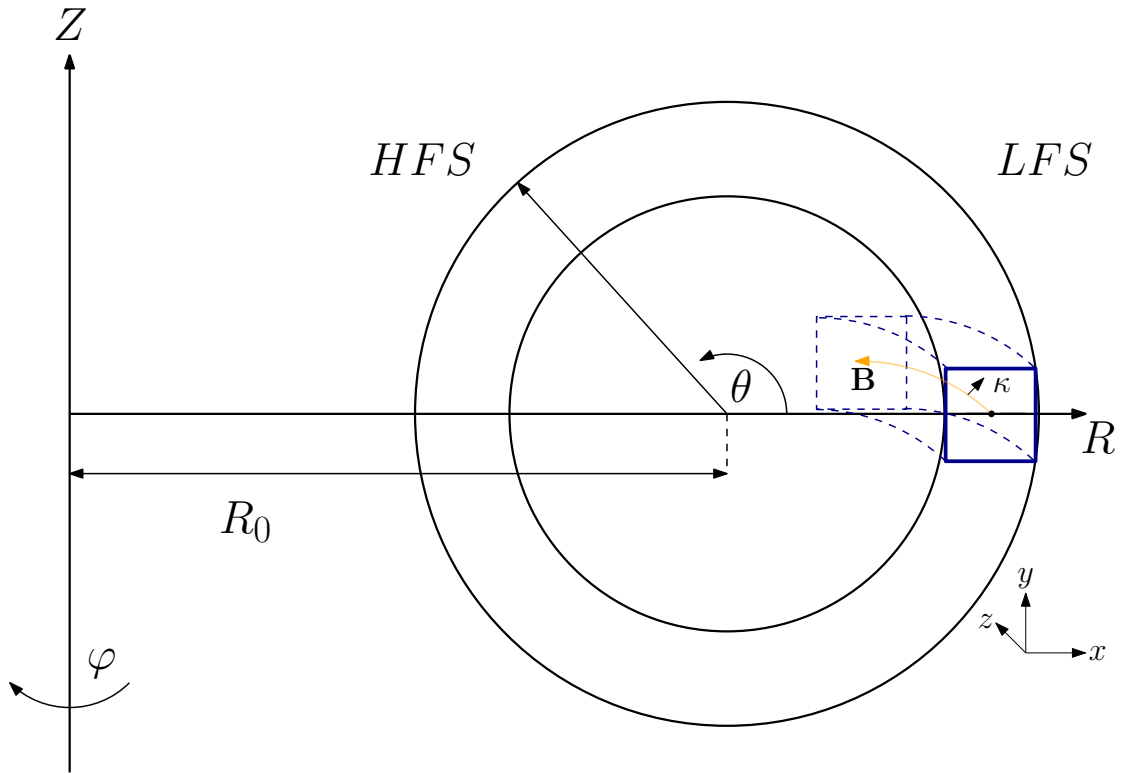


Figure 2.8.1: A 3D flux tube following the magnetic field lines around the torus.

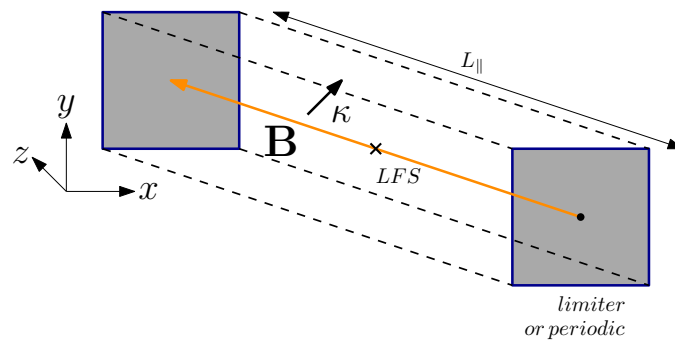


Figure 2.8.2: The flux box is unwound to a straight slab geometry, which still captures the curvature effects.

2.8.2 Normalization

The set of equations (2.4.1),(2.4.2),(2.4.5),(2.4.9),(2.4.10) is normalized according to

$$\begin{aligned}\tilde{t} &= \frac{c_s^0}{R} t, \quad \tilde{x}_\perp = \frac{x_\perp}{\rho_{s0}}, \quad \tilde{n} = \frac{n}{n_0}, \quad \tilde{\phi} = \frac{e\phi}{T_0}, \quad \tilde{\mathbf{B}} = \frac{\mathbf{B}}{B_0}, \\ \tilde{u}_\parallel &= \frac{u_\parallel}{c_{s0}}, \quad \tilde{j}_\parallel = \frac{j_\parallel}{c_s^0 e n_0}, \quad \tilde{x}_\parallel = \frac{x_\parallel}{R_0}, \quad \tilde{T}_e = \frac{T_e}{T_{e0}}, \quad \tilde{A}_\parallel = \frac{A_\parallel}{\beta_0 B_0 \rho_{s0}}.\end{aligned}$$

The normalized quantities are on the left side under tilde, which will be dropped in the following for clarity and conciseness. The perpendicular direction is normalized with the ion sound radius $\rho_{s0} = c\sqrt{T_{e0}m_i}/eB_0$. Time is measured in terms of $\frac{R_0}{c_s^0}$ with the sound speed $c_s^0 = \sqrt{T_{e0}/m_i}$ and the major radius of the tokamak R_0 . The density, the magnetic field and the electron temperature are normalized to some reference values n_0, B_0, T_{e0} , respectively. In order to ensure the positivity of the density and electron temperature we want to develop instead of n and T_e the logarithm of these quantities. In the following we use $\theta_n = \log(n)$ and $\theta_T = \log(T_e)$. For this reason the continuity equation and the temperature equation are divided by n and T_e respectively. The normalized set of equations is given by:

Continuity equation

$$\frac{\partial}{\partial t}\theta_n + \frac{\delta}{B}\{\phi, \theta_n\} = C(\phi) - C(p_e) - \frac{1}{n}\nabla \cdot nu_{\parallel i}\mathbf{b} - \frac{1}{n}\nabla \cdot j_{\parallel}\mathbf{b} \quad (2.8.1)$$

Vorticity

$$\begin{aligned}\nabla_\perp \cdot \left[\frac{n}{B^2} \frac{\partial}{\partial t} \nabla_\perp \phi \right] + \frac{\delta}{B} \nabla_\perp \cdot \left(\frac{n}{B^2} \{\phi, \nabla_\perp \phi\} \right) &= -C(p_e) + \nabla \cdot j_{\parallel}\mathbf{b} \\ &\quad - \nabla_\perp \cdot \left(\frac{n}{B^2} u_{\parallel i} \nabla_\parallel \nabla_\perp \phi \right)\end{aligned} \quad (2.8.2)$$

Parallel ion momentum

$$\frac{\partial}{\partial t}u_{\parallel} + \frac{\delta}{B}\{\phi, u_{\parallel i}\} = -u_{\parallel i}\nabla_\parallel u_{\parallel i} - \frac{1}{n}\nabla_\parallel p_e \quad (2.8.3)$$

Electron temperature

$$\begin{aligned} \frac{\partial}{\partial t} \theta_T + \frac{\delta}{B} \{ \phi, \theta_T \} &= \frac{2}{3} (C(\phi) - \frac{7}{2} C(T_e) - T_e C(\theta_n)) + \frac{2 \cdot 0.71}{3} \frac{1}{n} \nabla \cdot j_{\parallel} \mathbf{b} - \frac{2}{3} \nabla_{\parallel} v_{\parallel e} \\ &\quad - v_{\parallel e} \nabla_{\parallel} \theta_T + \frac{2}{3} \frac{1}{n T_e} \frac{j_{\parallel}^2}{\sigma_{\parallel}} + \frac{2}{3} \frac{1}{n T_e} \nabla \cdot \kappa_{\parallel e} \nabla_{\parallel} T_e \end{aligned} \quad (2.8.4)$$

Ohm's law

$$\beta_0 \frac{\partial}{\partial t} A_{\parallel} + \mu \left[\frac{\partial j_{\parallel}}{\partial t} + \frac{\delta}{B} \left\{ \phi, \frac{j_{\parallel}}{n} \right\} + v_{\parallel e} \nabla_{\parallel} \frac{j_{\parallel}}{n} \right] = - \frac{j_{\parallel}}{\sigma_{\parallel}} - \nabla_{\parallel} \phi + T_e \nabla_{\parallel} \theta_n + 1.71 \nabla_{\parallel} T_e \quad (2.8.5)$$

The $E \times B$ -advection of some quantity f can be written with the help of the Poisson bracket

$$\mathbf{v}_{E \times B} \cdot \nabla f = \frac{\delta}{B} (\partial_x \phi \partial_y f - \partial_y \phi \partial_x f) := \frac{\delta}{B} \{ \phi, f \} \quad (2.8.6)$$

$C(f)$ denotes the curvature operator which is given by

$$C(f) = -2\partial_y f \quad (2.8.7)$$

The parallel electron velocity is written as

$$v_{\parallel e} = u_{\parallel i} - \frac{j_{\parallel}}{n} \quad (2.8.8)$$

The free parameters of the system are given by

$$\delta = R_0 / \rho_s, \quad \sigma_{\parallel}^0 = \frac{c_s^0}{R_0} \frac{m_i}{m_e} \frac{1}{0.51 v_e^0}, \quad \kappa_{\parallel e0} = 3.15 \frac{c_{s0}}{R_0} \frac{m_i}{m_e} \tau_{e0}, \quad \beta_0 = \frac{4\pi n_0 T_{e0}}{B_0^2}, \quad \mu = \frac{m_e}{m_i}$$

determining the $E \times B$ -advection, the parallel conductivity $\sigma_{\parallel} = \sigma_{\parallel 0} \cdot T_e^{\frac{3}{2}}$ and the parallel heat conduction $\kappa_{\parallel e} = \kappa_{\parallel e0} \cdot T_e^{\frac{5}{2}}$.

2.8.3 Sources, Dissipation and radial boundary conditions

In order to ramp up plasma density and electron temperature source terms $S_{n,t}$ are added. We can choose between two kind of sources. The first one is a source with a constant rate in time. The second source ramps up the quantities to a defined target density and electron temperature respectively. In addition to that, hyper-diffusion $D(f) = \nabla_{\perp}^{2k} f$ with $k = 1, 2, \dots$ is applied on all quantities in perpendicular direction in order to damp high k_{\perp} structures on the grid scale. This stabilizes the simulation since it prevents the power spectrum from piling up at higher frequencies. In parallel direction a weak normal diffusion is applied acting also on the grid scale.

Radial boundary conditions are chosen according to Dirichlet or homogeneous Neumann conditions on all quantities. In addition to these the Bohm boundary conditions in parallel direction can be applied. The density, vorticity and electric potential are extrapolated linearly at the parallel boundaries $\nabla_{\parallel}^2 f|_{Boundary} = 0$ and Neumann boundary condition is applied on the electron temperature in parallel direction.

2.8.4 Discretization

In this section the normalized set of equations (2.8.1)-(2.8.5) is going to be discretized. The discretization is discussed for the parallel and perpendicular operators respectively.

Parallel operators

For the discretization of the parallel operators along the magnetic field line (\mathbf{e}_z) a grid G with the integer indices $k = 0, 1, 2, \dots$ and a staggered grid G^* having half-integral indices $k^* = \frac{1}{2}, \frac{3}{2}, \dots$ is introduced, see figure 2.8.3.

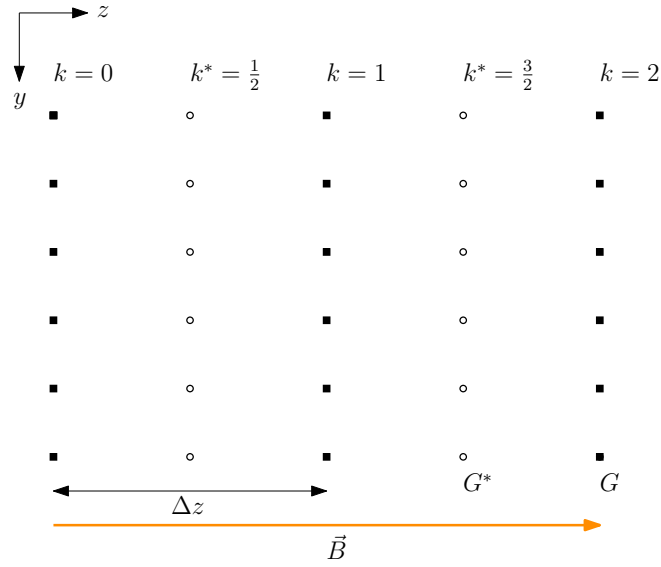


Figure 2.8.3: The grid is shown in parallel direction. The staggered grid G^* is shifted by $\frac{\Delta z}{2}$ compared to the grid G .

PARALLEL GRADIENT The discrete parallel gradient is an operator \mathbf{Q} which maps from the grid G to the staggered grid G^* :

$$\mathbf{Q} : G \rightarrow G^*.$$

For some quantity f which exists on the grid G the parallel gradient \mathbf{q}^{\parallel} which is defined on the staggered grid G^* is written in discretized form as:

$$\mathbf{q}^{\parallel}_{k^*} := (\mathbf{Q}f)_{k^*} := \frac{f_{k+1} - f_k}{\Delta z}, \quad (2.8.9)$$

where $\Delta z = \frac{L_{\parallel}}{N}$ with N being the number of poloidal planes.

PARALLEL DIVERGENCE Analogously, the parallel divergence is an operator of type \mathbf{Q}^* meaning that it maps from the staggered grid G^* to G :

$$\mathbf{Q}^* : G^* \rightarrow G.$$

The discrete form of the parallel divergence \mathbf{d}^{\parallel} is written in the form:

$$\mathbf{d}^{\parallel}_k := [\mathbf{Q}^*(\mathbf{Q}f)]_k := \frac{(\mathbf{Q}f)_{k^*+1} - (\mathbf{Q}f)_{k^*}}{\Delta z}. \quad (2.8.10)$$

MAPPING OPERATORS For objects like e.g. $f_k(\mathbf{Q}f)_{k^*}$ or $f_{k^*}(\mathbf{Q}f)_{k^*}$ where the quantity f exists on the grid G or G^* whereas the gradient is applied on the staggered grid G^* a mapping operator \mathbf{M} is needed to bring only the gradient to G , f to G^* or the product to G :

$$\begin{aligned}\mathbf{M} : G &\rightarrow G^*, \\ \mathbf{M}^* : G^* &\rightarrow G.\end{aligned}$$

A quantity f is mapped from the grid G to the staggered grid G^* in the following way

$$(\mathbf{M}f)_{k^*} = \frac{1}{2}(f_{k+1} + f_k). \quad (2.8.11)$$

Accordingly the gradient is mapped from the staggered grid G^* to the grid G

$$(\mathbf{M}^*(\mathbf{Q}f)_{k^*})_k = \frac{1}{2}((\mathbf{Q}f)_{k^*+1} + (\mathbf{Q}f)_{k^*}). \quad (2.8.12)$$

Perpendicular operators

Within the poloidal planes ($\mathbf{e}_x, \mathbf{e}_y$) operators are discretized on the grid G with the indices $i, j = 0, 1, 2, \dots$ with standard finite differences. In addition to that a staggered grid G_\perp^* is introduced having the half-integral indices $i^*, j^* = \frac{1}{2}, \frac{3}{2}, \dots$, see figure 2.8.4. All perpendicular operators are discretized and mapped in the same fashion like the parallel operators.

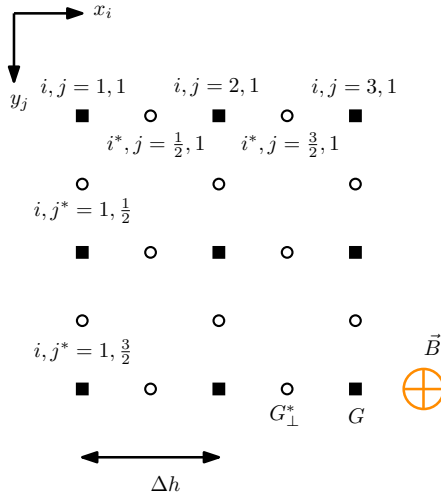


Figure 2.8.4: The grid in the poloidal planes. The staggered grid G_\perp^* is shifted by $\frac{\Delta h}{2}$ compared to the grid G .

PERPENDICULAR GRADIENT The perpendicular gradient is an operator \mathbf{P} which maps from the grid G to the perpendicular staggered grid G_{\perp}^* :

$$\mathbf{P} : G \rightarrow G_{\perp}^*.$$

The perpendicular gradient $\mathbf{p}_{k,i,j}^{\perp}$ is defined on G_{\perp}^* and can be written as

$$\mathbf{p}_{k,i^*,j}^{\perp} := (\mathbf{P}f)_{k,i^*,j} := \frac{f_{k,i+1,j} - f_{k,i,j}}{\Delta h}, \quad (2.8.13)$$

where the grid spacing is $\Delta h = \frac{L_{\perp}}{N_{\perp}}$ with N_{\perp} being the number of poloidal grid points. Here only the radial direction is shown but the same approach holds obviously for the poloidal direction as well.

PERPENDICULAR DIVERGENCE Another form of operators \mathbf{P}^* is introduced within the poloidal planes which map the quantities from the staggered grid G_{\perp}^* to grid G :

$$\mathbf{P}^* : G_{\perp}^* \rightarrow G.$$

The perpendicular divergence is written consequently in the following form

$$\mathbf{1}_{k,i,j}^{\perp} := [\mathbf{P}^*(\mathbf{P}f)]_{k,i,j} := \frac{(\mathbf{P}f)_{k,i^*+1,j} - (\mathbf{P}f)_{k,i^*,j} + (\mathbf{P}f)_{k,i,j^*+1} - (\mathbf{P}f)_{k,i,j^*}}{\Delta h}. \quad (2.8.14)$$

PERPENDICULAR MAPPING OPERATORS Perpendicular mapping operators are introduced bringing the quantity to G or G_{\perp}^* :

$$\begin{aligned} \mathbf{M}_{\perp} : G &\rightarrow G_{\perp}^*, \\ \mathbf{M}_{\perp}^* : G_{\perp}^* &\rightarrow G. \end{aligned}$$

A quantity f is mapped from the grid G to the staggered grid G_{\perp}^* in the following way

$$(\mathbf{M}_{\perp}f)_{k,i^*,j} = \frac{1}{2}(f_{k,i+1,j} + f_{k,i,j}). \quad (2.8.15)$$

Therefore the gradient is mapped from the staggered grid G_{\perp}^* to the grid G

$$(\mathbf{M}^*(\mathbf{P}f)_{k,i^*,j})_{k,i,j} = \frac{1}{2}((\mathbf{P}f)_{k,i^*+1,j} + (\mathbf{P}f)_{k,i^*,j}). \quad (2.8.16)$$

Now the set of equations can be written in a systematic way. The density n , the electron temperature T_e and the potential ϕ are derived on the grid G .

The parallel current j_{\parallel} and the parallel ion velocity $u_{\parallel i}$ are calculated on the staggered grid G^* .

Special operators

EXB-ADVECTION The $E \times B$ -advection $\mathbf{v}_{E \times B} \cdot \nabla f = \{\phi, f\}$ acts purely in the poloidal plane. For the discretization of the Poisson bracket $\{\phi, f\}$ we use the conservative Arakawa scheme [66] and use in the following the notation $[\phi, f]$.

NON-BOUSSINESQ ADVECTION Special attention was required for the relaxation of the Boussinesq approximation and discretization of the operators $\nabla_{\perp} \cdot (n[\phi, \nabla_{\perp} \phi])$ and $\nabla \cdot (nu_{\parallel i} \nabla_{\parallel} \nabla_{\perp} \phi)$ in the vorticity equation. In the first one the perpendicular gradient of ϕ exists on the perpendicular staggered grid G_{\perp}^* . This means that the potential needs to be mapped to the staggered grid. The Arakawa bracket is then evaluated on the staggered grid $[\mathbf{M}_{\perp} \phi, \mathbf{P} \phi]$. For the product with n , the density is mapped to the staggered grid as well $\mathbf{M}_{\perp} n[\mathbf{M}_{\perp} \phi, \mathbf{P} \phi]$. Finally the divergence brings the quantity back to the full perpendicular grid G , $\mathbf{P}^*(\mathbf{M}_{\perp} n[\mathbf{M}_{\perp} \phi, \mathbf{P} \phi])$. This procedure is necessary because otherwise the stencil jumps over neighboring grid points, a phenomenon known as checker boarding.

For the second operator the parallel gradient is interchanged with the perpendicular gradient writing $\nabla_{\perp} \cdot (nu_{\parallel i} \nabla_{\perp} \nabla_{\parallel} \phi)$. The parallel gradient of ϕ is mapped to the grid G where the perpendicular gradient is evaluated $\mathbf{P} \mathbf{M}^* \mathbf{Q} \phi$. The parallel ion velocity is mapped to the full grid, where the product $nu_{\parallel i}$ is evaluated, which is mapped to G_{\perp}^* , $\mathbf{M}_{\perp} n(\mathbf{M}^* u_{\parallel i}) \mathbf{P} \mathbf{M}^* \mathbf{Q} \phi$. The perpendicular divergence brings the quantity back to the full grid $\mathbf{P}^* \mathbf{M}_{\perp} n(\mathbf{M}^* u_{\parallel i}) \mathbf{P} \mathbf{M}^* \mathbf{Q} \phi$. A consistent discrete form of the full electromagnetic system of equations could be only reached with the use of staggered grids and the discussed procedure.

As an example the discrete continuity equation is shown here on the discrete level.

Continuity equation

$$\frac{\partial}{\partial t} \theta_n + \delta[\phi, \theta_n] = C(\phi) - \frac{1}{n} C(p_e) - \mathbf{M}^*(u_{\parallel i} \mathbf{Q} \theta_n) - \mathbf{Q} u_{\parallel i} + \frac{1}{n} \mathbf{Q}^* j_{\parallel} + \frac{D(n)}{n} + \frac{S_n}{n} \quad (2.8.17)$$

The diffusion term is given by $D(f) = D_{\perp}(f) + D_{\parallel}(f) = \mathbf{Q}^* \mu_{\parallel} \mathbf{Q} f + \mathbf{P}^* \mu_{\perp} \mathbf{P} f$.

2.8.5 Time-Stepping scheme

For the time propagation a 3rd order backward differentiation formula (BDF3) is used [67]. In the earlier Hasegawa-Wakatani version of the code the BDF3 scheme was already used. It has proven to be numerically stable and performed well concerning conservation of energy. The scheme has the following form

$$f_{t+1} = \frac{18}{11}f_t + \frac{9}{11}f_{t-1} + \frac{2}{11}f_{t-2} + \frac{6}{11}dt F(t+1, f_{t+1}). \quad (2.8.18)$$

Consequently three time points per each quantity need to be stored in the memory. The function $F(t+1, f_{t+1})$ contains all discrete operators at the time step $t+1$. Thus BDF3 is an implicit time scheme. An implicit treatment of nonlinearities is a difficult task thus the operators on the right hand side at the time-step $t+1$ are extrapolated out of the previous three time-steps

$$F(t+1, f_{t+1}) = 3F(t, f_t) - 3F(t-1, f_{t-1}) + F(t-2, f_{t-2}), \quad (2.8.19)$$

where df_t is the sum of all discrete operators on the right hand side of the model.

2.8.6 Helmholtz solver

In GRILLIX solutions to equations of the Helmholtz type

$$\lambda u - \nabla \cdot [c \nabla_{\perp} u] = b \quad \text{in } \Omega \quad (2.8.20)$$

have to be determined, where b is some right hand side and Ω is a poloidal plane. In order to get the electrostatic potential out of the vorticity equation (2.8.2) an elliptic equation ($u = \phi, \lambda = 0, c = n$) needs to be solved. The full Helmholtz equation ($u = A_{\parallel}, \lambda = \beta_0, c = 1$) is solved for the vector potential (2.8.5). Eq. (2.8.20) is discretized with finite differences according to section 2.8.4 giving a system of equations $Au = b$. A solution of this system with a direct solver is too costly since a LU -decomposition [68] has to be performed in each time step. Using Splitting methods e.g. Jacobi relaxation, which is a linear iterative method, is also not possible. In order to converge, the iteration matrix M of a linear iterative method needs to fulfill $\rho(M) < 1$ where $\rho(M)$ is the spectral radius. However for the Jacobi relaxation method it holds $\rho(M) - 1 \propto h^2$ [65, 68], where h is the grid resolution. With an increasing resolution the Jacobi relaxation method converges slower. This is the reason

why iterative solvers have no practical applications [65]. In order to accelerate the convergence behavior of the Jacobi relaxation method a multigrid solver is used in GRILLIX, which was developed by A. Stegmeir. Details of the use and implementation are provided in the GRILLIX Documentation [46]. A general introduction to iterative and multigrid solvers can be found in [65,68,69] and more mathematical approach in [70].

The basic idea behind the multigrid approach is the use of multiple grids where the equation reads $A_l u^l = b^l$ with the index l defining the grid resolution $h_l = h_0/2^l$ (h_0 : resolution of the coarsest grid). On the finest grid the Jacobi relaxation method converges too slow, however it smooths the higher frequencies of the numerical error $\epsilon^l = u^l - u^{l,*}$, where u^l and $u^{l,*}$ are the approximated solution after several iterations and the exact solution respectively [68]. The smooth numerical error can be used on a coarser grid (restriction) in order to get the final solution e.g. via a direct solver, which then has to be brought to the finer grid (prolongation). The restriction and prolongation operations can be done in several ways. The trivial restriction simply takes the values of the vector on the coarser grid. A linear restriction interpolates the values on the coarser grid via a linear interpolation out of the neighboring points. In the same fashion the prolongation operation is performed, where the values on the finer grid are computed linearly out of the coarser grid. In GRILLIX a trivial restriction and the bilinear prolongation are used [46]. Instead of prolonging the solution to the finer grid, it can be used as the initial condition for a further restriction to an even coarser grid. The solution on the coarsest level is prolonged all the way up to the finest level. At each level post-smoothing Jacobi iterations are applied. Going directly from the finest to the coarsest level and back defines the so called V -cycle. Similarly, in the W - cycle the solution is restricted and prolonged intermediately several times. The main advantage of multigrid methods is the $O(N)$ computational complexity with the problem size N , which makes it very efficient for large problems [71].

2.8.7 Method of manufactured solutions

In this section the slab version of GRILLIX is verified. The verification process is aimed to check if the chosen set of partial differential equations was discretized, implemented and solved correctly. It does not show whether the chosen numerical methods are applicable to the equations. Our chosen model consists of a nonlinear set of partial differential equation meaning that no analytical solution can be provided. In this sense a comparison between the numerical solution and an analytical result is impossible. The Method of Manufactured solutions (MMS) [72–74] is a technique allowing the verification of a code even without an analytical result. Within this method a known or manufactured solution is provided by adding source terms to the equations. It is checked how close the numerical solution of the equation is to the provided manufactured solution. The difference between the numerically derived solution and the manufactured solution gives the numerical error. Here we will focus on the $L2$ -norm of the numerical error

$$\epsilon_2 = \sqrt{\frac{\sum_{i=1}^N (f_{m,i} - f_{n,i})^2}{\sum_{i=1}^N f_{m,i}^2}}, \quad (2.8.21)$$

where f_m is the manufactured analytical function and f_n is the numerical solution. The sum is taken over all grid points N . With higher spatial resolution the numerical result should approach the manufactured solution with a known scaling in the numerical error e.g. second order for central finite differences. In order to test the correctness of the numerical implementation of a nonlinear equation evolving some quantity f

$$\frac{\partial}{\partial t} f = O(f), \quad (2.8.22)$$

where $O(f)$ is a nonlinear operator acting on f containing the discretized differential operators in the spatial dimensions a time-dependent manufactured function $f_m(t)$ is chosen. This function should be a smooth differentiable general combination of some simple mathematical functions e.g. \sin, \cos and \exp employing all spatial and temporal parts of the code. Here a periodic slab is chosen as the computational domain for testing the method of manufactured solutions. Thus, the chosen function f_m should also be

periodic in the poloidal and toroidal directions. The manufactured function is inserted in Eq. (2.8.22) providing an analytical form of the source function

$$S(t) = \frac{\partial}{\partial t} f_m - O(f_m). \quad (2.8.23)$$

The source function is inserted in the equation giving the new equation which is solved numerically

$$\frac{\partial}{\partial t} f = O(f) + S(t). \quad (2.8.24)$$

Now it is evident that f_m is an exact solution of the new equation (2.8.24). The procedure for the test of the scaling of the numerical error is then as follows. At the start of the simulation $t = 0$ the quantity is set to zero. The time is then advanced to some later point $t = \Delta t$. The source function is an analytical expression which is derived at every time point and provided to the code. After a period of time, which should be long enough in order to let the system reach the manufactured solution, the numerical outcome is compared to f_m . The $L2$ -norm of the numerical error (2.8.21) is computed. This is repeated with the double resolution and the numerical error is derived. If the spatial operators were implemented correctly then the scaling of the numerical error must show the expected order of convergence and decrease towards zero for higher spatial resolutions. The time mesh should also be refined in order to avoid a dominance of the numerical error from the time-discretization for higher spatial resolutions. Here only Dirichlet boundary conditions on the quantities are tested. Analytical expressions $f_m|_{Boundary}$ for the boundary conditions are set in the code within the MMS procedure. The following function is used

$$f(x, y, z, t) = [c_1 \cos(k_1^z z) + s_1 \sin(k_2^z z)] \cdot [c + \sin(\psi + t\omega)] \cdot (2.8.25)$$

$$[e_1 e^{-e_x \cdot \bar{x}} + c_2 \cos(k_1^x \bar{x}) + s_2 \sin(k_2^x \bar{x})] \cdot (2.8.26)$$

$$[c_3 \cos(k_1^y \bar{y}) + s_3 \sin(k_2^y \bar{y})]. \quad (2.8.27)$$

with $\bar{x} = \frac{2\pi(x-x_{min})}{(x_{max}-x_{min})}$, $\bar{y} = \frac{2\pi(y-y_{min})}{(y_{max}-y_{min})}$ and the parameters $c_1, k_1^z, s_1, k_2^z, c, \psi, \omega, e_1, e_x, c_2, s_2, k_1^x, k_2^x, c_3, s_3, k_1^y, k_2^y$. These parameters are set individually for each manufactured solution for the density n_m , the electron temperature $T_{e,m}$, the potential ϕ_m , the parallel ion velocity $u_{||,m}$ and the vector potential $A_{||,m}$. The values are shown in table below.

	c_1	k_1^z	s_1	k_2^z	c	ψ	ω	e_1	e_x	c_2	s_2	k_1^x	k_2^x	c_3	s_3	k_1^y	k_2^y
n_m	0.321	1	0.689	1	0.1	2.34	20	0.68	0.313	0.653	0.543	1	2	0.573	0.684	3	2
$T_{e,m}$	0.269	1	0.412	2	0.06	0.79	18	0.598	0.562	0.389	0.265	3	1	0.165	0.721	1	1
ϕ_m	0.462	2	0.321	1	0.8	0.69	33	0.365	0.468	0.385	0.684	3	1	0.942	0.762	2	1
$u_{ i,m}$	0.984	2	0.176	2	0.2	1.34	23	0.318	0.789	0.798	0.687	1	1	0.156	0.563	3	1
$A_{ m}$	0.756	1	0.985	1	0.15	0.83	27	0.145	0.863	0.462	1.268	2	1	0.724	0.621	1	2

One can test the complete model with the technique which has been discussed. Unfortunately this can lead to a situation where the error of some operator which was implemented in a wrong way is hidden by the numerical error of correctly implemented operators. In order to avoid this situation each part of the equations was tested separately. Here only the result for the complete model is shown, see figure 2.8.5.

Complete model

For the testing of the complete model the poloidal resolution is $h = \frac{1.0}{2^i}$ with $i = 0, 1, 2, 3$ and the toroidal resolution is chosen with $\Delta z = \frac{2\pi}{j}$ with $j = 16, 32, 64, 128$. The physical parameters are in the range of a typical turbulence simulation with $\delta = 680$, $\beta_0 = 10^{-2}$, $\mu = 10^{-3}$, $\sigma_{||0} = 1.2$, $\chi_{||0} = 0.75$. All lines are parallel to each other in figure 2.8.5 and also parallel to the reference 2nd order line indicating a very good second order behavior of the implemented system. A similar result was achieved within an electrostatic model which was published in [75]. From this one concludes that the model was discretized and implemented in a correct way.

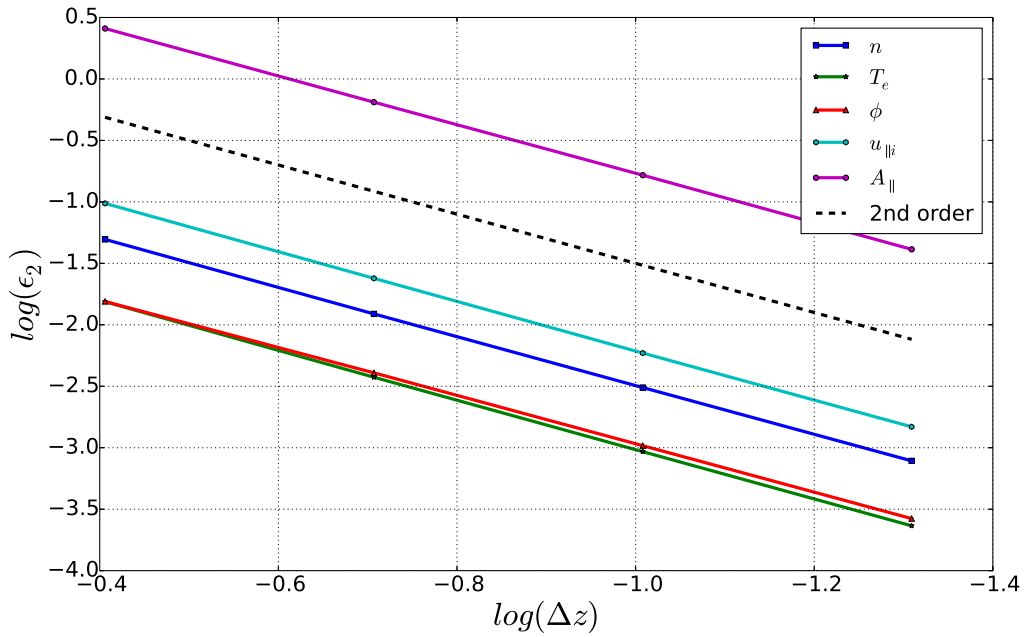


Figure 2.8.5: MMS for the complete electromagnetic model. All quantities show a second order behavior.

Summary

In this section the discretization and implementation of the drift reduced Braginskii model was shown, which is one of the major achievements in this thesis. For this purpose the use of staggered grids in toroidal and poloidal direction was essential. Both the staggered grids and the Helmholtz solver allowed the relaxation of the Boussinesq approximation extending GRILLIX to a global electromagnetic model without any assumptions about the density. For simplicity the discretization and implementation was shown in a magnetic slab geometry, which is a very efficient testing environment for the numerics and physics. The extension to FCI and more complicated geometries will be discussed later in the chapter 4. The important test of the numerics with the method of manufactured solutions showed an excellent second order behavior of the numerical schemes.

SIMULATIONS IN SLAB GEOMETRY

Radial transport of plasma in the SOL of magnetically confined plasmas is found to be turbulent. This turbulence is mainly dominated by filamentary large-amplitude structures in density, the electron temperature and the electric potential known as 'blobs' [76–82]. It is known from the theory and simulation side that these blobs are born as a result of the nonlinear saturation of the underlying edge turbulence instabilities [83]. These coherent structures are spatially localized in the poloidal plane on a lower-density plasma background and are elongated along the magnetic field lines in 3 dimensions. A wide review of blob physics is given in [84–86]. Simple analytical theories, which already yield satisfactory results describing the basic blob dynamics [87–90]. Most of the numerical studies were performed in 2D [91–95]. However blobs are a full 3D phenomenon such that in recent years the new standard became 3D simulations [64, 96–106]. In this chapter the basic blob dynamics is recapitulated. The focus is on the dynamics of the full 3D thermal system, which is a very important test for the model and the implementation of it. The numerical results can be compared to the analytical predictions. The correct description of the blob dynamics is important since plasma turbulence consists mainly of blobs. The scaling laws for the maximum center of mass velocity of a blob are derived and tested. For the first time the simulations are compared to the Boussinesq system in order to identify the regimes where the applicability of the Boussinesq system does not impact the overall dynamics. It is shown that GRILLIX successfully treats the blob dynamics in all regimes.

3.1 BLOB DYNAMICS

In this section the basic blob dynamics which is derived from a simple isothermal 2D model is presented. This helps to understand the polarization mechanism and the convection of the blobs in the SOL. The extension to a 3D thermal model is discussed afterwards.

The basic model consists of the continuity and the vorticity equation

$$\begin{aligned} \frac{\partial}{\partial t} n + \nabla \cdot n(\mathbf{v}_{e\perp} + v_{\parallel e} \mathbf{b}) &= 0, \\ \nabla \cdot \mathbf{j} &= 0, \end{aligned} \quad (3.1.1)$$

where the vorticity equation can be written in the usual form neglecting the parallel advection term using $d/dt = \partial/\partial t + \mathbf{v}_{E \times B} \cdot \nabla$.

$$\nabla_{\perp} \cdot \left[\frac{n}{B^2} \frac{d}{dt} \nabla_{\perp} \phi \right] = \nabla_{\parallel} j_{\parallel} + \nabla \cdot n \mathbf{v}_{De}. \quad (3.1.2)$$

Currents are induced in perpendicular direction by the ion inertia polarization which describes the collective plasma motion according to the vorticity and the diamagnetic plasma drift, which arises due to the curvature of the magnetic field. The diamagnetic drift acts as a source for the vorticity, interchanging high density plasma with low density plasma [86]. The diamagnetic drift polarizes the plasma due to the sign dependence for oppositely charged particles. The density structure shown in figure 3.1.1 is polarized due to the interchange drive in Eq. (3.1.2) which consequently produces an electric field perpendicular to the magnetic field. This causes an $E \times B$ -advection of the complete structure.

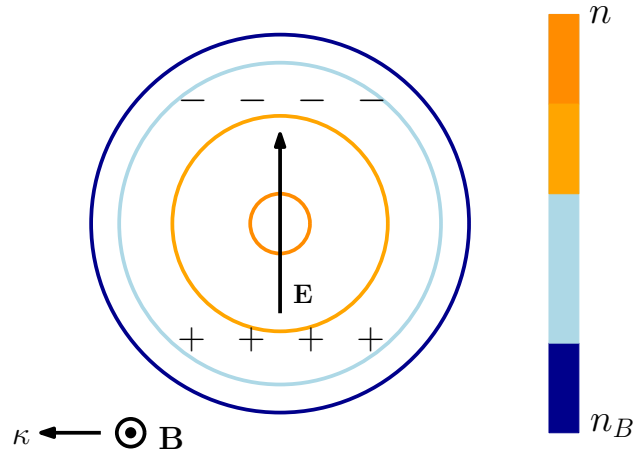


Figure 3.1.1: The blob is polarized due to the interchange drive. An electric field arises which is perpendicular to \mathbf{B} and the curvature κ causing the $E \times B$ -advection of the entire structure. Contours show areas with equal density ranging from the background density n_B to the maximum blob density n .

The dynamics of the blob depends highly on the balancing of the induced current. From Eq. (3.1.2) it is evident that the last term on the right hand side can be balanced by the inertial term (inertial regime) on the left side or by the parallel current which is limited by the sheaths (sheath limited regime), see the discussion on boundary conditions in section 2.6. In many theoretical works cited above, the scaling of the maximum velocity of the blob, which depends on the width of it was derived. Here we are following [89], where the authors also take the amplitude of the blob into account, in addition to the width for the derivation of the scaling laws. They used an isothermal model in 2D for the calculations but mention that it can be extended for capturing non-thermal effects. In the following the main points of [89] are sketched and extended in order to include the electron temperature. Here we focus on symmetrical blobs with the radial width δ_{\perp} . The divergence of the diamagnetic current is found to be approximately (see Eq. (3) in [89])

$$\nabla \cdot \mathbf{j}_{De} \sim -\frac{\kappa}{\delta_{\perp}}(n - n_B), \quad (3.1.3)$$

where κ is a constant denoting the strength of the curvature, n_B is the background density and n the density of the blob. The electron temperature is included in a straight forward way giving

$$\nabla \cdot \mathbf{j}_{De} \sim -\frac{\kappa}{\delta_{\perp}}(p_e - p_{eB}), \quad (3.1.4)$$

where $p_{eB} = n_B T_{eB}$ is the pressure of the background plasma and $p_e = n T_e$ is the total pressure of the blob with the absolute amplitude of the density and electron temperature n and T_e . The velocity of the blob is defined as the velocity of the center of mass

$$\mathbf{v}_f = \int dx dy (n - n_B) \mathbf{v}. \quad (3.1.5)$$

In the blob frame the background plasma has a negative momentum related to the blob. By going into the background frame where the blob has a positive momentum one can understand why the velocity of the blob saturates. In principle the blob is accelerated due to the $E \times B$ -advection, and there is no force which decelerates the blob. However in experiments and also in simulations which will be shown in the following the blob reaches a maximum velocity and starts decelerating. The gain in the momentum of the blob must be balanced. This is provided by the background plasma which the blob absorbs when traveling due to the $E \times B$ -advection. The maximum velocity is reached when the force from the polarization current $\mathbf{j}_p \times B$ is compensated by the mass gain of the filament. As pointed out in [89] in Eq. (9) the momentum gain of the blob due to absorption of the background plasma can be estimated roughly

$$\frac{\partial P}{\partial t} \sim -L_{\parallel} \delta_{\perp} n_B \mathbf{v}_f^2 \quad (3.1.6)$$

Extending the total force F ([89], Eq. (10)) on the blob to include the electron temperature yields

$$F \approx \kappa L_{\parallel} A_p p_{eB} \delta_{\perp}^2, \quad (3.1.7)$$

where the relative amplitude of the pressure is given by $A_p = \frac{\Delta p_e}{p_{eB}}$ with $\Delta p_e = p_e - p_{eB}$.

Balancing Eq. (3.1.6) and Eq. (3.1.7) gives the maximum velocity scaling of the blob in the inertial regime

$$\mathbf{v}_f^I \sim \sqrt{\frac{A_p}{n_B} \delta_{\perp}}. \quad (3.1.8)$$

This result shows clearly the physical behavior of the blob in the inertial regime. The interchange drive is pressure dependent. It is expected that with a higher pressure the polarization of the blob is stronger leading to a higher velocity of the blob. With an increasing background plasma n_B which is flowing into the blob the maximum velocity is decreased.

In order to get a scaling of the velocity in the sheath limited regime (section 1.2.3 in [89]) the sheath boundary condition is linearized

$$j_{\parallel}|_{sheath} = \pm n_S c_s (1 - e^{\Lambda - \phi_S/T_{eS}}) \approx \pm n_S c_s (\Lambda - \phi_S/T_{eS}). \quad (3.1.9)$$

Integrating over the the parallel direction yields

$$\int dz \nabla \cdot j_{\parallel} \approx 2n_S c_s (\Lambda - \phi_S/T_{eS}), \quad (3.1.10)$$

where the subscript S denotes the value of the quantity at the sheath. Assuming that the blob velocity is equal to the $E \times B$ -velocity one estimates $\mathbf{v}_f \sim \phi/\delta_{\perp}$. With this assumption one can balance the sheath current Eq. (3.1.10) and the diamagnetic drive Eq. (3.1.4) giving

$$2n_S c_s \Lambda T_{eS} - \frac{2n_S c_s \mathbf{v}_f \delta_{\perp}}{T_{eS}} = -\frac{\kappa}{\delta_{\perp}} (p_e - p_{eB}), \quad (3.1.11)$$

which yields a rough approximation for the scaling of the maximum velocity of the blob in the sheath limited regime

$$\mathbf{v}_f \sim \frac{T_{eS}^{3/2}}{\delta_{\perp}^2} \frac{p_e - p_{eB}}{p_{eS}} + \frac{\Lambda T_{eS}}{\delta_{\perp}}, \quad (3.1.12)$$

where one can assume that $\frac{T_{eS}^{3/2}}{\delta_{\perp}^2} \frac{p_e - p_{eB}}{p_{eS}} \gg \frac{\Lambda T_{eS}}{\delta_{\perp}}$ giving the final form of the sheath limited scaling

$$\mathbf{v}_f^S \sim \frac{T_{eS}^{3/2}}{\delta_{\perp}^2} \frac{p_e - p_{eB}}{p_{eS}}. \quad (3.1.13)$$

The fundamental blob size when $\mathbf{v}_f^S \approx \mathbf{v}_f^I$ is given by

$$\delta_* \sim \left(\frac{T_{eS}^{3/2} (p_e - p_{eB})}{p_{eS} \sqrt{A_p/n_B}} \right)^{2/5}. \quad (3.1.14)$$

In the following the scaling laws are going to be checked by simulating the model Eq. (2.4.1),(2.4.2),(2.4.5),(2.4.9),(2.4.10) without diffusion and the nonlinear heat conduction ($\kappa_{\parallel e0} = 0$) in the electrostatic limit $\beta_0 = 0$, $\mu = 0$.

Here a Gaussian blob structure for the density $n(x, y, z, t)$ and the electron temperature $T_e(x, y, z, t)$ is chosen

$$n(x, y, z, 0) = n_B + \Delta n \exp\left(-\frac{(x-x_0)^2 + (y-y_0)^2}{2\sigma^2}\right) \cdot \exp\left(-\frac{(z-z_0)^2}{2\mu_{\parallel}^2}\right), \quad (3.1.15)$$

$$T_e(x, y, z, 0) = T_{eB} + \Delta T_e \exp\left(-\frac{(x-x_0)^2 + (y-y_0)^2}{2\sigma^2}\right) \cdot \exp\left(-\frac{(z-z_0)^2}{2\mu_{\parallel}^2}\right), \quad (3.1.16)$$

where $\Delta n, \Delta T_e$ denotes the amplitude of the blob on the background. In the following a helium plasma is considered with $\Lambda = 3, R = 1.65m, T_{e0} = 7eV, n_0 = 1.0 \cdot 10^{19}m^{-3} B_0 = 1.5T, L_{\parallel} = 5R_0$ which results in the critical blob width $\delta_* \sim 10$ in terms of $\rho_s = 2.5 \cdot 10^{-4}m$. Before going into the details of the scaling laws the blob dynamics is discussed qualitatively.

3.1.1 Qualitative blob dynamics

For this purpose three blobs with $\delta_{\perp} = 2.0, 10.0, 80.0$ corresponding to the inertial, intermediate and the sheath limited regime respectively with $n_B = 1, \Delta n = 1$ and $T_{eB} = 1, \Delta T_e = 1$ are considered. The potential, the vorticity and the parallel current are initialized to zero. In figure 3.1.2 the dynamics of the density and the potential is shown in the inertial regime. The blob develops the classical 'mushroom-like' form. In order to gather a detailed view of the internal blob dynamics the velocity field $\vec{v} = (\nabla_x \phi, \nabla_y \phi)$ and the absolute value $|\vec{v}| = \sqrt{v_x^2 + v_y^2}$ are also plotted. The reason for these dynamics is the behavior of the potential which shows a dipolar structure leading to a high velocity of the plasma in the middle of the blob with two points where the velocity is almost zero. The mushroom form was observed very often in previous works [91–95].

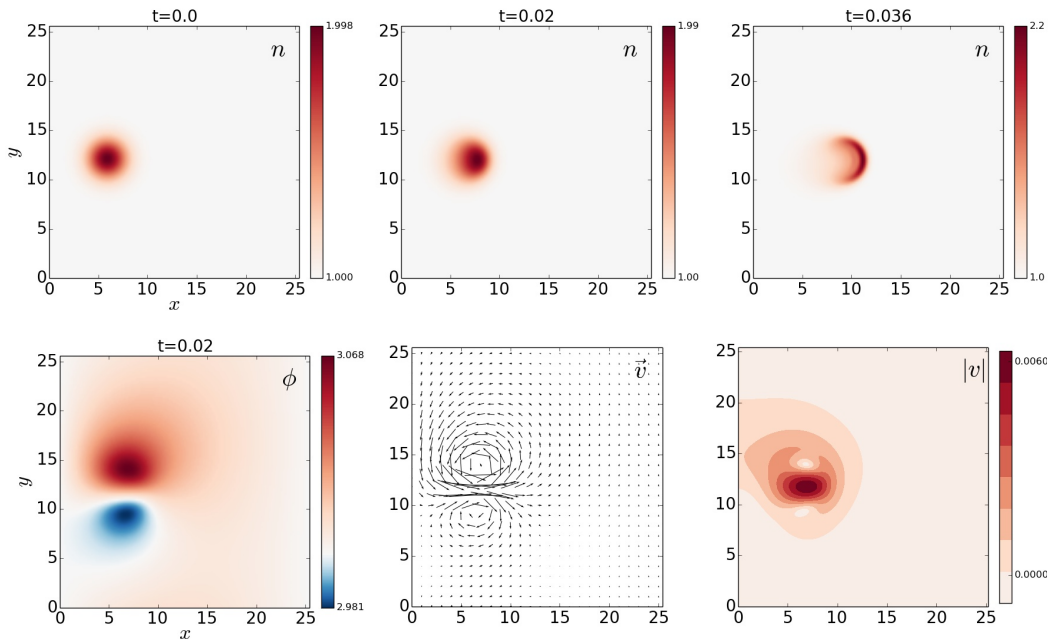


Figure 3.1.2: Blob dynamics in the inertial regime with $\delta_{\perp} = 2$. Dipolar structure of the potential causes the mushroom like form in the density.

In the intermediate regime, see figure 3.1.3 the blob shows a different behavior. The potential shows a dominant monopolar structure. It reveals a heavy non-symmetrical velocity field leading to a poloidal motion of the blob. The monopolar structure of the potential has two sources. First, every disturbance in density leads to a Boltzmann response of the potential, such that the potential follows the shape of the density which in this case is a Gaussian. Second, in the intermediate regime all currents are equivalent. The sheath physics forces the potential to approach $\phi \sim \Lambda T_e$. This effect is not fully developed in the intermediate regime, nevertheless the potential starts to follow the structure of the electron temperature leading to a monopolar structure.

Consequently in the sheath limited regime, see figure 3.1.4 the potential approaches $\phi \approx \Lambda T_e$ leading to a strong rotational component in the velocity field. However the dipolar structure is still present, although not visible, leading to a radial motion of the blob.

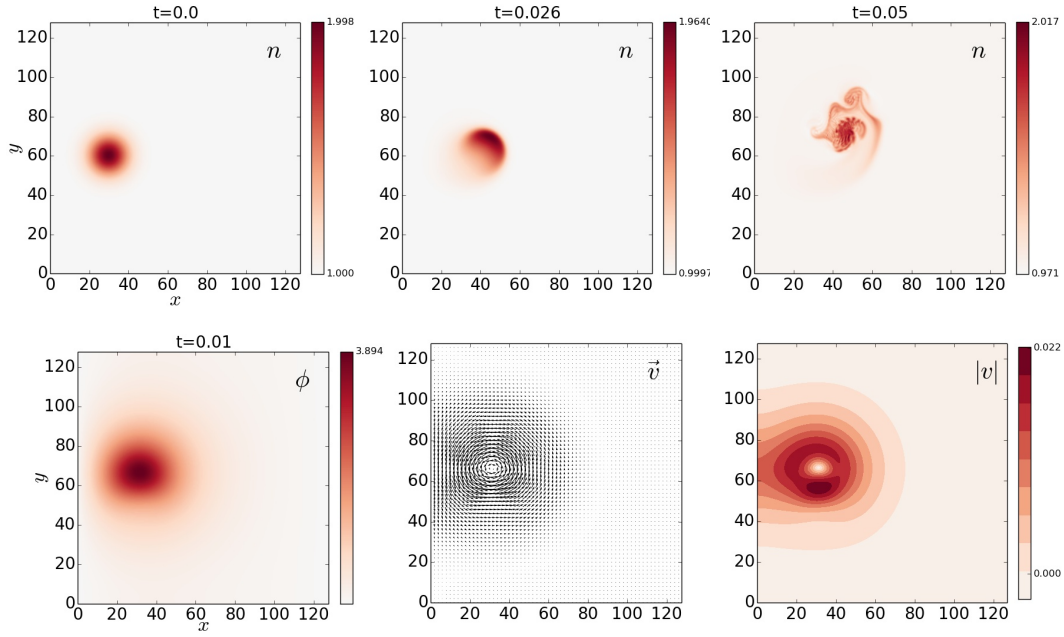


Figure 3.1.3: Blob dynamics in the intermediate regime with $\delta_{\perp} = 10$. The dipolar structure of the potential is overlapped by a monopolar component leading to a poloidal flow.

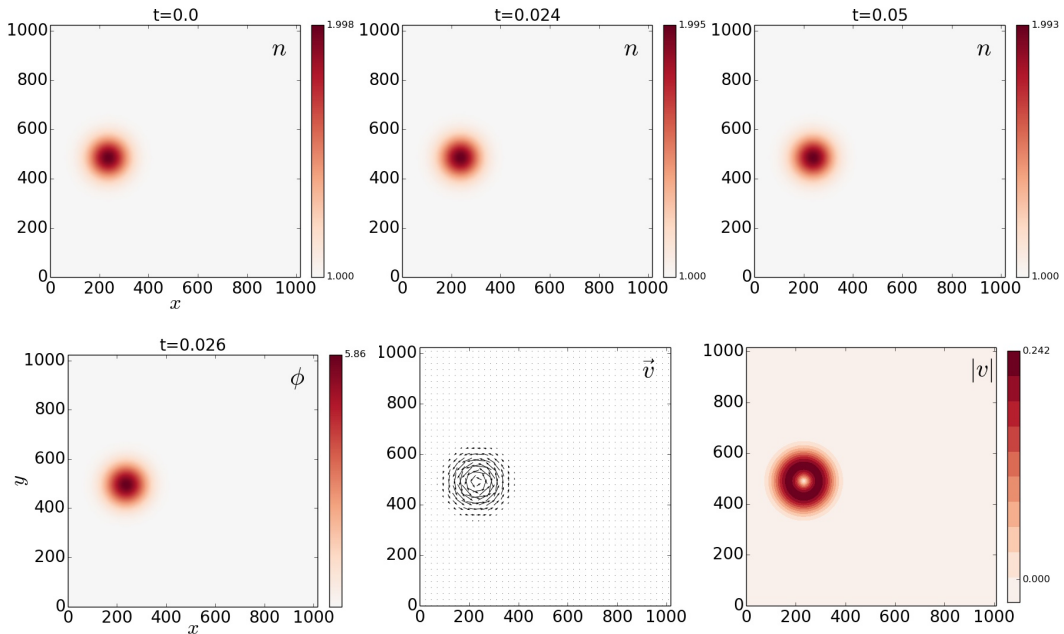


Figure 3.1.4: Blob dynamics in the sheath limited regime with $\delta_{\perp} = 80$. The dipolar structure of the potential is not visible anymore. It is overlapped by a monopolar component $\phi \approx \Lambda T_e$ leading to a rotational motion.

3.1.2 *Scaling with the width*

In this section the scaling laws for the radial width of the blob in the inertial regime Eq. (3.1.8),

$$\mathbf{v}_f \sim \sqrt{\delta_\perp} \quad (3.1.17)$$

and in the sheath limited regime Eq. (3.1.13),

$$\mathbf{v}_f \sim \frac{1}{\delta_\perp^2} \quad (3.1.18)$$

are checked. For this purpose the radial widths $\delta_\perp = 0.1, 0.025, 0.4, 1.0, 2.0, 4.0, 6.0, 8.0, 10.0, 20.0, 40.0, 80.0$ are scanned. The radial resolution is always chosen in the way such that the blob is resolved in every case with 10 grid points $h = \delta_\perp/10$. The toroidal resolution is again $\Delta z = 2\pi/32$. The initial state and the boundary conditions are chosen in the same way like it was done in the previous section. For each case the behavior of the velocity is analyzed, see figure 3.1.5.

For the blob widths which are smaller than the critical blob size, $\delta_\perp < \delta_* \approx 10\rho_s$ for the chosen parameters, the velocity increases with the width. The blob shows a linear acceleration phase until it reaches the maximum velocity and starts decelerating. The situation is different in the sheath limited regime with $\delta_\perp = 20.0, 40.0, 80.0$. In this regime the velocity shows a kind of plateau behavior. It reaches the maximum velocity at much later time points compared to the inertial regime and starts decelerating slowly. Also the maximum velocity is lower compared to the inertial regime which is consistent with the theory of blob dynamics.

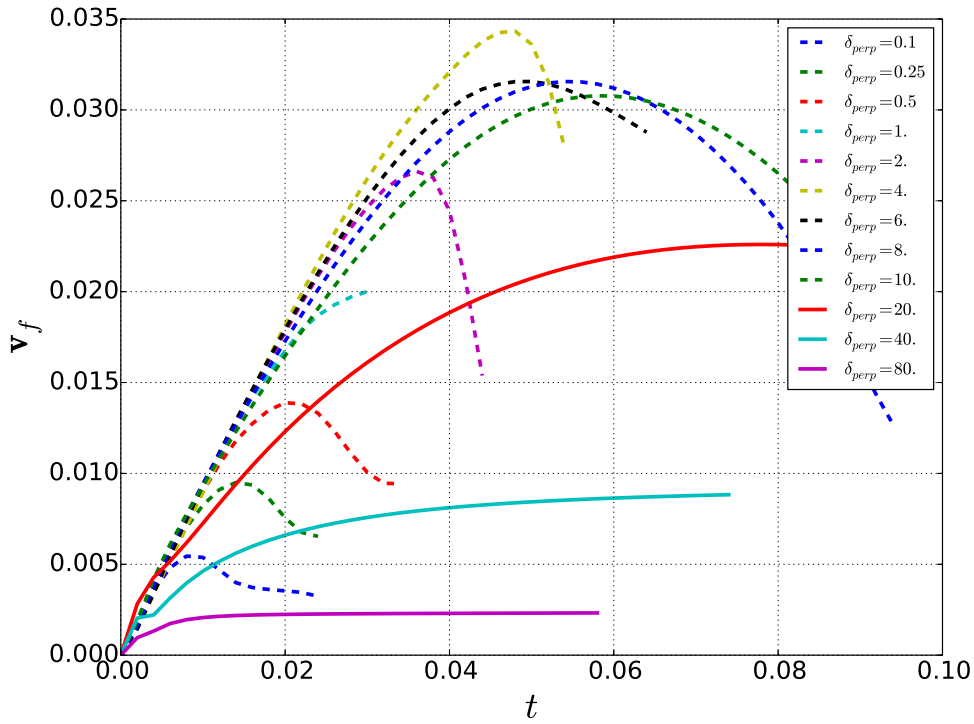


Figure 3.1.5: Velocity dependence of the blobs center of mass on the radial width $\delta_{\perp} = 0.1, 0.025, 0.4, 1.0, 2.0, 4.0, 6.0, 8.0, 10.0, 20.0, 40.0, 80.0$. After Reaching the critical blob size $\delta_{\perp} = \delta_* = 10\rho_s$ the maximum velocity decreases. Dashed: inertial regime. Solid: sheath limited regime.

The logarithm of the maximum values of the velocities \mathbf{v}_f are plotted against the logarithm of the radial width of the blob in figure 3.1.6. Two reference lines are plotted for $\sqrt{\delta_{\perp}}$ and $1/\delta_{\perp}^2$. Under the critical blob size the expected inertial behavior is obtained. The maximum velocity increases with the radial width $\mathbf{v}_f \sim \sqrt{\delta_{\perp}}$. The transition to the sheath limited regime appears at the critical blob size $\delta_{\perp} \approx \delta_* \approx 10\rho_s$. In the sheath limited regime the velocity decreases with $\mathbf{v}_f \sim 1/\delta_{\perp}^2$. This behavior was also reproduced in an isothermal model [93] using the Boussinesq approximation with GRILLIX.

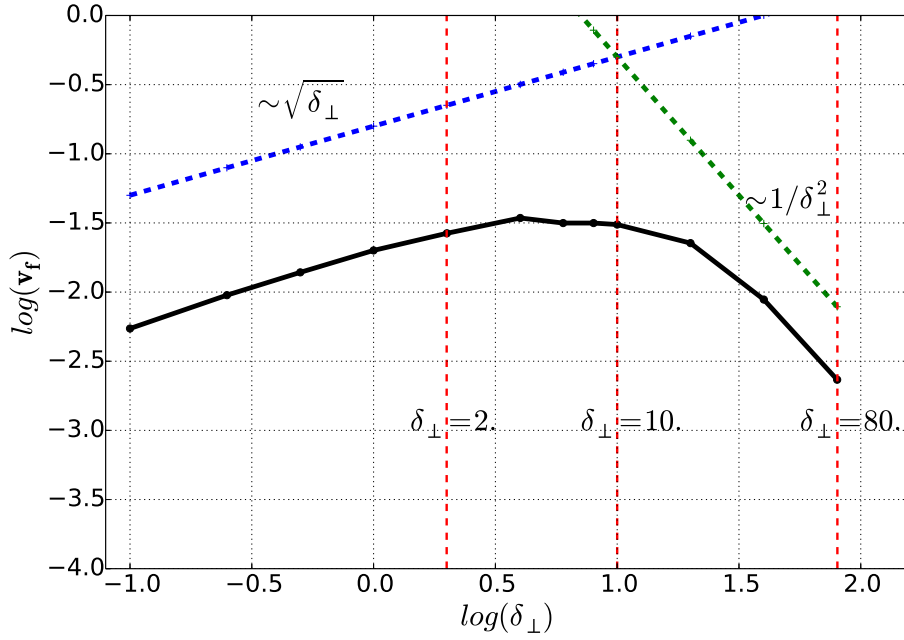


Figure 3.1.6: Complete velocity scaling from the inertial regime over the intermediate regime to the sheath limited regime.

The full transition from the inertial regime to the sheath limited regime is successfully recovered within GRILLIX simulations. Next, the dependence on the amplitude is going to be investigated.

3.1.3 Scaling with the amplitude

In this section the scaling laws for the amplitude of the blob in the inertial regime Eq. (3.1.8),

$$\mathbf{v}_f \sim \sqrt{\Delta n \Delta T_e + n_B \Delta T_e + T_B \Delta n} \quad (3.1.19)$$

and in the sheath limited regime Eq. (3.1.13),

$$\mathbf{v}_f \sim T_{eS}^{3/2} \frac{p_e - p_{eB}}{p_{eS}} \quad (3.1.20)$$

are checked. For this purpose the radial widths $\delta_\perp = 2.0, 10.0, 80.0$ are chosen in order to cover the inertial, the intermediate and the sheath limited regime. For every width a constant background density $n_B = 1$ and electron temperature $T_{eB} = 1$ are chosen.

On top of the background the dynamics of blobs with different amplitudes in the density and the electron temperature is considered. In the following, in each regime the density amplitude of the blob will be increased from $\Delta n = 1$ to $\Delta n = 9$ while the amplitude of the electron temperature is chosen $\Delta T_e = 1$ as the initial condition. Next the electron temperature will be increased from $\Delta T_e = 1$ to $\Delta T_e = 9$ while the density amplitude is chosen with $\Delta n = 1$. Finally both quantities are going to be increased at the same time from $\Delta n, \Delta T_e = 1$ to $\Delta n, \Delta T_e = 9$. In each case the maximum velocity \mathbf{v}_f is derived and plotted against the amplitude.

In the inertial regime a square root dependence on the amplitude in $\Delta n, \Delta T_e$ of the maximum velocity is expected. The expected scaling is obtained for Δn as shown in figure 3.1.7 by the reference line $\sqrt{\Delta n}$ for the full system without the Boussinesq approximation (FS). If only the amplitude of the temperature is increased then the situation is more complex. The blob gets very unstable such that the derivation of the center of mass is very difficult. This is why just the maximum amplitude $\Delta T_e = 5$ could be covered. When $\Delta n, \Delta T_e$ are increased at the same time one expects a nearly linear scaling, which is not recovered. The reason for this is the shift of the inertial regime towards the sheath limited regime with higher temperatures. The parallel conductivity is temperature dependent $\sigma_{\parallel} \sim T_e^{3/2}$ which makes the sheath closure more favorable with an increasing temperature, although the blob width $\delta_{\perp} = 2$ suggests an inertial behavior. The increasing temperature causes the blob to change to the regime where neither the inertial scaling nor the sheath limited scaling hold.

In the sheath limited regime it is necessary to know the sheath values of the quantities in order to obtain the scaling. However it is not clear which value need to be taken, e.g. the center of mass of the blob or some intermediate value. It is found from simulations that the sheath value at maximum velocity depends linearly on the initial amplitude $f_S = q + c \cdot A_f$. The values q and c act as fitting parameters. The model

$$\mathbf{v}_f \sim (q + c \cdot A_t)^{3/2} \frac{A_p}{(q + c \cdot A_p)}$$

is found to describe the simulation data very well in the sheath limited regime. The reference line in the $\Delta n, \Delta T_e$ -plot is the fitted model with $q = 1.8, c = 1.15$.

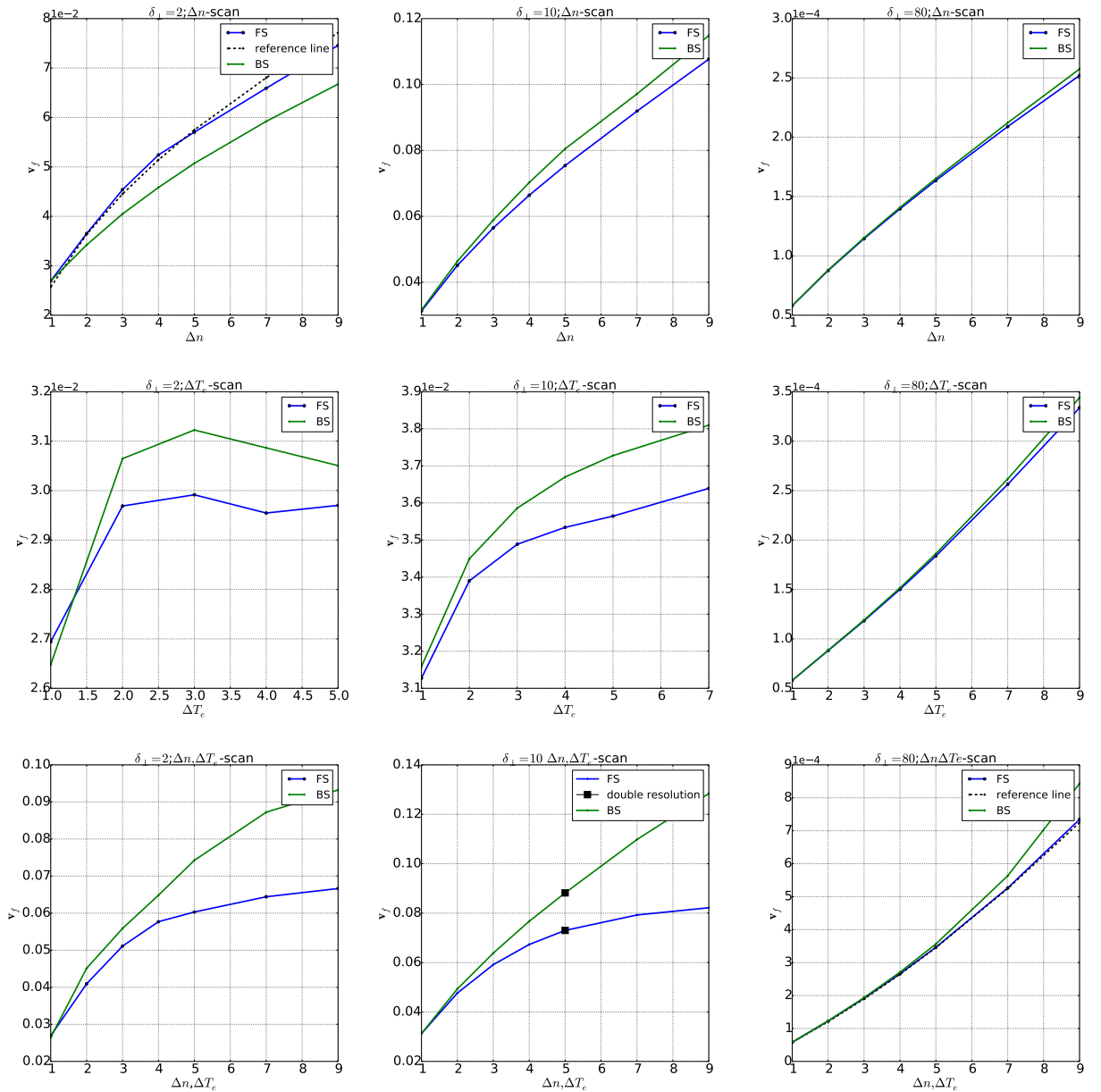


Figure 3.1.7: Maximum velocity scan over $\Delta n, \Delta T_e$ for the full system (FS) and the Boussinesq system (BS). The predicted scalings (reference lines) for the inertial and the sheath limited regimes are in excellent agreement with simulation. Double resolution simulation yields the same result.

This result shows clearly that in addition to the width scaling the GRILLIX simulations recover excellently the predicted scalings with the amplitudes which were derived in section 3.1. In the next section the impact of the Boussinesq approximation is going to be discussed.

3.1.4 *Impact of the Boussinesq approximation*

The Boussinesq approximation has a long history in simulations of blob dynamics. Most of the works cited in this chapter were done using the Boussinesq approximation. Only a few papers investigated the impact of the Boussinesq approximation in an isothermal 2D model [89, 107–109]. It was shown that in the Boussinesq approximation the blob decays faster. Furthermore, it was not possible to get the correct velocity scaling in the inertial regime in the Boussinesq approximation. A subtle point considering the use of the Boussinesq approximation is that it was often employed in the non-conservative form given in section 2.7.1, see for example the recent paper [64]. In that paper, although a thermal model is used, the velocity scaling in the inertial regime becomes independent of the pressure. Although the results in the non-conservative form of the Boussinesq approximation may give the desired outcome, its use is at least questionable since the relation $\nabla \cdot \mathbf{j} = 0$ does not hold anymore. However, this relation is the foundation for the whole theory of blob dynamics from the inertial to the sheath limited regimes. If current is not a conserved quantity a discussion about current balancing is not consistent without providing the magnitude of error for $\nabla \cdot \mathbf{j} = 0 + O(\epsilon)$. Here the conservative form of the Boussinesq approximation (BS) is compared to the full system (FS). The Boussinesq approximation enters the inertial part. Current balancing suggests that the impact of the Boussinesq approximation should depend not only on the amplitude of n , but also on the regime of the dynamics. In the sheath limited regime where the inertial term is negligible the impact of the Boussinesq approximation is expected to be weak.

Figure 3.1.8 shows a qualitative difference between FS and BS. The plot shows a blob with $\delta_{\perp} = 10$ and $\Delta n, \Delta T_e = 5$ at three time points. Although the time points are equal, the blob shows a different behavior. In the BS the blob accelerates faster. It loses the coherent form and decays into turbulence while the blob in FS still has a coherent form. This run has been performed with the double resolution in order to exclude a numerical reason for the difference, which produced the same result. A more detailed and systematic comparison between these two systems is presented in figure 3.1.7, where the amplitude scans from the previous section are compared in FS and BS. The maximum velocity with the double resolution is plotted in the intermediate $\Delta n, \Delta T_e$ -plot.

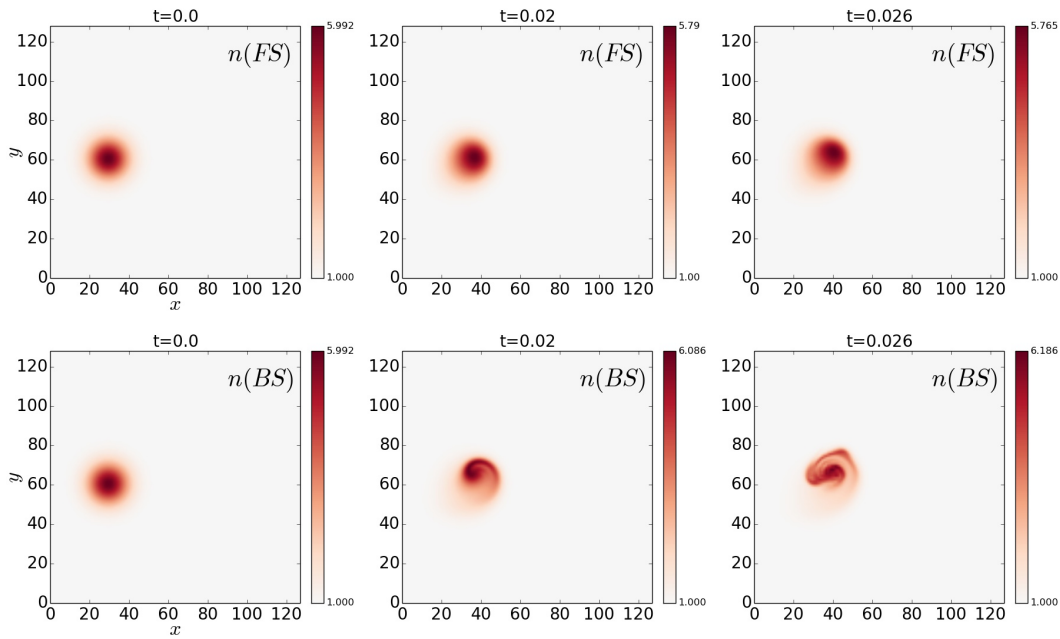


Figure 3.1.8: Comparison between the density in full system (FS) and in the Boussinesq system (BS) for a blob with $\delta_{\perp} = 10.$ and $\Delta n, \Delta T_e = 5.$

The BS is in qualitative agreement with FS. Going from the inertial regime into the sheath limited regime the difference between FS and BS decreases. In the sheath limited regime the difference is negligible. The difference starts to become visible only for very high values of $\Delta n, \Delta T_e.$ The situation is different in the inertial regime. Here the dynamics is dominated by the terms where the Boussinesq approximation enters. If only Δn is varied, the difference gets bigger for higher amplitudes but stays nevertheless moderate. In the situation where only ΔT_e is varied the situation is again difficult in terms of measurement of the center of mass. Also in the Boussinesq approximation the blob is very unstable. However a difference in maximum velocity between BS and FS is recognized even when only ΔT_e is varied. This holds also in the intermediate regime where the blobs are stable and a clear measurement of the center of mass is possible. This is a surprising finding since the Boussinesq approximation enters the system only via the density. The temperature amplifies the difference between FS and BS. As discussed before, for higher electron temperature the blob changes from the inertial regime into the sheath limited regime where the potential starts to follow $\Delta T_e.$ Via this effect the temperature enters the inertial term and amplifies the difference between FS and BS. The difference is even more pronounced when Δn and ΔT_e are increased at the same time. Thus the impact of the Boussinesq approximation does not only depend on the density due to the

relation of the potential to the electron temperature the regime of the filament is important when discussing the impact of the Boussinesq approximation. In previous works this fact was not taken into account.

In the intermediate regime the difference between BS and FS is observable especially for hot and dense blobs. The use of the Boussinesq approximation in these regimes may become questionable depending on the parameters.

Summary

In this chapter the dynamics of blobs was investigated. It is an important test for the model and the numerical implementation of it. It was shown that the model captures the expected physics of blobs. GRILLIX is able to simulate the complete transition from the inertial to the sheath limited regime. One can conclude from this that the temperature dependent sheath boundary conditions were implemented correctly. Furthermore on the analytical side the scalings for the maximum velocity capturing the radial width, thermal effects and the amplitude of the blob were derived and tested. It was found that the expected scalings were in excellent agreement with the simulations. Thermal effects introduce an additional layer of complexity which can drive the blob from the inertial into the sheath limited regime by affecting the sheath part of the equation via the parallel conductivity. At the same time the temperature enters the inertial part via the potential affecting the inertial regime which is an explanation for the impact of the Boussinesq approximation. It was stated that the use of the non-conservative form of the Boussinesq approximation is not consistent with the theory of blob dynamics. The conservative form was in qualitative agreement with the full system. The difference between the full and the Boussinesq system was found to be significant in the inertial and intermediate regime for higher amplitudes of the density and the electron temperature.

3.2 TURBULENCE ON CLOSED FIELD LINES

In this section several fundamental tests in GRILLIX are performed. In all cases a periodic slab geometry is used. The simplicity of the geometry allows a focus on key features of GRILLIX. First, the electromagnetic dynamics, which is treated via the Helmholtz solver (section 2.8.6), is going to be tested. The simulation of an Alfvén wave impulse is compared to theoretical predictions, testing whether the solver provides the correct solution. Second, the conservation of energy and particles within GRILLIX simulations of turbulence is checked. On the analytical level the model has perfect conservation properties, see section 2.5. These properties need to be conserved on the discrete level in a good way. Otherwise artificial sources or sinks may appear, affecting the turbulence dynamics. Results, which are produced in such an environment would not be reliable. In addition to MMS (section 2.8.7), which only tests the numerical implementation, the tests presented here are crucial showing the reliability of physical results produced with GRILLIX.

3.2.1 Alfvén dynamics

In this chapter the importance of electromagnetic effects on turbulence dynamics and simulations is investigated. As pointed out in [110] collisional drift-wave turbulence with $k_{\perp}\rho_s \sim 1$ can be taken to be electrostatic if the plasma beta (see chapter 2) satisfies $\beta \ll \mu$ for the parallel dynamics and $\hat{\beta} = \beta(qR/L_{\perp})^2 \ll 1$ for the drift dynamics with the connection length $2\pi qR$ which depends on the geometry. These assumptions leads to the electrostatic $E \times B$ -dynamics and the drift-wave instability. These conditions are satisfied in the far scrape-off layer. Outside of the far scrape-off layer they are violated already at rather low densities and temperatures near the separatrix where $\beta \geq \mu$ and $\hat{\beta} \geq 1$, resulting in turbulence and transport which is strongly affected by electromagnetic effects. However it is important to point out that although the electron dynamics, which are determined by Ohm's law, may be dominated by magnetic induction and electron inertia, the transport can be still electrostatic dominated by $E \times B$ -flows which are much stronger than the parallel transport down the perturbed magnetic field lines. As will be discussed in more detail below the most pronounced effect of magnetic induction in turbulence is to make the response of the electrons to parallel forces non-adiabatic, leading to electron driven turbulence. Under these conditions the drift-wave instability turns into nonlinear Drift-Alfvén instability [110, 111] (which is discussed below) leading to an increasing

turbulence with higher β . In order to understand the impact of magnetic induction and electron inertia, the generalized Ohm's law Eq. (2.4.6) is rewritten in terms of the parallel electron heat flux Eq. (2.1.14) giving [110]

$$\underbrace{\beta_0 \frac{\partial}{\partial t} A_{\parallel}}_{\text{magnetic induction}} + \underbrace{\mu \left[\frac{\partial j_{\parallel}}{\partial t n} + \frac{\delta}{B} \left\{ \phi, \frac{j_{\parallel}}{n} \right\} + v_{\parallel e} \nabla_{\parallel} \frac{j_{\parallel}}{n} \right]}_{\text{electron inertia}} + \underbrace{\frac{j_{\parallel}}{\sigma_{\parallel}} + \frac{0.71}{\kappa_{\parallel e}} (q_{\parallel e} + 0.71 T_e j_{\parallel})}_{\text{collisional dissipation}} = \underbrace{-\nabla_{\parallel} \phi + T_e \nabla_{\parallel} \theta_n}_{\text{parallel forces}} \quad (3.2.1)$$

Now it is more clear how the electron response to parallel forces should appear. Magnetic induction, electron inertia and collisional dissipation tend to balance the electron response to parallel forces. In the electrostatic case neglecting electron inertia $\beta = \mu = 0$ the parallel forces are balanced by collisional dissipation. In the electromagnetic case the electron inertia introduces the collisional skin depth, as the perpendicular scale above which the magnetic induction becomes dominant in the collisionless regime which is $\beta > (k_{\perp} \rho_s)^2 \mu$ [110, 112]. Magnetic induction controls then the response to parallel forces and ensures that a perturbation cannot propagate along the magnetic field faster than the Alfvén velocity $v_A = B_0 / \sqrt{4\pi n m_i}$ or for very small scales faster than the thermal velocity v_e .

In order to get a more quantitative view of the electromagnetic dynamics a model evolving disturbances on a homogeneous background under the drift approximation from [52] is used

$$\frac{\partial}{\partial t} \nabla_{\perp}^2 \tilde{\phi} = \nabla_{\parallel} \frac{\tilde{j}}{n}, \quad (3.2.2)$$

$$\frac{\partial \tilde{n}_e}{\partial t n_e} = \nabla_{\parallel} \frac{\tilde{j}}{n e c_s}, \quad (3.2.3)$$

$$\beta_0 \frac{\partial}{\partial t} \tilde{A}_{\parallel} + \mu \frac{\partial \tilde{j}}{\partial t n} = \nabla_{\parallel} (\tilde{n}_e - \tilde{\phi}). \quad (3.2.4)$$

Out of the system Eq. (3.2.2-3.2.4) a wave equation can be derived giving

$$\frac{\partial^2}{\partial t^2} (\tilde{n}_e - \tilde{\phi}) = V_a^2 \nabla_{\parallel} (\tilde{n}_e - \tilde{\phi}) \quad (3.2.5)$$

with the wave speed

$$V_a = \sqrt{\frac{1 + k_\perp^2}{\beta_0 + \mu k_\perp^2}} \quad (3.2.6)$$

It is evident that the speed of the wave along the magnetic field line depends on the scale of motion k_\perp in perpendicular direction. As pointed out in [52] the limit $k_\perp^2 \rightarrow 0$ yields propagation at the Alfvén speed

$$\lim_{k_\perp^2 \rightarrow 0} V_a = v_A \quad (3.2.7)$$

On the other side the limit $k_\perp^2 \rightarrow \infty$ yields propagation at the thermal velocity

$$\lim_{k_\perp^2 \rightarrow \infty} V_a = \sqrt{\frac{T_e}{m_e}} = v_e$$

These two limits indicate the fastest and slowest Alfvén wave propagation. Large perpendicular scales propagate with the Alfvén velocity v_A . Small scales propagate with the thermal velocity v_e . In the literature these Alfvén waves are often called ‘kinetic Alfvén waves’, due to the first derivation from the Vlasov Equation [113]. Compared to the basic shear Alfvén wave, which is a plain wave along the magnetic field lines, the kinetic Alfvén waves have a cross-field component posing a torsional Alfvén wave [52]. Drift waves, which have a perpendicular wavelength comparable to the ion gyro-radius couple to the kinetic Alfvén waves due to its dependence on k_\perp finally posing the Drift-Alfvén instability in turbulence [114].

What do these findings mean for GRILLIX or in general a turbulence code suitable for the scrape-off layer? The electrostatic assumption breaks down in the scrape-off layer, meaning that a plasma turbulence code designed for the simulation of the turbulence in the SOL needs to take into account the electromagnetic effects. If electrostatic dynamics are assumed, the only remaining balancing for parallel forces in Eq. (3.2.1) is the collisional dissipation which is a very fast process. Resolving such a fast process in the simulation is cumbersome due to a heavy limit on the time step on the one hand and on the other hand it is not relevant for the SOL due to the fact that even at very low $\beta_0 \sim 10^{-6}$ [110] the dynamics is electromagnetic. Indeed the experience gained within the global electrostatic model during this thesis confirmed the importance of electromagnetic dynamics. The limit on the time step was extremely pronounced in particular when the electron temperature was high, leading to a high σ_\parallel and $\kappa_{\parallel e}$. The slow, but still feasible simulations in the slab geometry finally motivated the inclusion of

the electromagnetic effects. The extension of GRILLIX to an electromagnetic model is crucial in a numerical and physical sense. It is of great importance to note, that the extension to an electromagnetic model finally accelerated the simulations by a factor of 60! The core of the electromagnetic model in GRILLIX is the Helmholtz-solver from section 2.8.6, whose implementation is going to be tested with the analytical predictions from the delta-f model (3.2.2-3.2.4). Finally the results are compared to the global model.

For this test a Gaussian function in the density is initialized in parallel direction. A periodic slab geometry is used here with an isothermal electromagnetic model without parallel ion momentum in order to match the delta-f model as closely as possible. In the perpendicular plane a sine mode is initialized which allows the variation of k_{\perp} . For the first test, the values $\beta_0 = 8 \cdot 10^{-3}$ and $\mu = 10^{-4}$ are chosen. The perpendicular scale is varied with $k_{\perp} \rho_s \in [\frac{2\pi}{628}, \frac{2\pi}{20}, \frac{2\pi}{15}, \frac{2\pi}{10}, \frac{2\pi}{5}, \frac{2\pi}{1.98}, \frac{2\pi}{1}, \frac{2\pi}{0.5}, \frac{2\pi}{0.25}, \frac{2\pi}{0.125}, \frac{2\pi}{0.00625}, \frac{2\pi}{0.003125}]$. The center of mass velocity of the impulse $\tilde{n} - \tilde{\phi}$ is tracked. An example is shown in figure 3.2.1 for $k_{\perp} = \frac{2\pi}{628}$.

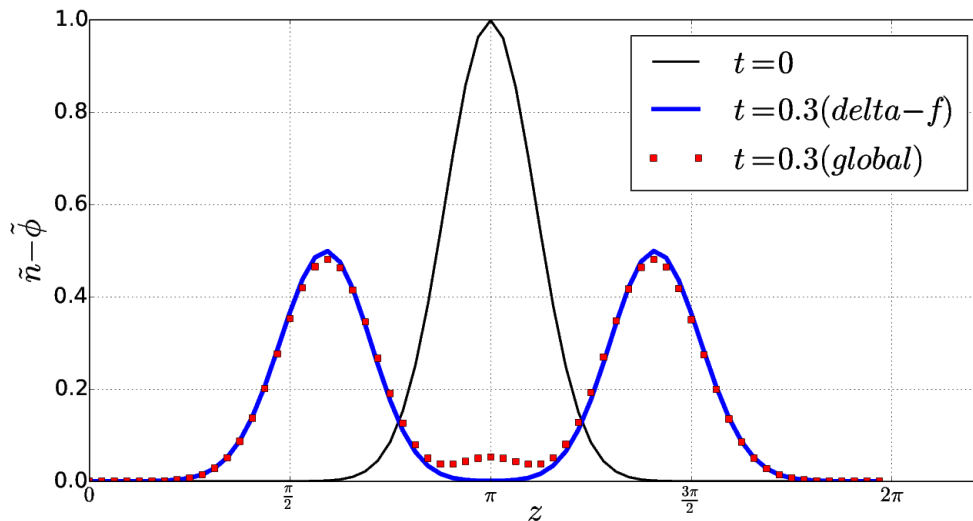


Figure 3.2.1: Initial Gaussian perturbation in the density at $t = 0$. An impulse in $\tilde{n} - \tilde{\phi}$ propagates along the magnetic field lines. Both models coincide with each other.

For the delta-f simulation a disturbance with the amplitude $n(t = 0) = 1$ was initialized. In the global model a constant background density n_0 with a perturbation $n(t = 0) = 0.1n_0$ was used. In order to show both simulations on the same plot the background density was subtracted from the global solution and the amplitude was scaled with a factor of ten. From the initial

density perturbation an impulse in $\tilde{n} - \tilde{\phi}$ starts in both directions. It is evident that the delta-f solution coincides with the global model. The k_{\perp} -scan is shown in figure 3.2.2 for both models. First of all the delta-f solution matches the analytical prediction. Very large perpendicular structures propagate with Alfvén velocity. There is a smooth transition to thermal electron velocity for smaller scales. The global model matches the analytical prediction and the delta-f model for all tested scales! This result holds for small initial perturbation in the density. The models diverge significantly for higher amplitudes. This result shows clearly that the delta-f model is a limit of the global model for low amplitudes compared to the background. The linear dynamics is still present in the global model.

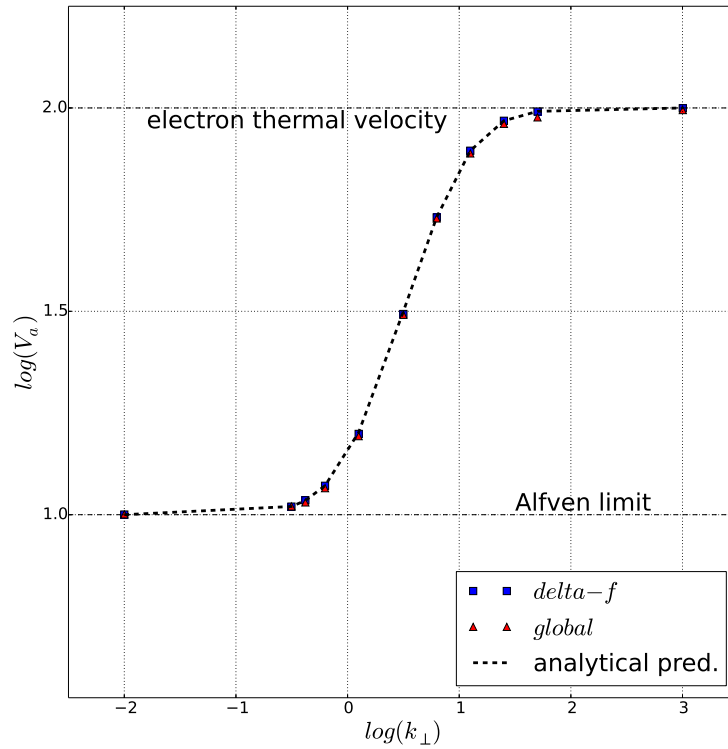


Figure 3.2.2: k_{\perp} -scan for the delta-f model and the global model. Analytical prediction coincides with both models. Smooth transition from Alfvén limit to electron thermal velocity.

Another test is the scan of β_0 . For this the perpendicular scale is fixed with $k_{\perp} = \frac{2\pi}{12800}$. A scan in $\beta_0 \in [9, 8, 7, 6, 5, 4, 3, 2, 1, 0.9, 0.8, 0.7, 0.6, 0.5, 0.4, 0.3, 0.2, 0.1] \cdot 10^{-3}$. In this limit it is expected that the structure propagates at the Alfvén

speed. The result is shown in figure 3.2.3. Again the the analytical prediction is matched perfectly by the delta-f model. The global model is also in very good agreement. These tests show clearly that the core of electromagnetic model in GRILLIX, the Helmholtz-solver is performing well. Although the implementation of it was already tested within the method of manufactured solutions a physical test remains crucial. The electromagnetic effects are simulated in GRILLIX correctly from a numerical and physical perspective.

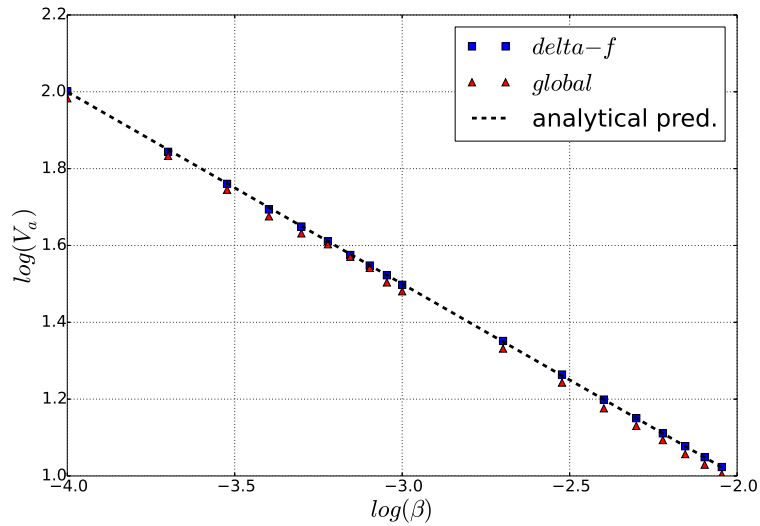


Figure 3.2.3: β_0 -scan for the delta-f model and the global model. Analytical prediction coincides with both models. Alfvén velocity is obtained for $k_{\perp} = \frac{2\pi}{12800}$.

Summary

In this chapter several fundamental tests were performed in order to check whether GRILLIX simulations yield the expected electromagnetic dynamics. It was shown that the dynamics in the scrape-off layer is dominated by electromagnetic effects. The turbulence is electromagnetic, the transport remains mainly electrostatic. Magnetic induction and electron inertia replace the collisional dissipation in Ohm's law for the electron answer slowing down the dynamics to Alfvén speed or thermal speed. This is favorable from a numerical point of view as the limitation on the time step from the fast collisional dissipation process is relaxed. In addition to that, the results become physically relevant for the SOL. The Alfvén dynamics was tested within a relative simple delta-f model where an analytical dispersion relation can be derived. It showed that the Helmholtz solver which is the core for the treatment of electromagnetic effects in GRILLIX works very well. The dynamics of an impulse changed from thermal velocity to pure Alfvén velocity in dependence of k_{\perp} as predicted by theory. The global model was compared to the delta-f model for small amplitudes of the density and it was found that the models are in overall agreement. From this one concludes that the electromagnetic effects are captured by GRILLIX in a correct way.

3.2.2 *Conservation properties*

Conservation properties play a crucial role for the model and the numerical implementation of it in GRILLIX. As was shown in section 2.5 the global drift reduced Braginskii system perfectly conserves energy. Towards a global turbulence code with predictive and trustable capabilities this property need also to be fulfilled accurately on the discrete level in the code. The final outcome of a simulation would become at least questionable if a fundamental feature like energy conservation is not fulfilled. In addition to the energy conservation the code needs to fulfill particle conservation. The numerics should neither create nor destroy energy and particles. The method of manufactured solution from section 2.8.7 is not able to discover non-conservative properties of the numerical scheme as it just shows if the scheme was implemented correctly. In this light the check of the conservation properties is a physical verification test. In this chapter the conservation properties of the global electromagnetic system will be investigated. For this purpose a turbulence simulation in a periodic slab geometry is performed. The periodic slab geometry is chosen due to its simplicity as the focus here is on the check of the conservation properties. Plasma is brought into the system via sources. Without any sinks e.g. target plates, the density and electron temperature should remain in the computational domain. The corresponding energies are transformed according to the energy theorem. Each part in Eq. (2.5.1)-(2.5.4) is derived in GRILLIX. It is checked if the equations hold. In section 2.7.1 the impact of the Boussinesq approximation on the energy theorem was shown and it was stated that very often the Boussinesq approximation is used in a non-conservative form, breaking the conservation properties of the system. Here the impact of the Boussinesq approximation on turbulence on closed field lines is shown. Earlier results in a electrostatic model were published in [75]. The results presented here take the efforts in reaching a global conservative model one step further by the inclusion of electromagnetic effects.

Modeling

For the modeling of the turbulence and the check of conservation properties a periodic slab geometry is used. The global electromagnetic model (2.7.1-2.7.5) is employed. The density and electron temperature are ramped up to a target value with Gaussian sources S_f respectively

$$S_f = C_f \exp(-(x - x_s)^2 / 2w_s) (f_{target} - \langle f \rangle_{zonal}). \quad (3.2.8)$$

The sources are localized on the left side of the computational domain simulating the core plasma. In the rest of the domain (source free region) the plasma develops freely. A Dirichlet boundary condition is chosen on the wall side for the density and electron temperature, acting as a sink. A grid with $n_x = n_y = 128$ and $n_z = 32$ was used for the simulations in this chapter. The plasma is subject to several instabilities. The main drive of the turbulence are the drift-Alfvén instabilities, ballooning and the interchange instability leading to a turbulent state. Similar parameters like in [75] were used in this chapter with the parallel conductivity $\sigma_{\parallel 0} = 1.5$, the perpendicular diffusion $\nu_{n, T_e, \phi, \mu_{\parallel}} = 2.5$, the parallel diffusion $\mu_{n, T_e, \phi, \mu_{\parallel}} = 10^{-2}$, $\delta = 580$, the perpendicular resolution $h = 0.5$ and the toroidal resolution $\Delta z = 2\pi/32$. A typical example of a turbulence simulation is shown in figure 3.2.4 for the density and the potential at the mid-plane. Blob like structures are born in the source region, which are advected by the $E \times B$ -drift into the direction of the wall developing a kind of mushroom like form which is typical for blobs in the inertial regime, as was discussed in section 3.1.1 about qualitative blob dynamics.

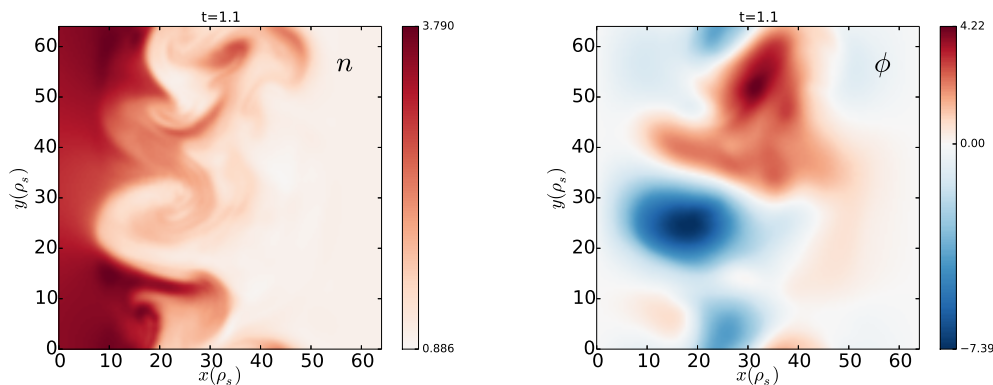


Figure 3.2.4: Turbulence on closed field lines at the mid-plane creates blob like structures which are advected by the $E \times B$ -drift.

Particle conservation

The only sink in the system is the Dirichlet boundary subtracting plasma reaching the wall. The turbulence reaches a turbulent equilibrium regime when the sources and sinks are in balance. As shown in figure 3.2.5 the density and electron temperature are saturated, fluctuating around a mean value.

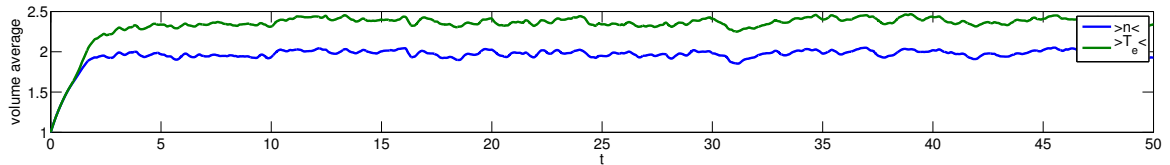


Figure 3.2.5: Volume average of the density and electron temperature indicates a balance between the sources and sinks. The turbulence is saturated.

The balance between the sources and sinks is shown in figure 3.2.6, indicating a very good particle conservation in GRILLIX. The change in density is according to a balance of the source and sink which is the diffusion on density D_n , see section 2.5.

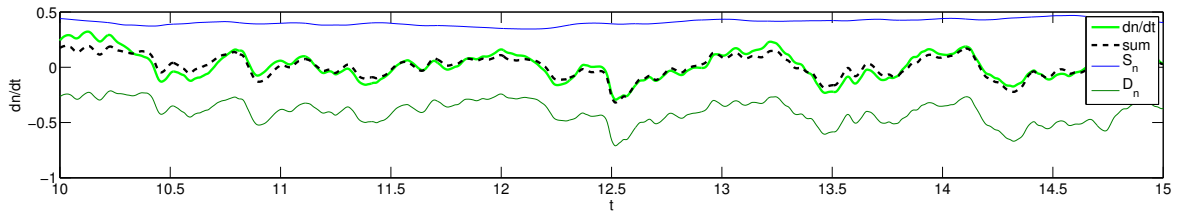


Figure 3.2.6: Particle conservation in a saturated turbulent regime. The change in density is according to a balance between the sources and sink.

Energy conservation

In the same fashion like the particle conservation the energy conservation properties are checked. For this the perpendicular kinetic energy E_{\perp} , the parallel kinetic energy E_{\parallel} , the thermal energy E_{the} and the electromagnetic energy with electron parallel kinetic energy $E_{em} + E_{\parallel e}$ are derived in GRILLIX. In figure 3.2.7 the energy conservation is plotted for each energy including all parts on the right side of equations (2.5.1)-(2.5.4) in order to demonstrate the energy balancing of each term. Each energy form is conserved quite well as is demonstrated by the overlap of the time derivative curve with the dashed curve which represents the sum of all parts on the right side

in the energy theorem. In figure 3.2.8 the total energy theorem is shown. The overall energy is conserved very well. The only remaining terms on the right side of the total energy theorem are the sources and sinks. The terms coming from the new advective derivative in section 2.7.1 were not included in the diagnostics indicating that these terms are indeed negligibly small. Each energy form e.g parallel advection $-u_{\parallel i} \nabla_{\parallel} p_e$ in E_{\parallel} has a corresponding counterpart in another equation $+u_{\parallel i} \nabla_{\parallel} p_e$ in $E_{em} + E_{\parallel e}$ balancing each other leading to the total energy conservation. This fact shows that the energy is not simply conserved in GRILLIX on the discrete level, even more the energy transfer mechanism remains valid.

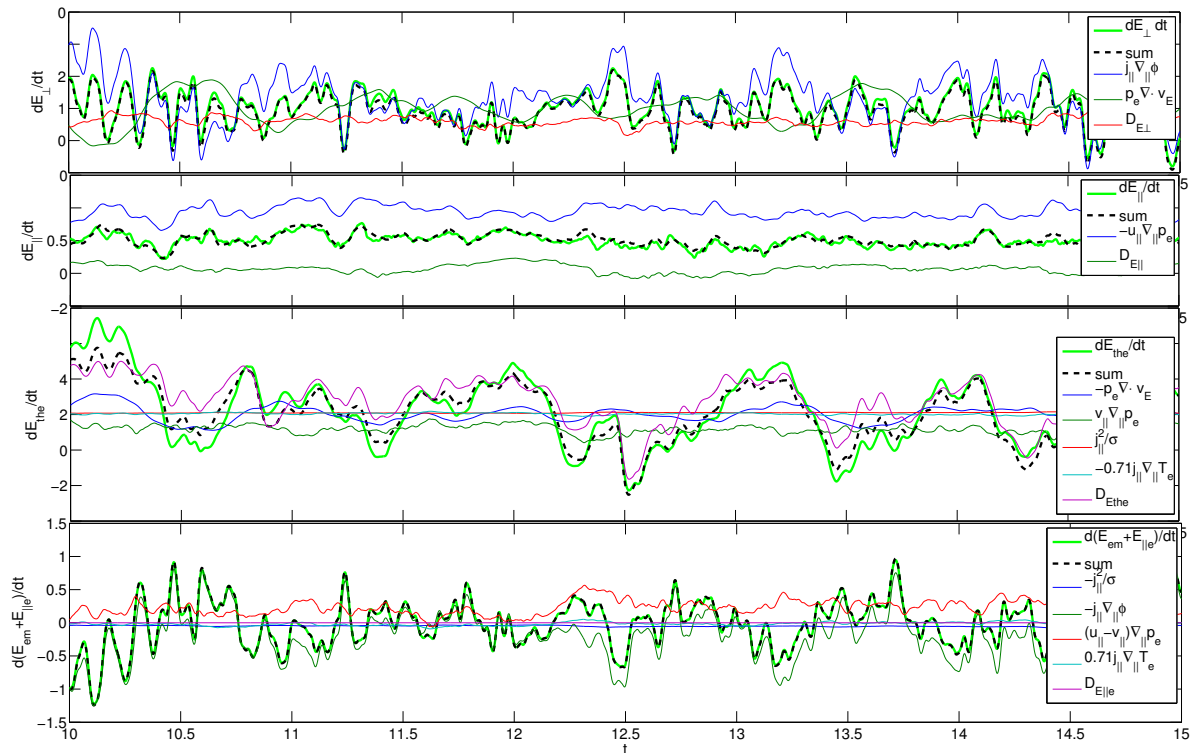


Figure 3.2.7: Energy conservation properties in GRILLIX. All energies are conserved well. The lime curve represents the time derivative of the corresponding energy overlaps with the dashed line which is the sum of all energy forms on the left side of equations (2.5.1)-(2.5.4).

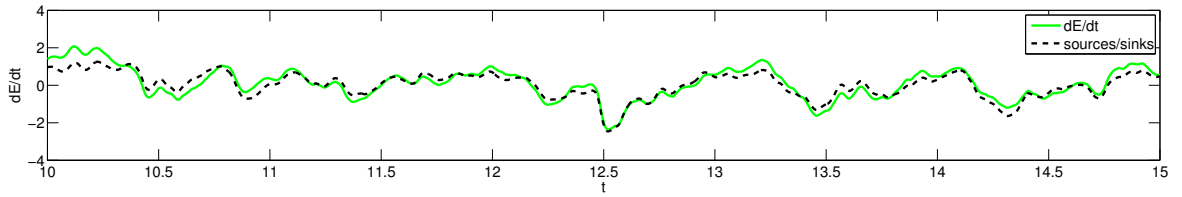


Figure 3.2.8: The total energy is conserved very well. The remaining terms on the right side are the sources and sinks. The energy transfer mechanism remains valid in GRILLIX simulations.

Impact of Boussinesq approximation

In [75] the turbulence dynamics was compared in the electrostatic global model and the conservative Boussinesq model from section 2.7.2. The biggest difference was the higher fluctuation level in the global system. The profiles almost overlapped as did the convective transport of energy and density. The neglect of ohmic heating in the equations leads to a decaying thermal energy transport in both systems. Here the complete global electromagnetic model is compared with the Boussinesq system. Moreover the impact of the non-conservative form of the Boussinesq approximation is shown.

In figure 3.2.9 the profiles $\langle n \rangle_{y,z,t}$ and $\langle T_e \rangle_{y,z,t}$, the fluctuation level $\hat{f} = \sqrt{\langle (f^2 - \langle f \rangle^2) / \langle f \rangle^2 \rangle_{y,z,t}}$, convective and diffusive transport of particles

$$\Gamma_n = \Gamma_n^C + \Gamma_n^D = \langle n v_{E \times B} \rangle_{y,z,t} + \langle D \partial_x n \rangle_{y,z,t} \quad (3.2.9)$$

and thermal energy

$$\Gamma_p = \Gamma_p^C + \Gamma_p^D = \frac{3}{2} \langle p_e v_{E \times B} \rangle_{y,z,t} + \frac{3}{2} n \langle D(T_e) \rangle_{y,z,t} + \frac{3}{2} T_e \langle D(n) \rangle_{y,z,t} \quad (3.2.10)$$

are shown for the Boussinesq system (BS) and full system (FS).

Here $\langle \dots \rangle_{y,z,t}$ indicates the poloidal, toroidal and time average, respectively.

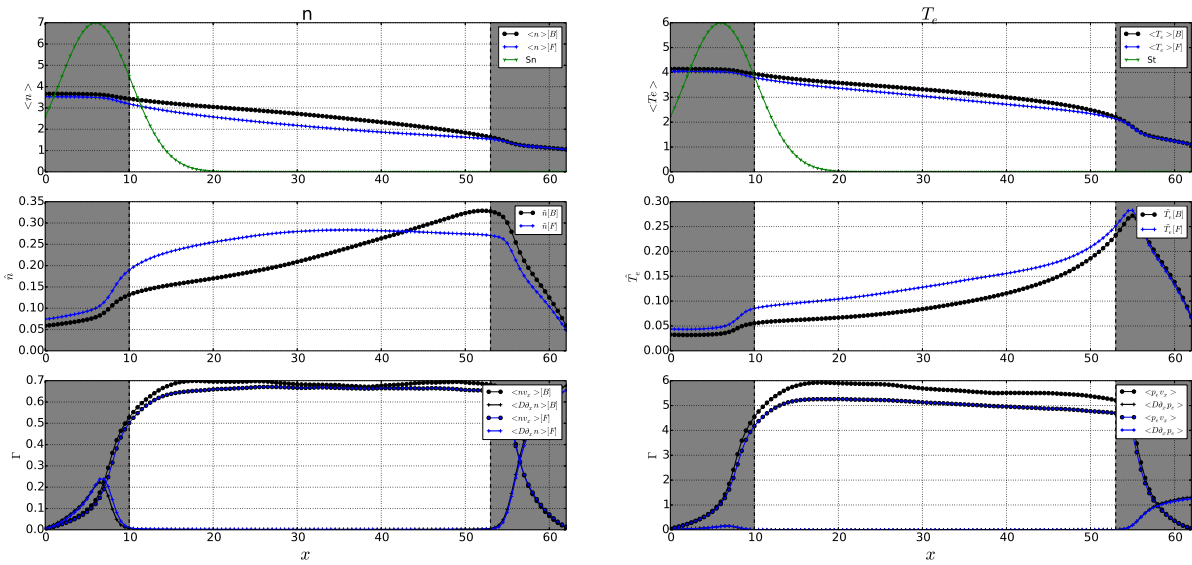


Figure 3.2.9: Comparison between BS (black) and FS (blue) for the profiles, the energy and particle transport and fluctuation levels.

The results are qualitatively very similar. The difference in profiles between FS and BS is slightly increased compared to the electrostatic model. The biggest difference is the fluctuation level which is higher in FS. Furthermore the fluctuation level of the density shows in FS a different shape remaining almost flat in the source free region which is not the case in BS. The convective transport of the thermal energy is now almost flat in the source free region. Strong convective particle transport indicates that transport is dominated by turbulence in the source free region. A general statement about the impact of the Boussinesq approximation would require a scan over a wide range of parameters, models and geometries. Nevertheless one can conclude from the findings in the electrostatic model and in the electromagnetic model used here by taking into account the result from section 3.1.4 that the Boussinesq approximation has an impact on the overall dynamics beyond the assumptions on the density. Although the Boussinesq approximation does not enter the electromagnetic part of the equations it has an impact on, for example the shape of the fluctuation level of the density although the density gradient is comparable to the electrostatic case.

Non-conservative Boussinesq approximation

Finally the same simulation is repeated using the non-conservative Boussinesq approximation from section 2.7.2. The system shows a completely different behavior. A typical result is shown in figure 3.2.10. The snapshot shows the density and potential at the same plane and time like in figure 3.2.4. The potential indicates a strong negative parabolic shape. This leads to a strong poloidal $E \times B$ -flow of the plasma smearing out the structures coming from the source region. Later in the simulation the potential gets even more negative causing a poloidal flow which largely suppresses the turbulence! Finally the simulation crashes due to the poloidal flow which gets too intense. The poloidal flow is a direct consequence of the lost conservation properties in the vorticity equation. This finding strongly emphasizes the importance of the conservation properties. By chance the lost conservation properties may not show up either by the use of a different geometry or other boundary conditions. However the results produced in such an environment are at least doubtful as it is hard to say how exactly the turbulent dynamics is affected by the lost conservation properties.

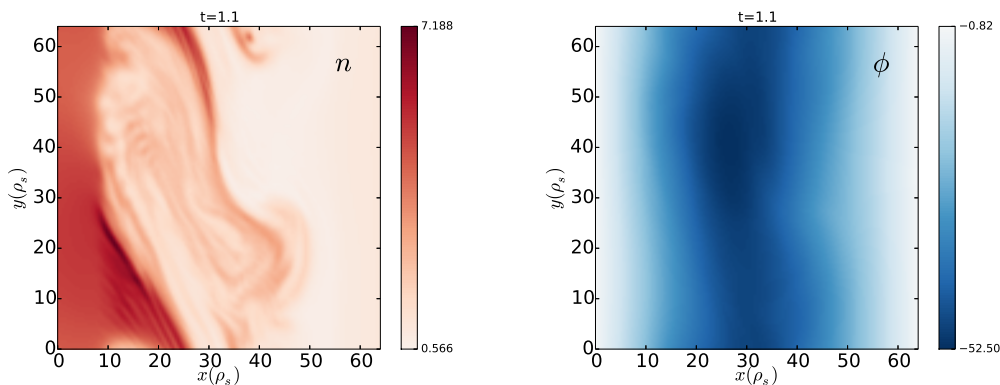


Figure 3.2.10: Non-conservative Boussinesq approximation creates a strong poloidal flow. This flow accelerates and finally suppresses the turbulence leading to a crash of the simulation.

Summary

In this chapter several fundamental tests were performed in order to check whether GRILLIX simulations yield the expected dynamics. The Alfvén dynamics was tested within a relative simple delta-f model where an analytical dispersion relation can be derived. It showed that the Helmholtz solver in GRILLIX works very well. Another important test is the check of the conservation properties. It was shown that the numerical scheme in GRILLIX conserves energy and particles to good accuracy. As far as known this test is still a missing part in other plasma turbulence codes. Without conservation properties the accuracy of the results becomes questionable. The comparison between the global model and the conservative Boussinesq model did not show a qualitative difference but it is suggested that the Boussinesq approximation may have an impact on the overall dynamics which is hard to foresee. The non-conservative form of the Boussinesq approximation, which still can be found in literature, yielded a significant different result. The loss of conservation properties in the vorticity equation translates into strong poloidal flows, which suppress the turbulence, leading finally to a crash of the simulation. This effect may be overlapped in other geometries or by other parameters. In principle it is always present with an impact on the turbulence which is absolutely not desired.

3.3 LARGE PLASMA DEVICE (LAPD)

The Large Plasma Device (LAPD) is a linear machine which provides a very useful environment for the study of plasma turbulence and transport. Plasma can be created at the size and scale of many fusion machines. The axial magnetic field hitting material walls at the end of the device leads to a situation similar to the scrape-off layer. Although the densities and temperatures are usually smaller compared to a fusion plasma, the size of the machine allows the growth of many modes in parallel and perpendicular directions, leading to a wide range of turbulent processes relevant for actual fusion devices [115]. It is a perfect test case for a validation of GRILLIX. In the validation process, the simulation results are compared to real experimental data. In general, the more features of the experiment can be reproduced by simulations the more valid is the model and the implementation of it. Here for the first time GRILLIX results within the global electromagnetic model are compared to experimental data from LAPD. In addition to the verification tests from section 2.8.7, the blob tests from chapter 3.1 and the Alfvén and conservation tests from section 3.2., experimental validation is an important milestone on the way to a reliable fluid code having predictive capabilities. Previous works on LAPD used an electrostatic model with the non-conservative Boussinesq approximation [22,23] or a superficial geometry neglecting the parallel boundaries [116]. In this light this chapter takes the LAPD modeling efforts one step forward. First the LAPD experiment is introduced. It is discussed afterwards how the experiment is modeled in GRILLIX. The validation results are shown in the end of this chapter. The impact of the Boussinesq approximation is discussed in the last section.

3.3.1 LAPD experiment

A schematic view of the experiment is shown in figure 3.3.1. The vacuum chamber is surrounded by axial magnetic coils (yellow and violet) which are separately connected allowing many magnetic field configurations.

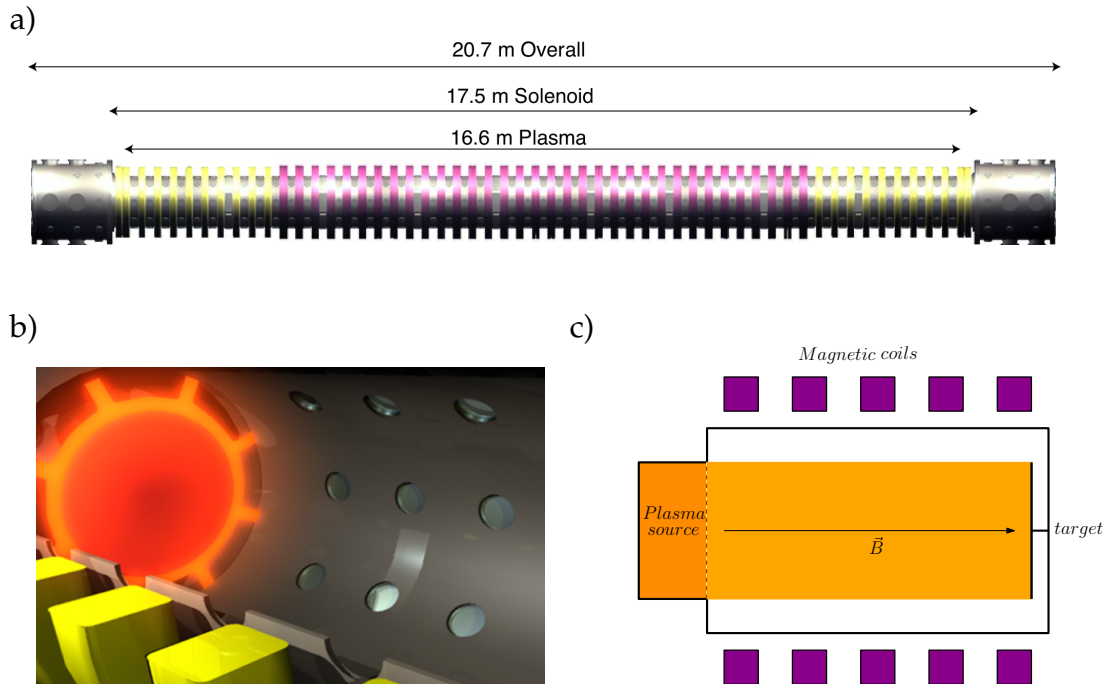


Figure 3.3.1: a) Schematic side view of the LAPD experiment. The picture was taken from [117]. The vessel is surrounded by magnetic coils. b) The barium-oxide cathode acts as plasma source. c) Schematic view of the inner of the vessel. Plasma is created and travels along the magnetic field hitting the target plate.

A barium-oxide coated, nickel cathode is heated to emission temperature of about 850°C . A discharge of a few thousand Amperes of current creates free electrons. A mesh anode is located next to the cathode which is about 50% transparent allowing a part of the electrons to travel down the length of the device and fill the chamber with plasma. The rate of emission of the plasma source can be adjusted. The plasma column has a length of approximately 17 meters and a diameter of up to 60 cm. In the following table the typical values of the LAPD plasma are given:

Parameter	
max. density n	$2.0 \times 10^{12} \text{cm}^{-3}$
max. T_e	6eV
max. T_i	0.5eV
$\lambda_p(\text{Alfven})$	2.0m
v_A	$7.7 \times 10^7 \text{cm/s}$
c_s	$1.2 \times 10^6 \text{cm/s}$
Plasma β	0.0015
species	<i>He</i>
charge state Z	1

Here a Helium plasma is going to be investigated. The cold ion assumption is reasonable in LAPD. It is important to note that the plasma β_0 is relatively high such that an electrostatic treatment is not justified in LAPD [118].

3.3.2 Dominant Instabilities

In a linear device like LAPD three main instabilities occur, the resistive drift wave instability, the interchange instability and the Kelvin-Helmholtz instability. The resistive drift wave arises due to the presence of a pressure gradient. It has been shown in section 3.2.1 that it couples to the Alfvén waves, leading to resistive drift-Alfvén instability. The interchange instability arises due to the rotation of the plasma column. In order to understand the cause of the self-generated plasma rotation one has to recapitulate the impact of the sheath boundary conditions from section 2.6. The potential follows the electron temperature very closely with $\phi = \Lambda T_e$. The electron temperature source has a top-hat like form, leading to a gradient in the potential which drives the $E \times B$ -rotation of the plasma. The centrifugal force drives the interchange instability mixing higher density region with lower density. The sheared plasma rotation causes also the Kelvin-Helmholtz instability. All three instabilities can be present in a linear device at the same time and are going to be discussed in more detail.

Resistive Drift Wave Instability

Drift waves can occur in every quasi-neutral magnetic configuration with a pressure gradient. A sinusoidal pressure perturbation is assumed as shown in figure 3.3.2. If the electrons follow a Boltzmann distribution then the

initial pressure perturbation will lead to a potential perturbation according to

$$\frac{e\tilde{\phi}}{T_e} = \frac{\tilde{p}_e}{p_{0e}}.$$

The potential perturbation causes an $E \times B$ -advection of the plasma. Above the positive charge accumulation the $E \times B$ -flow lowers the density. Below the charge accumulation the situation is opposite. This causes a motion of the entire perturbation with the diamagnetic velocity, giving the wave its name. If the Boltzmann response of the electrons is perturbed in some way, e.g. by low parallel conductivity, then the phase between the pressure and potential is shifted. In this situation the initial perturbation is amplified instead of creating a pure wave, leading to a drift-wave instability. A drift wave is a full three dimensional effect. Charge imbalance can only occur in the parallel direction as any charge imbalances in perpendicular plane are annihilated by the $E \times B$ -flow of the plasma leading to charge mixing. Thus a parallel variation of the plasma must exist for the creation of the drift wave.

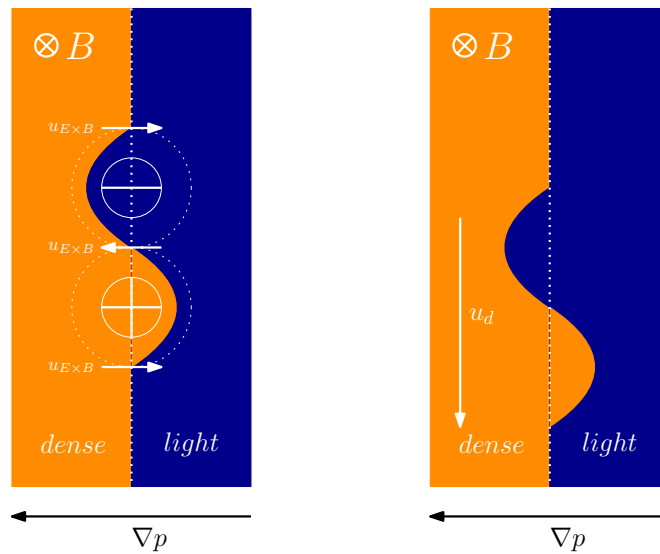


Figure 3.3.2: An initial perturbation of the electrostatic potential leads to an $E \times B$ -advection of the plasma. The perturbation propagates in the direction perpendicular to the initial pressure gradient and the magnetic field with the diamagnetic velocity.

Interchange Instability

Interchange instabilities are present in systems which are subject to a force acting in opposite direction to the density gradient leading to a interchange of high density plasma with low density plasma. The rotation of the plasma column leads to a centrifugal force. This force force causes a charge imbalance in perpendicular plane, leading to a $E \times B$ -flow amplifying the initial perturbation. The parallel dynamics is not important for the interchange modes but come into play when interchange modes couple to drift-waves.

Kelvin-Helmholtz Instability

The Kelvin-Helmholtz mode arises in regions of sheared flow where the flow on one side has a different density compared to the flow in the other side. A perturbation on the interface between this two regions creates vortices mixing the two plasma regions.

For the Kelvin-Helmholtz mode the parallel direction does not play a role. It was found in previous works [24] that the main driver for cross-field radial transport is the Kelvin-Helmholtz instability (KH) in LAPD.

3.3.3 *Modeling*

For the modeling of LAPD plasma the slab geometry is used. The perpendicular domain width spans from $-L_{\perp}/2$ to $L_{\perp}/2$ with $L_{\perp} = 1.4 m$. The parallel length is $L_z = 17 m$. The global electromagnetic model (1.7.1-1.7.5) is employed without the curvature terms $C(f) = 0$ with the LAPD parameters from the last section. The density and electron temperature sources are modeled with top-hat shaped profiles $S_{n,T}$ respectively

$$S_{n,T} = C_{n,T}(1 - \tanh[(r - r_s)/L_s])\exp(-\lambda_s z). \quad (3.3.1)$$

The ionization front decay in parallel direction is modeled with an exponential function where in normalized units $\lambda_s = 0.0813$. The strength of the sources are adjusted with $C_{n,T}$ and are chosen in order to match the experiment with $C_{n,T} = 0.27$. The sharpness of the sources is set with $L_s = 0.5$. The sources are localized in the center of the computational domain. Bohm boundary conditions are chosen according to section 2.6. In the radial direction Neumann boundary conditions are chosen on density and electron temperature. Dirichlet boundary conditions are chosen for the potential, vorticity and parallel ion momentum. A grid with $n_x = n_y = 128$ and

$n_z = 32$ was used for the simulations in this chapter. A full 3D turbulence simulation is shown in figure 3.3.3

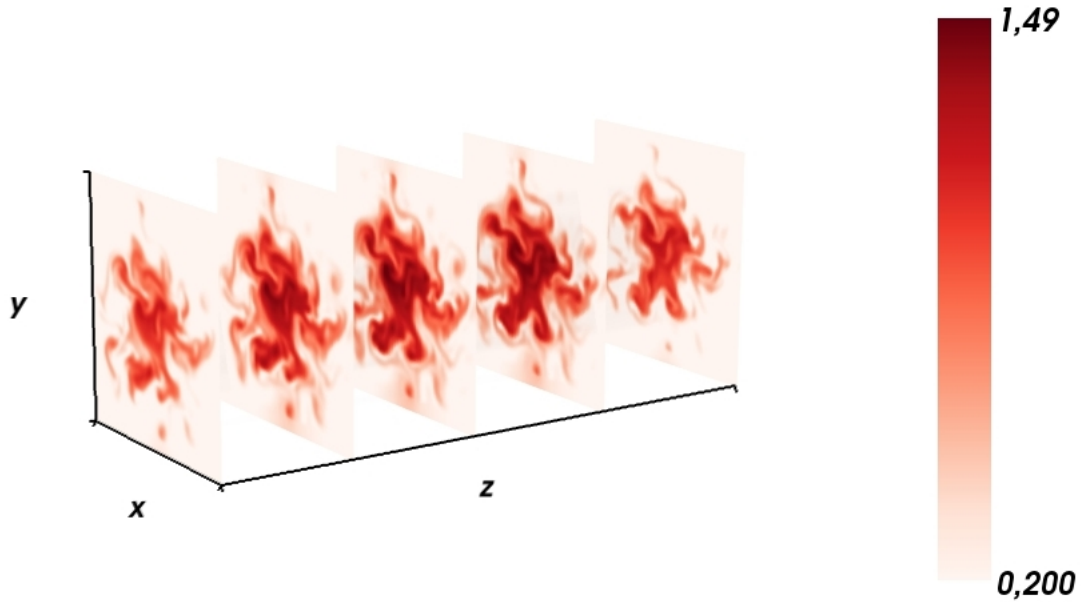


Figure 3.3.3: 3D turbulence simulation of LAPD with GRILLIX. Cut planes show density at $t = 42$. The first plane is located at $z = 0$. The last plane shows the density at $z = L_z$.

3.3.4 Validation

In this section the LAPD plasma is compared to the experiment. The top-hat shaped sources ramp up the density and electron temperature having steep gradients. The plasma is subject to several instabilities. Here the radial profiles, the fluctuation level, the probability distribution function (PDF) of fluctuations, the skewness of the PDF and the power spectrum of the turbulence will be compared to experimental data which were taken from [22, 119]. The result obtained using the conservative Boussinesq approximation is also included in the plots. The impact of the Boussinesq approximation is discussed in the last section. In figure 3.3.4 the density is shown at 3 time steps on the mid-plane. At the beginning the source keeps the top-hat shape. The drift-Alfvén waves instabilities which are shown in the second snapshot saturate at much smaller amplitudes compared to the KH instability as was

pointed out in [22]. The full saturated turbulent regime dominated by KH is shown in the last snapshot.

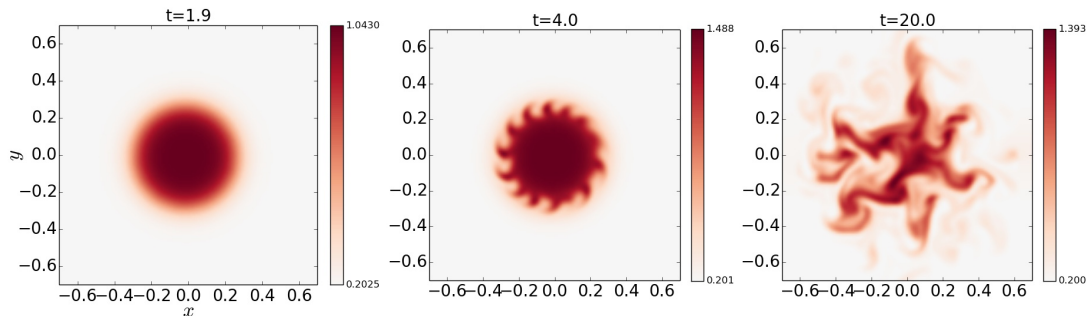


Figure 3.3.4: The plasma source at three stages during the development of turbulence. The top-hat shaped source decays into turbulence due to the onset of resistive drift-Alfvén wave instabilities. Turbulence is dominated by KH instability.

PROFILES The radial profile is compared to the experiment at the poloidal position $y = 0$, see figure 3.3.5. GRILLIX data is in qualitative agreement with the experiment. The main deviation is the absolute value of the density in the source region $r < 0.28m$.

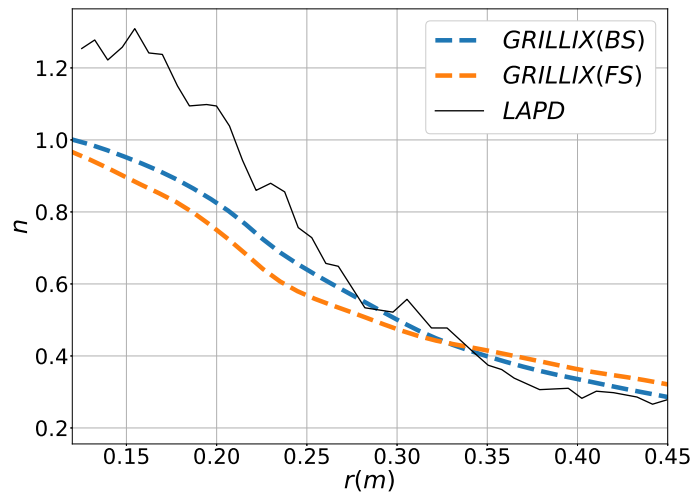


Figure 3.3.5: Radial density profile compared to the LAPD experiment shows qualitative agreement. Deviation in absolute value of the density in the source region.

FLUCTUATION LEVEL The fluctuation amplitude $\delta n = n - \bar{n}$ normalized to the maximum value of the density n_{max} is shown in figure 3.3.6. The maximum value of the fluctuations appear on the source boundary where the gradients are steepest. The GRILLIX simulation results are in qualitative agreement with the experiment, although GRILLIX result is slightly higher.

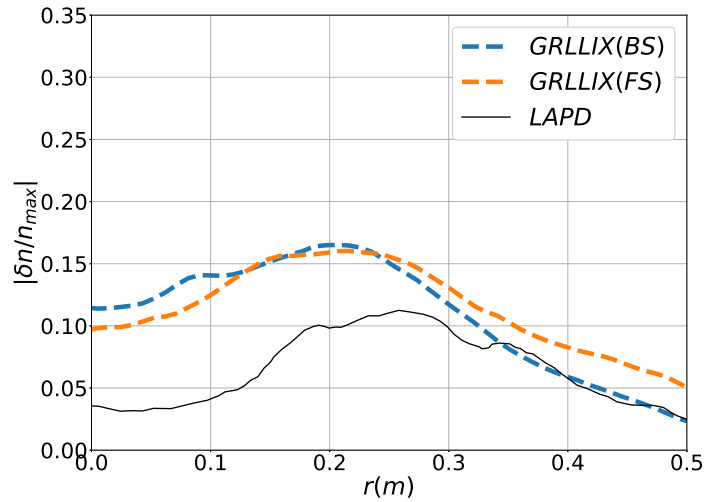


Figure 3.3.6: Fluctuation level is in qualitative agreement with the experiment. The maximum value appears at the source boundary, where GRILLIX simulation results are a factor of half higher.

PROBABILITY DISTRIBUTION FUNCTION The PDF of the fluctuations normalized to the root mean square $rms(\delta n)$ was averaged at the source boundary in the experiment $0.22m \leq r \leq 0.28m$. The comparison to GRILLIX simulation is shown in figure 3.3.7. The PDF produced by GRILLIX is in excellent agreement with the experiment. It has a nearly Gaussian shape indicating a pure uncorrelated behavior of the plasma in the gradient region.

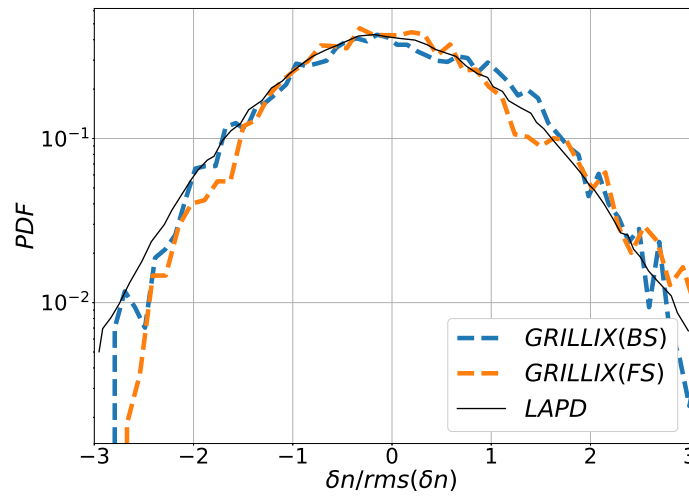


Figure 3.3.7: The probability distribution function is in very good agreement with the experiment.

SKEWNESS The skewness of the PDF indicates the deviation from a normal distribution

$$\gamma = \frac{\frac{1}{N_t} \sum_{t=1}^{N_t} \delta n^3}{\left(\frac{1}{N_t} \sum_{t=1}^{N_t} \delta n^2\right)^{3/2}}.$$

It is a statistical measure for the presence of holes and blobs in plasma. A negative skewness is an indicator for the presence of holes. A positive skewness indicates blobs. The comparison of the experimental skewness to GRILLIX simulations is shown in figure 3.3.8. GRILLIX captures the overall skewness to good agreement with experimental results. As in experiment, the dynamics is dominated by holes in the source region. The source free region is dominated by blobs.

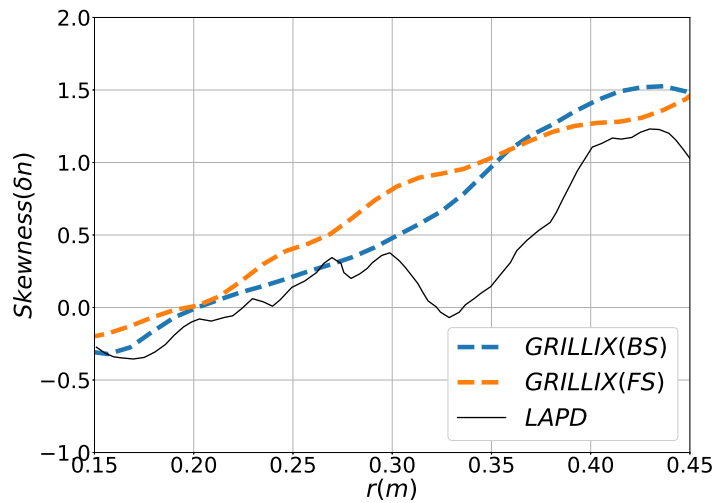


Figure 3.3.8: The skewness is in qualitative agreement. The overall trend indicates that in the source region plasma dynamics are dominated by holes, whereas in the source free region the dynamics are dominated by blobs.

POWER SPECTRUM Finally the power spectrum of normalized density fluctuations $\delta n/n$ is analyzed. It shows how the power is distributed along the frequencies of the turbulence. The result is shown in figure 3.3.9. The GRILLIX power spectrum fits the experiment almost perfectly over a large frequency range. It is a strong indication that GRILLIX captures the main turbulence dynamics to high accuracy.

The deviations between GRILLIX results and the experiment can have several reasons. First there are uncertainties on the experimental side, meaning that it is not obvious in details how and where in the machine the experimental data presented here was collected e.g the profiles of the density differ between [119] and [22] although similar plasma parameters were used. Second, the question arises if the experimental data shows general results. As was pointed out in [22], also other values for e.g. the fluctuation level have been measured. In GRILLIX a plasma source on a constant plasma background of 0.2 is simulated. However in the experiment the situation is different. The plasma column is surrounded by neutral gas. The global electromagnetic model lacks of neutrals dynamics which are important in LAPD [119, 120].

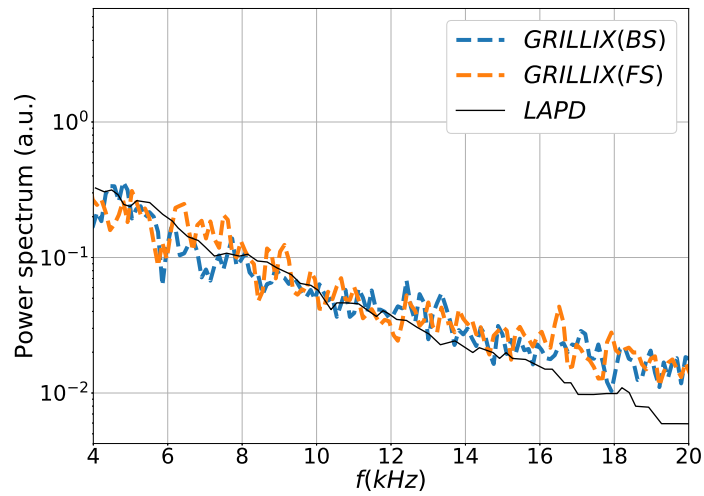


Figure 3.3.9: The power distribution of the turbulence matches the experiment.

Impact of Boussinesq approximation

The difference between the full system (FS) and the Boussinesq system (BS) the initial onset of the instability in the density is considered in figure 3.3.10 at a very early time step. The difference between FS and BS is remarkable. The initial mechanism by which the plasma source decays into turbulence in BS totally different compared to FS. As was shown in chapter 3.1 the difference between BS and FS depends on the gradients in density and temperature. Before the onset of the instabilities which finally relax the gradients, the source has a top hat like shape with steep gradients. It means that the impact of the BS is strongest at the beginning of the simulation showing that the use of BS can strongly affect a turbulence simulation where steep gradients are present.

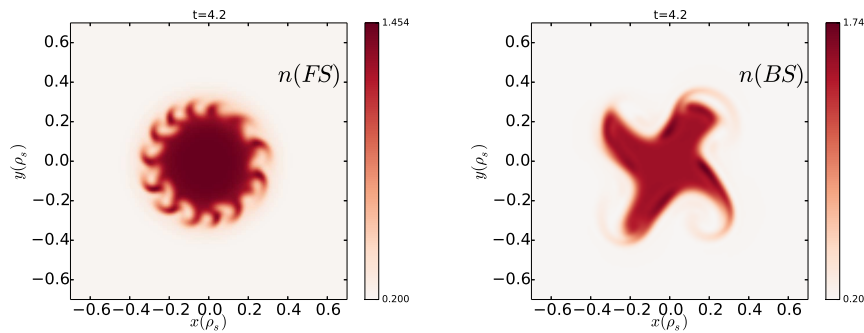


Figure 3.3.10: Comparison between the density in the full system (left) and the Boussinesq system (right) during the onset of the instability at early time step. The picture shows a clear difference between these two systems.

PROFILES In figure 3.3.5 the density profile is shown for BS and FS. It shows no qualitative difference.

FLUCTUATION LEVEL The fluctuation level in figure 3.3.6 is also very similar. The BS and FS are in qualitative agreement with the peak of the fluctuation level in the vicinity of the steepest gradients.

PROBABILITY DISTRIBUTION FUNCTION For both system the probability distribution function shows in figure 3.3.7 a Gaussian shape at the source edge.

SKEWNESS The skewness is in qualitative agreement between BS and FS

POWER SPECTRUM The power spectrum in figure 3.3.9 is in BS and FS very similar. The slope of the curves is equal in both systems indicating that the power distribution along the frequencies of the turbulence is equivalent.

Summary

In this chapter the focus was on the validation of GRILLIX. For the first time GRILLIX turbulence results were compared to experiment. The LAPD experiment is a very good test case for the simulation efforts as it includes the dynamics which can be found in the scrape-off layer. It was shown that GRILLIX captures the overall dynamics of the experiment. The profile matches qualitatively the experimental outcome. The fluctuation level is slightly higher than in the experiment but matches qualitatively the experiment. The PDF is in very good agreement with the experiment and also the skewness of the PDF. The power spectrum is an important measure for the turbulence dynamics. GRILLIX turbulence power spectrum is in excellent agreement with the experiment. The deviations between simulation and experiment might have several sources on the model and experiment side. Finally the impact of the Boussinesq approximation was investigated. The impact of the Boussinesq approximation is strongest when steep gradients are present like in the beginning of the simulation. When the turbulence relaxes the gradients the difference between the models is less pronounced. It is possible that the Boussinesq approximation has a strong impact on the turbulence when steep gradients are present.

FLUX-COORDINATE INDEPENDENT APPROACH

The previous chapters showed a step by step development and progress of a new model for GRILLIX. The system of equations was discretized on a slab grid which was verified with the method of manufactured solutions in section 2.8.7. The slab geometry was an efficient set up for the testing of blob dynamics and the comparison to analytical predictions in chapter 3.1. The Boussinesq approximation was relaxed and the impact of it was investigated on closed field lines in a turbulence simulation in chapter 2.2 where also very good conservation properties of GRILLIX were shown. The Alfvén dynamics was also tested and yielded excellent agreement with analytical predictions. These efforts were taken one step further in chapter 3.3 where for the first time GRILLIX turbulence simulations were compared to the LAPD experiment showing good qualitative agreement. All of these steps pose a solid foundation for the transition of the global electromagnetic model to realistic magnetic geometries which are going to be investigated in this chapter. Here the focus is on the comparison between a single-null, double-null and circular geometries in the closed field line region. The open field line region was not considered, due to a lack of the implementation of the parallel boundary conditions, which poses a major challenge and will be discussed in chapter 5. First the discretization of the equations in these geometries will be discussed. The geometries are presented in more detail and it is pointed out that the unique feature of GRILLIX namely the use of a Cartesian grid in the poloidal planes allows for a very efficient calculation of radial transport of the plasma. In addition to this result the radial transport, profiles and fluctuation levels are presented.

4.1 DISCRETIZATION

In section 2.8.4 the discretization of the system of equations was shown. Figure 2.8.3 showed that in the slab geometry used in the last chapters the magnetic field lines are normal to the poloidal planes always hitting the grid points. This allowed a relatively straight forward discretization of the parallel gradient and divergence. Also the mapping of the quantities on the staggered grid was in fact the average value of the quantity. The formal discrete form of the equations is very advantageous in terms of flexibility. Once the equations are written in terms of the mapping operators e.g. Eq. 2.8.17 changing the geometry converts into changing the mapping operators \mathbf{Q} and \mathbf{Q}^* . The scheme for toroidally staggered FCI approach is shown in figure 4.1.1. For clarity we restrict the discussion here to a 2D setup, where φ is the toroidal direction x mimics the poloidal plane. The transition to the 3D case is straight forward. It is clear that the magnetic field lines do not coincide with the grid points anymore. Furthermore the length along a magnetic field line is denoted as $s_j^- + s_j^+$. The parallel gradient is discussed here in its simplest form in this setting. The more advanced version, which is based on a flux box integration including map distortions can be found in [9,45,46].

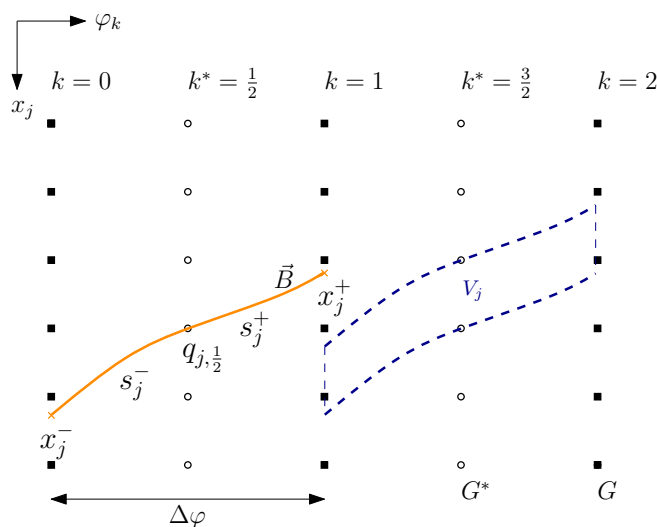


Figure 4.1.1: Scheme for toroidally staggered FCI approach. The staggered grid G^* is shifted by $\frac{\Delta\varphi}{2}$ compared to the grid G in the toroidal direction.

The FCI version of the parallel operator, see Eq. (2.8.9) is given by

$$\mathbf{q}^{\parallel}_{k^*} := (\mathbf{Q}f)_{k^*} := \frac{f_{k+1}(x_j^+) - f_k(x_j^-)}{s_j^+ + s_j^-}. \quad (4.1.1)$$

The quantity on the penetration points of the magnetic field line with the poloidal plane $f_{k+1}(x_j^+)$, $f_k(x_j^-)$ are found via interpolation. The coefficients of interpolation are stored in the sparse matrix \mathbf{Q} . In similar fashion the mapping operator \mathbf{M} , see Eq. (2.8.11) to the staggered grid is rewritten giving

$$(\mathbf{M}f)_{k^*} = \frac{f_{k+1}(x_j^+)s_j^- + f_k(x_j^-)s_j^+}{s_j^+ + s_j^-}. \quad (4.1.2)$$

The direct discretization along a magnetic field line of the parallel divergence is given by

$$D_{\parallel}f = \frac{2}{s_j^+ + s_j^-} [(\nabla_{\parallel}f)_{j,k+\frac{3}{2}} - (\nabla_{\parallel}f)_{j,k+\frac{1}{2}}] \quad (4.1.3)$$

This scheme causes spurious perpendicular numerical coupling, which can be even larger than real dynamics. It turns out to be advantageous to discretize the parallel divergence in FCI with the support operator method [9, 121, 122]. The first order operator is discretized, here the parallel gradient Eq. (4.1.1), then the second order discrete operator is constructed via a discretization of a scalar product $\langle \cdot, \cdot \rangle$ and the keeping of certain integral properties i.e. adjointness

$$\begin{aligned} \langle u, D_{\parallel}f \rangle &= \int_V dV u \nabla \cdot [(\nabla_{\parallel}f)\mathbf{b}] = - \int_V dV \nabla_{\parallel}u \nabla_{\parallel}f = - \langle \nabla_{\parallel}u, \nabla_{\parallel}f \rangle \\ &\rightarrow \nabla_{\parallel}^{\dagger} = -\nabla \cdot [\mathbf{b}\cdot] \end{aligned} \quad (4.1.4)$$

The surface terms have been dropped here as they only enter through boundary conditions. The equality (4.1.4) is brought to the discrete level giving

$$\sum_{\alpha,\beta,\gamma} \mathbf{u}_{\alpha} (\nabla \cdot [(\nabla_{\parallel}\mathbf{f}_{\gamma})_{\beta,\gamma}])_{\alpha,\beta} \mathbf{V}_{\alpha} = - \sum_{\mu,\nu,\tau} (\nabla_{\parallel}\mathbf{u})_{\mu,\nu} (\nabla_{\parallel}\mathbf{f})_{\mu,\tau} \mathbf{V}_{\mu} \quad (4.1.5)$$

where Greek indices denote a summation over all grid points here. A relabeling of the indices $\mu \rightarrow \alpha$, $\nu \rightarrow \beta$ and $\tau \rightarrow \gamma$ leads to the final

expression of the discrete parallel divergence, which is the negative adjoint of the parallel gradient

$$\mathbf{Q}^* = -\mathbf{V}^{-1}\mathbf{Q}^T\mathbf{V}, \quad (4.1.6)$$

where \mathbf{V} is a diagonal matrix containing the flux box volumes V_j .

4.2 GEOMETRIES

In this chapter the geometries shown in figure 4.2.1 are used. In the following they are introduced in more detail.

Circular geometry

In the circular geometry the magnetic field is prescribed with a safety factor

$$q(\rho) = q_0 + s(\rho - \rho_0), \quad (4.2.1)$$

where the flux surface label in normalized units $\rho = \sqrt{(R-1)^2 + Z^2}$ with the bound $\rho \in [\rho_{min}, \dots, \rho_{max}]$ and the reference value q_0 is at the central flux surface $\rho_0 = (\rho_{max} + \rho_{min})/2$. The constant magnetic shear is s .

Single-Null geometry

For the single-null geometry the magnetic field is prescribed as

$$\mathbf{B} = \nabla\varphi + \nabla\varphi \times \nabla\psi. \quad (4.2.2)$$

The toroidal angle is given by φ . The poloidal flux function ψ is taken from an exact solution of the Grad-Shavranov-equation from [123] having the form

$$\begin{aligned} \psi(R, Z) = & 0.0159 - 0.0363 R^2 - 0.00262 R J_1(5.836 R) \\ & - 0.0117 R(1.769 Z - 0.231) J_1(5.836 R) \\ & - 0.0665 R Y_1(5.836 R) \\ & - 0.0461 R J_1(4.669 R) \cos(3.502 Z - 0.457) \\ & + 0.0360 R J_1(3.502 R) \cos(4.669 Z - 0.610) \\ & + 0.0218 R J_1(0.584 R) \cos(5.807 Z - 0.758) \\ & - 0.0383 R J_1(6.825 R) \cosh(3.537 Z - 0.462) \\ & + 0.0238 R J_1(4.669 R) \sin(3.502 - 0.457) \\ & - 0.00926 \sin(5.836 Z - 0.762) \end{aligned} \quad (4.2.3)$$

with the Bessel functions of first order J_1 and second order Y_1 . Here the flux label is defined as $\rho = \sqrt{(\psi - \psi_0)/(\psi_x - \psi_0)}$, where ψ_0 is the poloidal flux at the magnetic axes and ψ_x is the magnetic flux at the separatrix.

Double-null geometry

For the double-null configurations the non-symmetric parts are removed from Eq. (4.2.3) yielding

$$\begin{aligned} \psi(R, Z) = & 0.0159 - 0.0363 R^2 - 0.00262 R J_1(5.836 R) \\ & - 0.0665 R Y_1(5.836 R) \\ & - 0.0461 R J_1(4.669 R) \cos(3.502 Z - 0.457) \\ & + 0.0360 R J_1(3.502 R) \cos(4.669 Z - 0.610) \\ & + 0.0218 R J_1(0.584 R) \cos(5.807 Z - 0.758) \\ & - 0.0383 R J_1(6.825 R) \cosh(3.537 Z - 0.462) \end{aligned} \quad (4.2.4)$$

One advantage of the use of a Cartesian grid within the poloidal planes becomes clear when considering the poloidal resolution of the flux surfaces in the single-null or double-null geometries. It is shown in figure 4.2.1 that the flux surface density and with it the resolution of a flux aligned grid are different across the poloidal section. The flux surfaces are stretched into the direction of the X-point leading to an imbalance of the resolution. This means that the numerical accuracy differs at different locations around the poloidal plane. However turbulence acts isotropically within poloidal planes. Consequently the Cartesian grid, providing everywhere the same resolution, is suited more for the simulation of turbulent dynamics. Moreover the stretched flux surfaces lead to a problem when calculating e.g. radial transport of the plasma for which perpendicular derivatives of the potential need to be calculated. If the resolution is not high enough in the stretched region the outcome becomes questionable. Increasing the resolution in the stretched region to a sufficient level leads to a very dense grid at the outboard mid-plane such that the simulation becomes very expensive or even not feasible due to limitations on the time step. The Cartesian grid allows GRILLIX to calculate the radial transport with the same numerical accuracy everywhere in the poloidal plane.

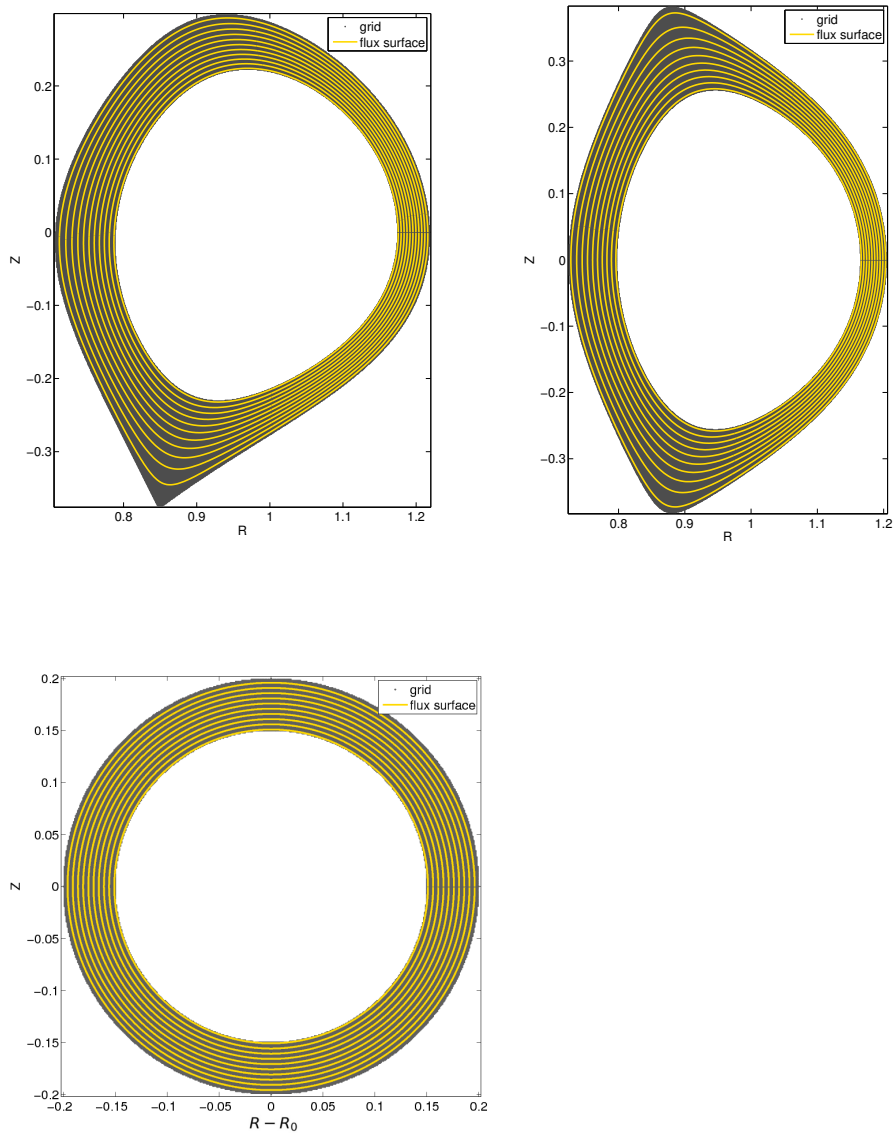


Figure 4.2.1: a) double-null geometry b) single-null geometry c) circular geometry with constant magnetic shear

The q -profiles in all geometries are shown in figure 4.2.2. In the circular geometry the parameters $q_0 = 2.75$ and $s = 10$ were chosen in order to match roughly the other geometries.

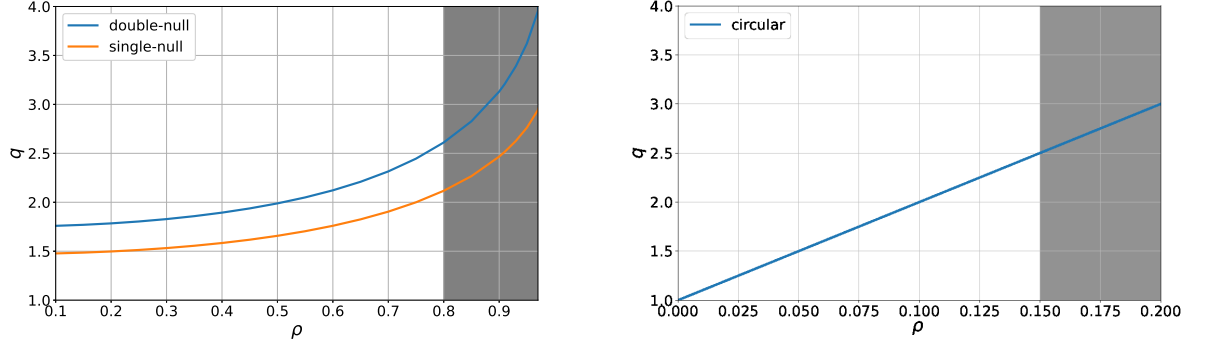


Figure 4.2.2: q -profiles: left: single-null (SN) and double-null (DN). right: circular geometry; shadowed area is the computational domain.

4.3 SIMULATION AND DIAGNOSTICS

In this section the profiles, fluctuation level and the radial transport are going to be calculated in the three geometries presented in the last section. For the turbulence simulations a hydrogen plasma with the following physical and numerical parameters was used

<i>physical parameters</i>		<i>numerical parameters</i>	
density n_0	$5.0E13 \text{ cm}^{-3}$	poloidal resolution h	$1.0E - 3$
el. temperature T_0	30 eV	toroidal resolution $\Delta\varphi$	$2\pi/16$
magnetic field B_0	1.5 T	\perp hyper-diffusion ($N = 6$)	10.0
major radius R_0	1.65 m	\parallel diffusion	0.15
flux surface label ρ	$[0.8, \dots, 1.0]$	target density and temp. $n_t T_{et}$	3.0

Here we focus on a qualitative comparison and results. A constant density and electron temperature background ($n, T_e = 1.0$) with small amplitude noise is initialized. All other quantities are set to zero in the beginning. The Gaussian sources ramp up the density and temperature to the target values. All quantities (density, electron temperature, vorticity, parallel ion velocity) are rotating clockwise, see figure 4.3.1, where the zonal average of the poloidal rotation velocity $\langle v_\theta \rangle$ is shown. This kind of rotation

was also observed in simulations with GBD code [31] and experimentally in e.g. ASDEX Upgrade [124]. The gradient of the poloidal velocity is higher in the circular geometry and shows a parabolic shape. In the outer region $\rho > 0.190$ the poloidal velocity changes direction. In figure 4.3.2 a density snapshot in a saturated turbulence regime is shown for all three geometries. It is important to note that although just one poloidal plane is shown, full 3D turbulence simulations were used in this chapter.

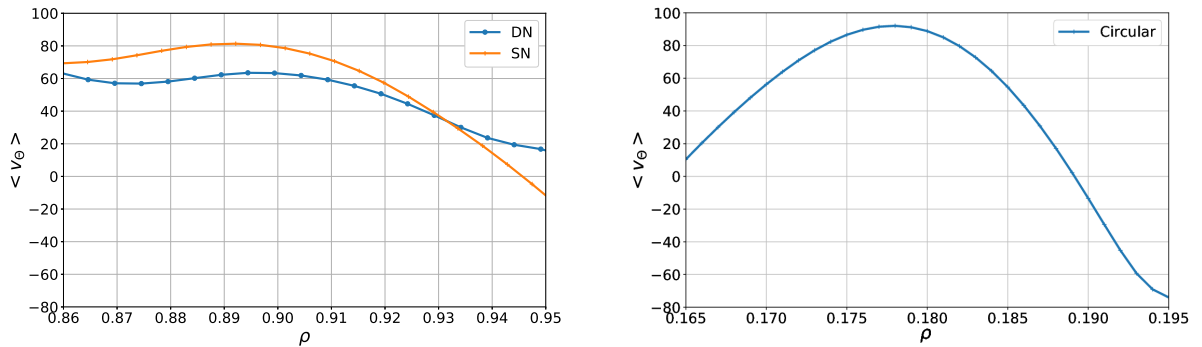


Figure 4.3.1: Zonal average of the poloidal velocity $\langle v_\theta \rangle$ along the flux surfaces. left: single-null (SN) and double-null (DN). right: circular geometry

PROFILES For the calculation of the profiles the density and electron temperature was averaged over the time and toroidal angle yielding $\langle n \rangle_{t,\varphi}$ and $\langle T_e \rangle_{t,\varphi}$. First the profiles in the circular geometry are considered. Here the density profile at the outboard mid-plane (LFS) is compared to the profile at the high field side (HFS). The result in figure 4.3.3 shows a clear difference between LFS and HFS. The ballooning on the LFS is stronger, relaxing the gradients more compared to HFS. A minor asymmetry between the upper side (UP) and the lower side (DOWN) is visible which was also observed in [31]. The asymmetry in density is more pronounced. As was pointed out in [31] the non-linear heat conduction relaxes the asymmetry in the electron temperature.

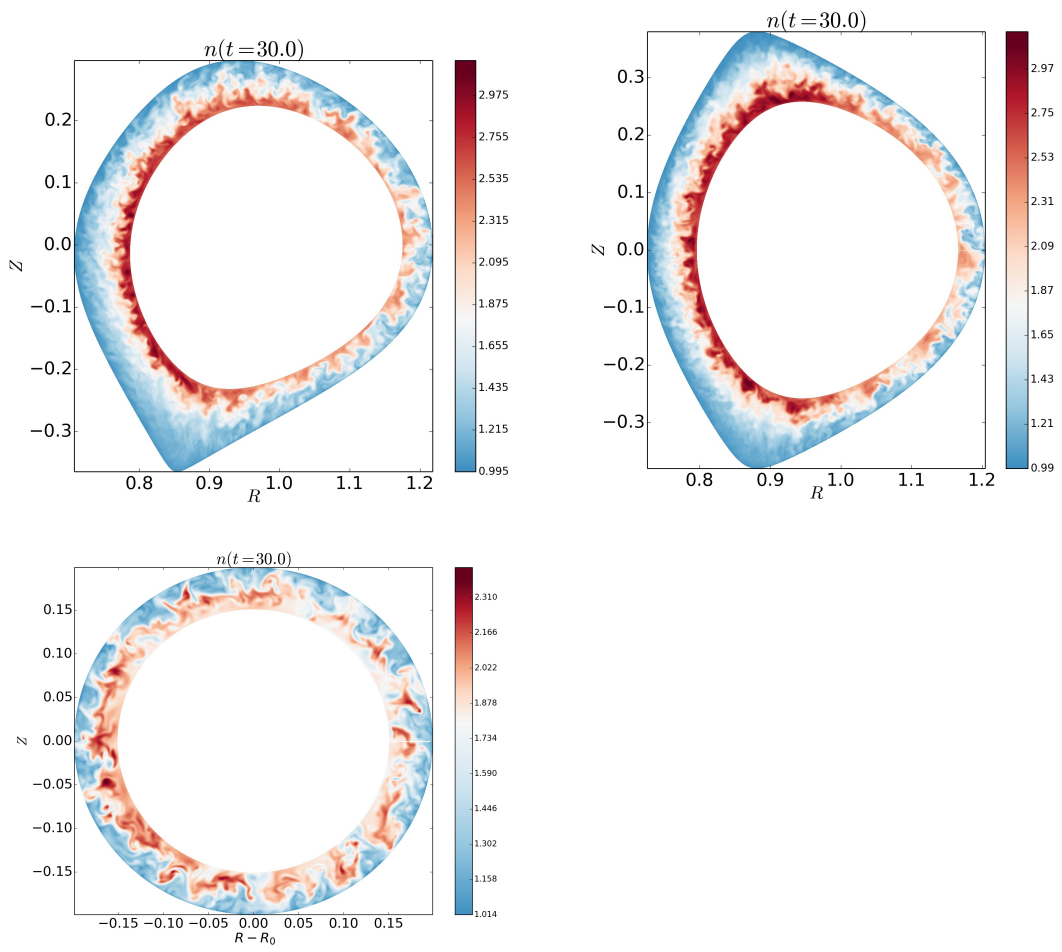


Figure 4.3.2: Density snapshot of saturated turbulence in all three geometries.

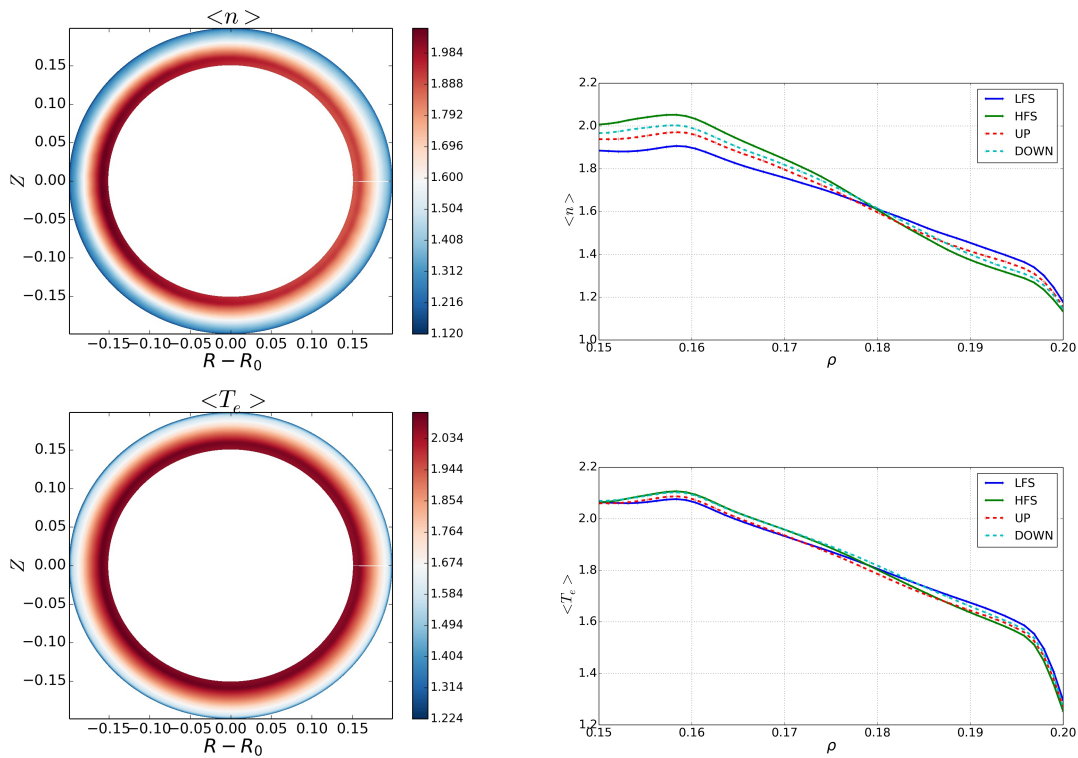


Figure 4.3.3: Density and electron temperature average $\langle n \rangle_{t,\varphi}$, $\langle T_e \rangle_{t,\varphi}$, in circular geometry. The profile is steeper on HFS compared to LFS. Minor Up-Down asymmetry in both quantities.

The profiles are compared in the single-null (SN) and double-null (DN) geometries at the LFS and HFS respectively. The result is shown in figure 4.3.4. First a clear difference between the LFS and HFS is visible in the density. The profiles at HFS are much steeper. The difference between LFS and HFS is much stronger compared to the circular geometry indicating that the HFS is more stable in SN and DN respectively. The difference in the electron temperature between LFS and HFS is less pronounced, which was also the case in circular geometry. The double-null geometry is symmetric, however the profile of the density is not. There is a clear up-down asymmetry in the density profile which is at the same time absent in the temperature. This finding is in line with the circular geometry. Although the circular and DN geometries are symmetric, the dynamics are not. The reason for this is the poloidal rotation of the plasma. The plasma rotates clockwise, meaning that on the lower side plasma is transported from the LFS into the more stable HFS. On the upper side, the situation is opposite. There, plasma is transported from the more stable HFS into LFS, causing the up-down asymmetry.

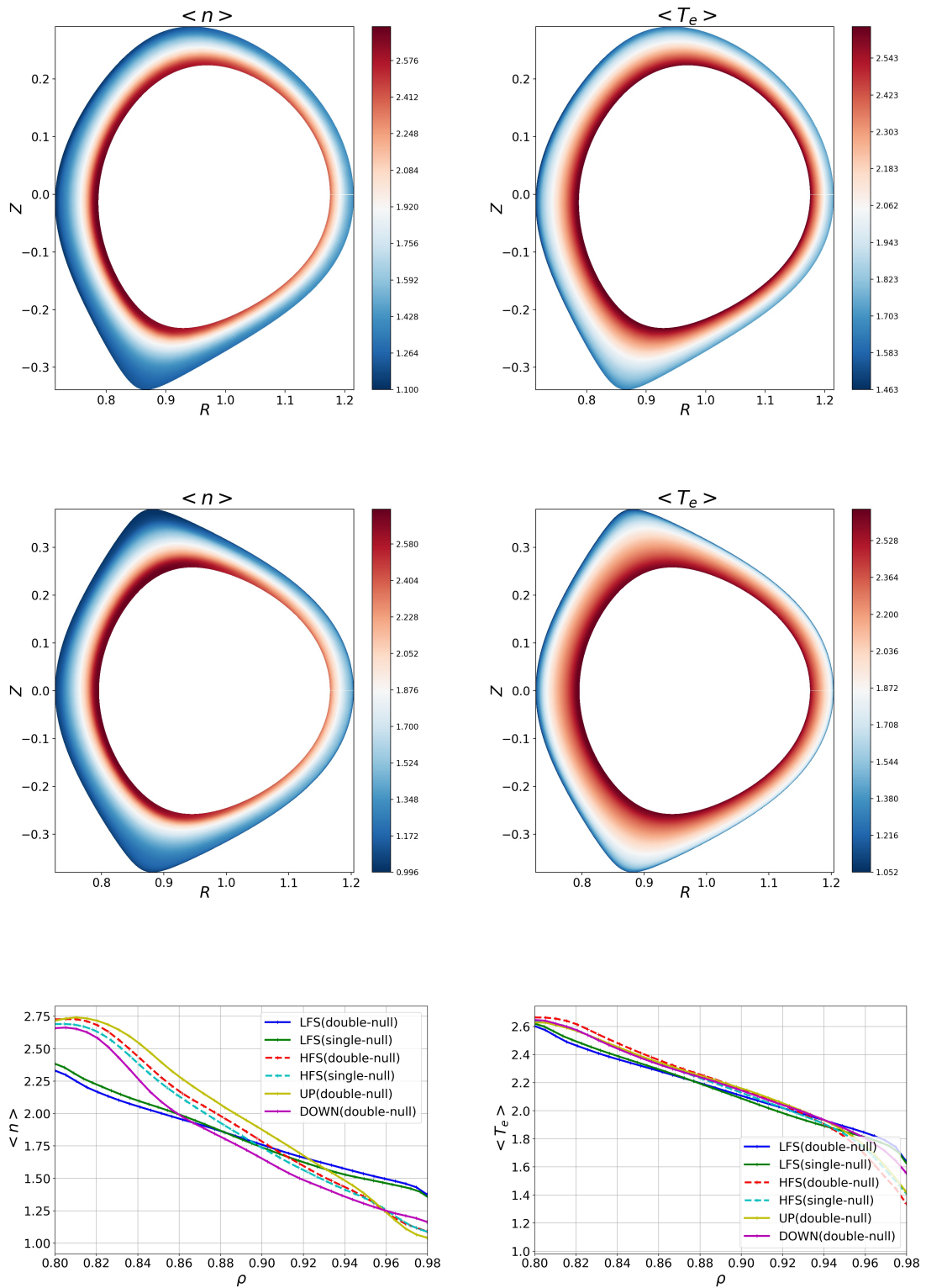


Figure 4.3.4: Density and electron temperature average in the single-null and double-null geometries. Comparison between LFS and HFS for both geometries.

FLUCTUATION LEVEL The fluctuation level is computed as the root mean square $RMS(f) = \sqrt{\langle (f - \langle f \rangle_{\varphi,t})^2 \rangle_{\varphi,t}}$ of the quantity. The results are presented for all three geometries for the density and electron temperature. In figure 4.3.5 the fluctuation level is shown for circular geometry. The maximum value for the density fluctuations is around $RMS(n)_{max} \approx 0.25$ for HFS, LFS, UP and DOWN. No clear ballooning is visible in the density. In the electron temperature the fluctuation is higher on the LFS. A slight asymmetry between the upper and lower side is also present.

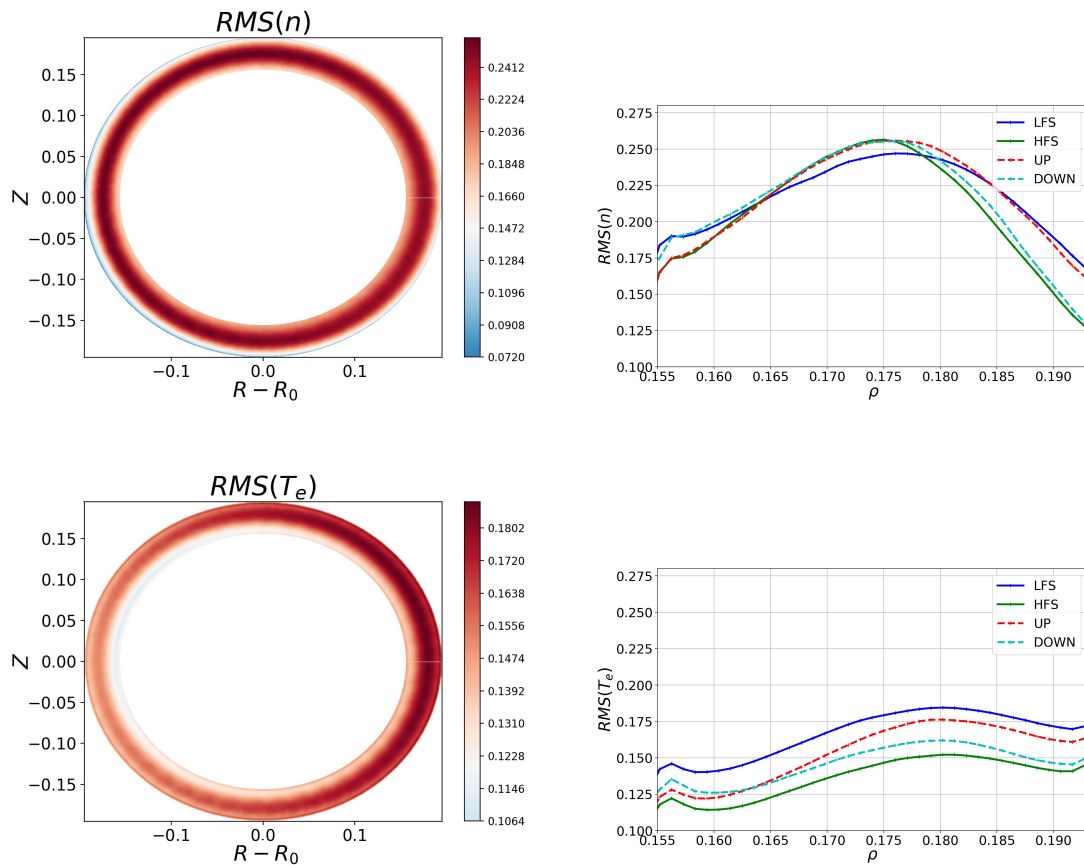


Figure 4.3.5: Fluctuation level $RMS(n)$, $RMS(T_e)$ in circular geometry.

The ballooning is not pronounced due to the strong rotation of the plasma introducing other instabilities, e.g. Kelvin-Helmholtz and interchange, see the discussion in section 3.3.2. If the rotation velocity is decreased artificially in simulations by reducing the $E \times B$ -velocity, a clear ballooning with a relative stable HFS and less stable LFS with very high fluctuations on LFS is present.

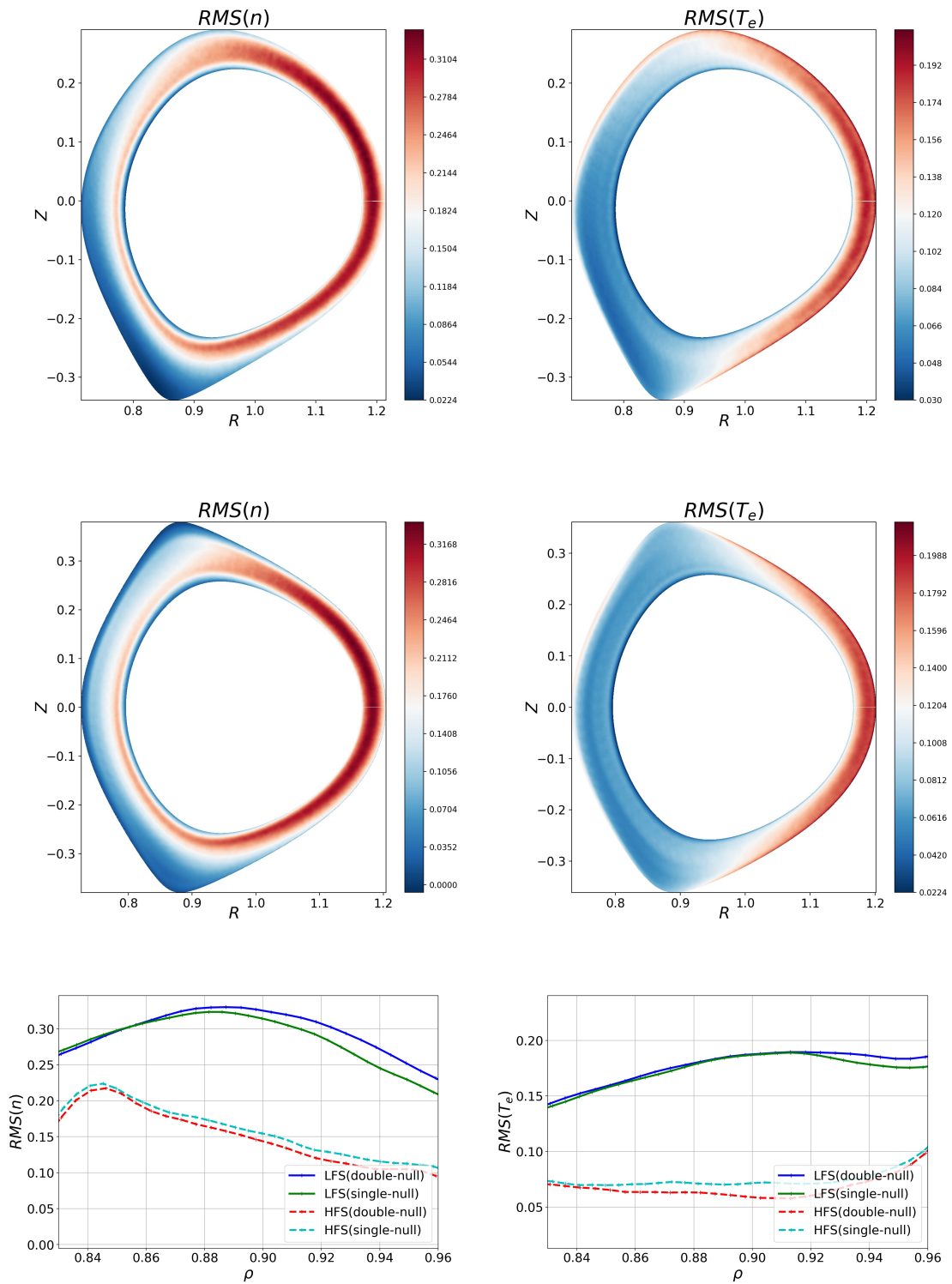


Figure 4.3.6: Fluctuation level $RMS(n)$, $RMS(T_e)$ in single-null and double-null geometry. Comparison between LFS and HFS.

The fluctuation levels in SN and DN are shown in figure 4.3.6. First, there is no big difference between SN and DN in the fluctuation levels. The maximum value for the density fluctuations is around $RMS(n)_{max} \approx 0.32$ on the LFS. The difference between LFS and HFS is more pronounced, indicating a more stable HFS in SN and DN compared to LFS. The flux expansion on HFS might also play a role. The density fluctuations are in the same range in SN and DN compared to the circular geometry on the HFS. The electron temperature fluctuations are decreased on HFS.

TRANSPORT The radial particle transport $\Gamma_n = \langle n \mathbf{v}_{E \times B}^{\rho} \rangle_{\varphi, t}$ and the heat transport $\Gamma_p = \langle p_e \mathbf{v}_{E \times B}^{\rho} \rangle_{\varphi, t}$ across the flux surfaces is calculated in all three geometries. The particle transport is shown in figure 4.3.7 for $t = 47.0$. It is dominated by streamers. Towards the top/bottom in SN and DN the structures are tilted.

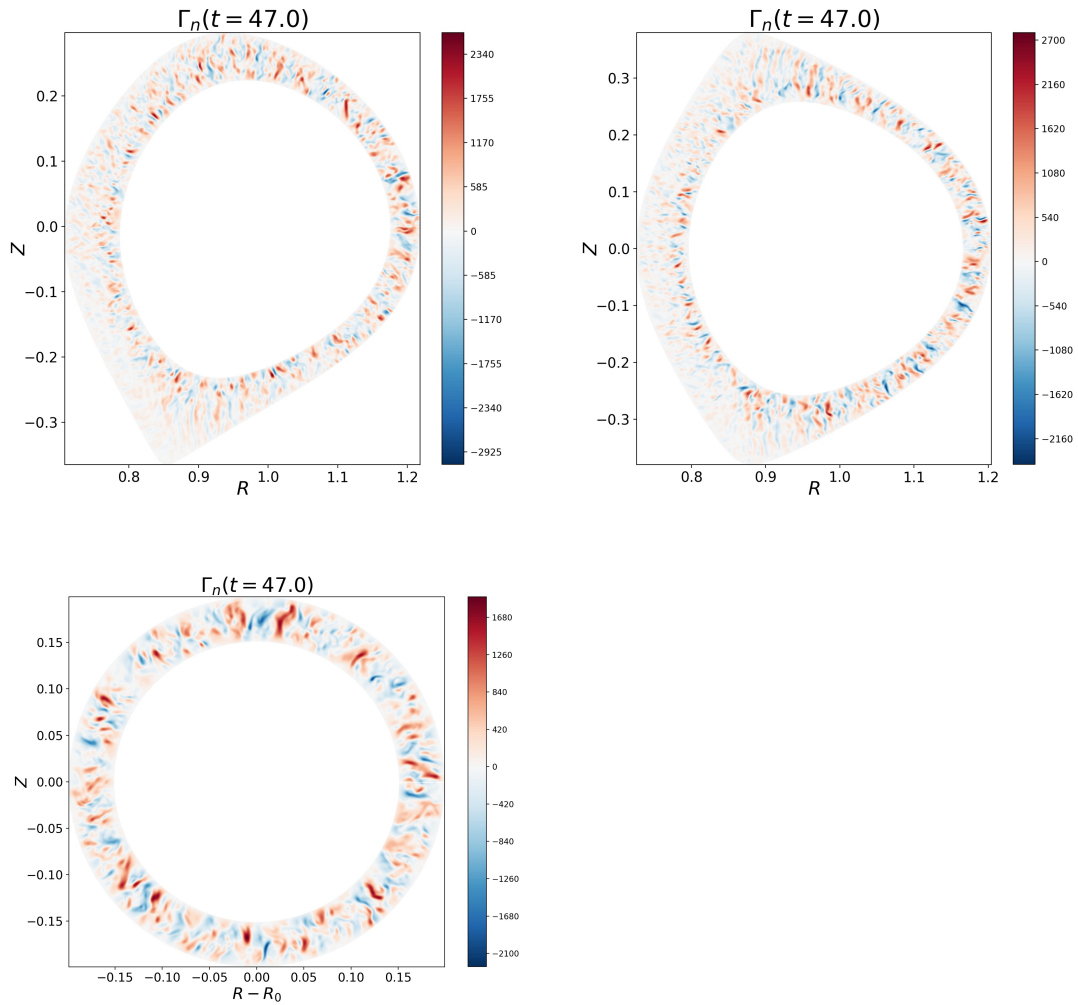


Figure 4.3.7: Radial transport Γ_n snapshot in a saturated turbulence regime for $t = 47.0$ in all three geometries. A mode structure is clearly visible.

It is obvious that the transport has a structure with different k -modes. As all quantities, the radial density and heat transport also rotates clockwise. A rotating mode is difficult in terms of data analysis, as will be discussed below.

We are interested in the smooth global average $\langle \cdot \rangle_{\varphi, t}$. However the average of a running (rotating) mode always shows again a mode structure, as is shown in figure 4.3.8 with the help of a toy-model. A running sine wave in 1D $f(x, v, t) = 3.0 + \sin(vt + x)$ with the constant velocity $v = 0.1$ and $x \in [0, 2\pi]$ is used. The average $\langle f(x) \rangle_t = \frac{1}{N_s} \sum_t^{N_s} f(x, v, t)$ with $N_s = 2000$ is shown in the right plot. It poses again a mode structure with a

smaller amplitude. The amplitude approaches asymptotically towards the background value 3.0 with higher number of average snapshots N_s , which is shown in the same plot, where the maximum amplitude of the average value $\max(\langle f(x) \rangle)$ is plotted for $N_s \in [10, \dots, 150]$. An exponential fit indicates the asymptotic approach to the background.

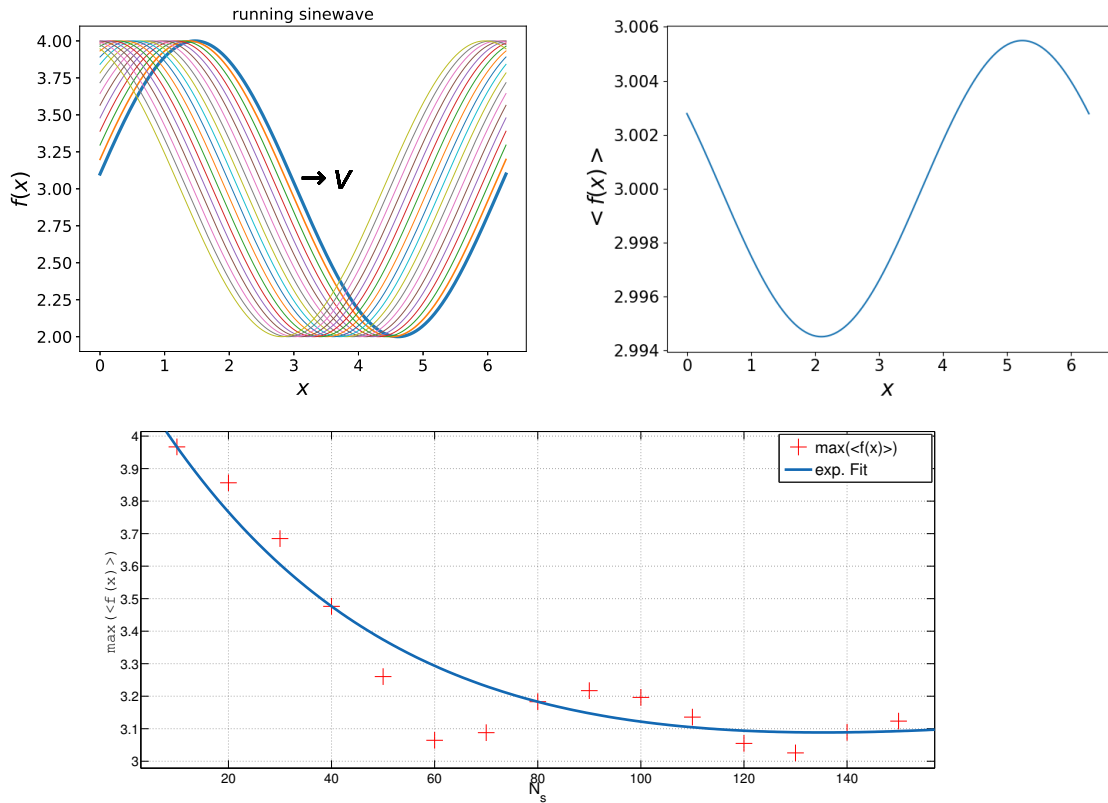


Figure 4.3.8: Toy-model for the explanation of the data analysis issue. The average of a running mode is again a mode. The amplitude of the average $\max(\langle f(x) \rangle)$ approaches asymptotically the background value with higher number of snapshots N_s .

This clearly shows the issues one encounters for the calculation of the average transport. The average background value is hidden behind the residue of a mode structure. As is shown in figure 4.3.9, the behavior of the maximum value of the density transport $\max(\langle \Gamma_n \rangle_{\varphi,t})$ is very similar to that in the 1D example in figure 4.3.8. The maximum value of the transport approaches asymptotically a background value, meaning that the mode, which is present in the average transport, is a residue. A large amount of data is needed for the average procedure, in order to decrease the amplitude of the mode and make the global structure visible. In order to decrease the computational

time, a filter has been applied. The average transport (density and heat) was Fourier transformed along the flux surfaces in poloidal direction. In the Fourier space higher k -modes were set to zero. The rest of the modes were transformed back in order to get the final smooth transport. This makes a qualitative comparison of the geometries possible. The same amount of data in all three geometries was used for the average and the same filter was applied.

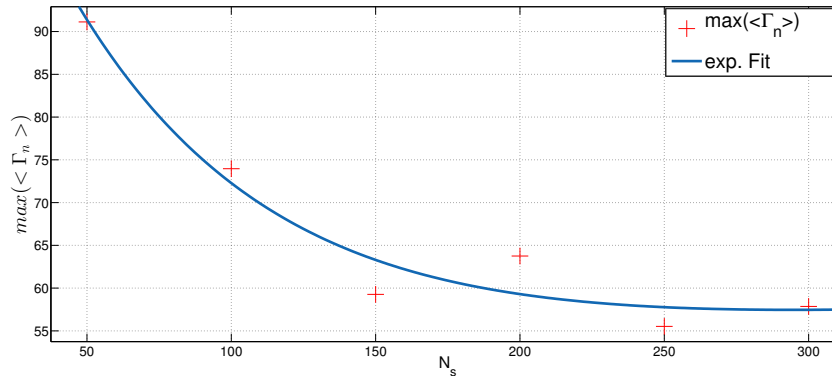


Figure 4.3.9: red: Maximum value of the particle transport $\max(\langle \Gamma_n \rangle)$ averaged over number of snapshots N_s in GRILLIX. blue: exponential fit

The result for the density transport is shown in figure 4.3.10 for the circular geometry. The transport is higher at the LFS compared to the HFS. A pronounced up-down asymmetry is visible. The transport is highest in the upper right quarter. The rotation of the plasma is responsible for this asymmetry. A pure ballooning would cause an up-down symmetric transport, which was observed with artificially decreased $E \times B$ -rotation. However with clockwise rotation, the plasma rotates from the less stable LFS, where the radial transport is enhanced, into the lower side direction. There effectively less plasma arrives, which could be transported outwards. The plasma is stabilized at the HFS, where the radial transport is decreased. Leaving the HFS, the plasma is transported strongly outwards in the upper right quarter.

The situation is similar in SN and DN, see figure 4.3.11. The density transport in DN is slightly higher on the LFS compared to SN. It is equivalent into the direction of the X-point and on the HFS in both geometries. The transport is maximum on LFS, which is in line with the circular geometry. Effectively the DN geometry seems to be less stable on the LFS. Compared to the circular case, the SN and DN geometries show a higher density transport on the LFS and a decreased transport on HFS. It seems that the plasma, which is

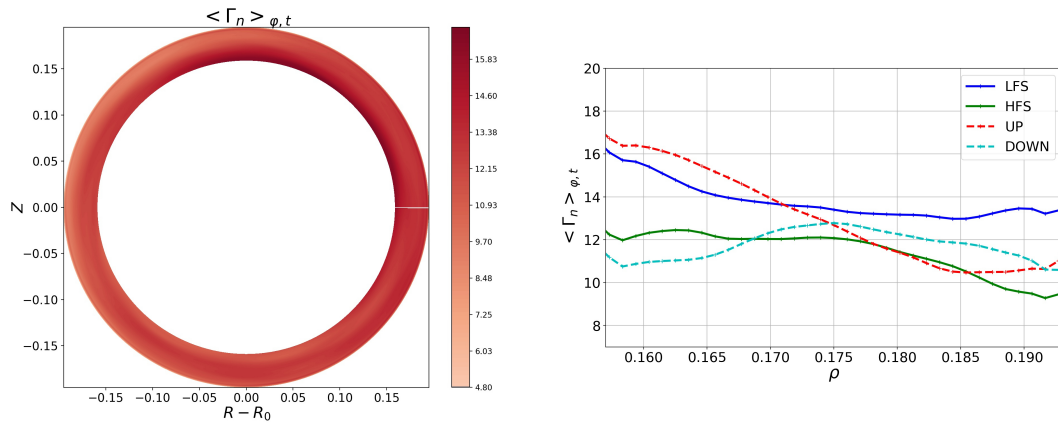


Figure 4.3.10: left: Filtered average radial density transport $\langle \Gamma_n \rangle_{\varphi,t}$ in circular geometry. right: Radial transport at HFS, LFS, upper side (UP), lower side (DOWN)

stabilized on the HFS, due to the presence of the stretched flux surfaces in the vicinity of the X-point, is transported more strongly on the LFS.

The heat transport is shown in figure 4.3.12 and 4.3.13. It is in line with the particle transport. In circular geometry the same asymmetries are observed. The HFS in SN and DN is in the same range like the circular geometry. However the heat transport on the LFS is a factor two higher in SN and DN. The plasma which is stabilized on the HFS (lower fluctuation levels in density and electron temperature and lower density transport), due to the stretched region, rotates into LFS, where it is more strongly transported outwards. Thus a bigger imbalance between LFS and HFS in heat and density transport is observed. in the SN and DN cases.

Open questions still remain. The plasma rotation has a strong impact on the dynamics. In circular geometry it destabilizes the HFS leading to comparable fluctuations on all sides and also causes the difference in transport on LFS and HFS to be relatively weak. In SN and DN the rotation causes an increased density and heat transport on LFS. The origin of the rotation in the global electromagnetic model needs to be clarified. In [31] a force balance between the curvature terms was suggested leading to $\mathbf{v}_{E \times B} \simeq \mathbf{v}_{De}$. Another open question is the impact of the sheared rotation. Although the q -profile was chosen in the circular geometry in order to match SN and DN closely, the profile of the poloidal rotation velocity is different, showing steeper gradients and different shape. Sheared flows are able to decrease particle and heat transport, as was shown in the review article [125]. The circular geometry shows effectively a smaller density and heat transport outwards compared

to SN and DN. One reason is that the rotation itself pushing the plasma, which is stabilized by the stretched region around the X-point in SN and DN, from the HFS to LFS. Another reason may be the sheared poloidal flow decreasing the turbulent transport, which of course needs further studies. The X-point disconnects the HFS and LFS in SN and DN. After the X-point the particle and heat transport approaches a lower constant value on HFS in SN and DN. In SN it starts to increase again on the top side, whereas it remains on the low value in DN. The second X-point decreases the transport on the top side in the vicinity. In the circular geometry, where no X-point is present, no such behavior can be observed.

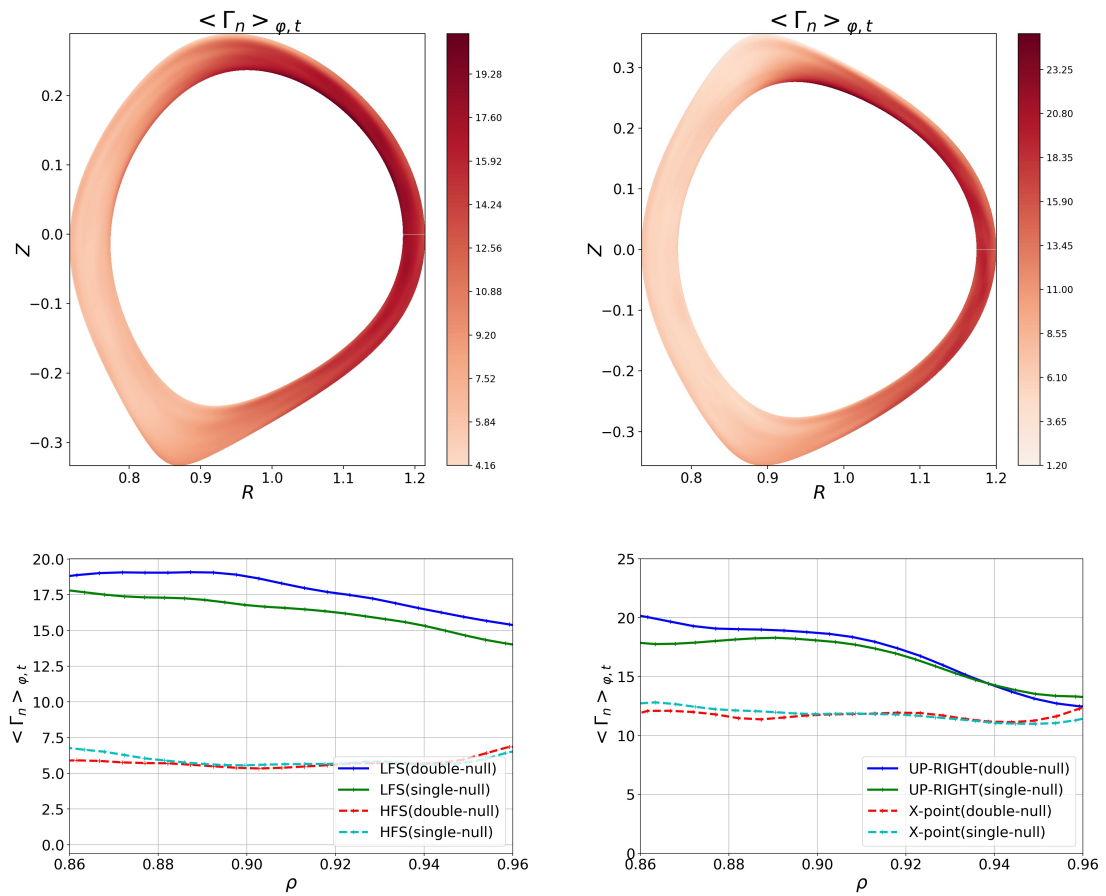


Figure 4.3.11: Filtered average radial density transport $\langle \Gamma_n \rangle_{\varphi,t}$ in single-null and double-null geometries.

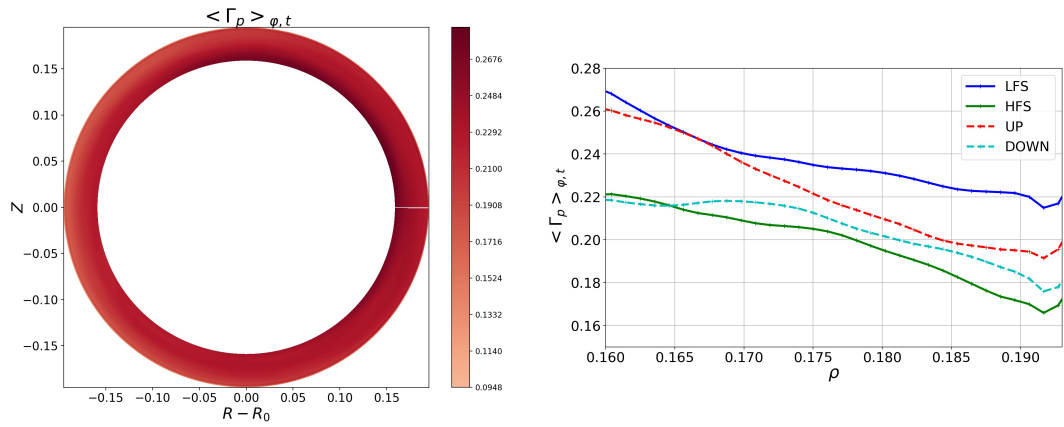


Figure 4.3.12: left: Average radial heat transport $\langle \Gamma_p \rangle_{\varphi,t}$ in circular geometry. right: Radial transport at HFS, LFS, upper side (UP), lower side (DOWN)

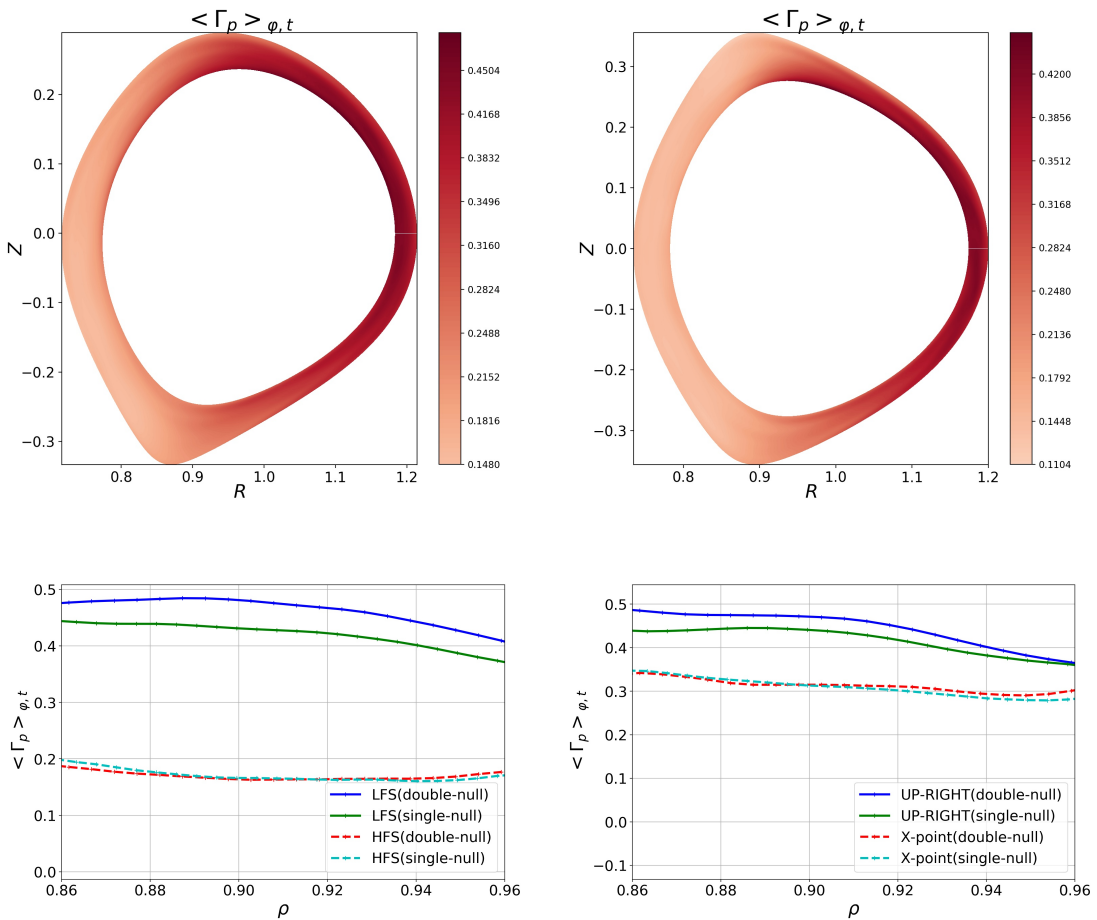


Figure 4.3.13: Filtered average radial heat transport $\langle \Gamma_p \rangle_{\varphi,t}$ in single-null and double-null geometries.

Summary

In this chapter the FCI concept was applied in a circular, single-null and double-null geometries with similar q -profiles. The aim was the comparison of the geometries in terms of the profiles, fluctuation levels, particle and heat transport. The separatrix could not be crossed, due to the lack of boundary conditions. However the impact of the X-point was investigated, because the closed flux surfaces are stretched towards the X-point. The simulations showed a strong $E \times B$ -rotation of the plasma, which had interesting implications. In circular geometry the profiles were slightly steeper on the HFS and an up-down asymmetry was present. The fluctuation levels were on all sides very similar. Also the difference in density and heat transport between HFS and LFS was not very pronounced. The rotation equilibrated the turbulence strength across the flux surfaces in circular geometry. The situation was different in single-null and double-null geometries. The stretched flux surface region stabilized the HFS in both geometries. The profiles were steeper on HFS compared to LFS. Also the fluctuation levels on the HFS were lower, but at the same time higher on LFS compared to the circular geometry. The rotation of the plasma pushed the more stable and dense plasma from the HFS towards LFS, leading to an enhanced density and heat transport. Consequently, stabilizing the HFS by a stretched flux surface region in the vicinity of the X-point, destabilized the LFS. This effect is stronger in the presence of a second stretched region. Further studies are needed in order to answer questions concerning the origin of the poloidal rotation within the global electromagnetic model. Furthermore the impact of the sheared poloidal flow on turbulence dynamics needs to be investigated.

SUMMARY, CONCLUSIONS AND OUTLOOK

The GRILLIX project aims to develop a numerical code which can simulate and predict anomalous transport in the scrape-off layer of fusion devices. The singularity of field-aligned coordinate systems at the separatrix motivated a flux-coordinate independent approach, which is able to treat the X-point and other complicated magnetic topologies such as snowflake divertor.

The numerical methods for the flux-coordinate independent approach in GRILLIX were initially developed with a relatively simple fluid-turbulence model (Hasegawa-Wakatani), which is not accurate in the edge and SOL region. The importance of the SOL for a successful fusion reactor and the complicated physics there made the implementation of a more advanced model in GRILLIX essential. The focus was on the consistent and correct implementation of the global electromagnetic model in GRILLIX. Significant achievements of this thesis included the relaxation of the Boussinesq approximation, good conservation properties on the discrete level and the extension to electromagnetic dynamics. By improving the accuracy of the GRILLIX code, the simulations could be compared directly to and verified against the experiment. This is an important step towards the goal of a virtual tokamak, where numerical simulations can be used both to self-consistently interpret and even predict the behavior of fusion experiments. At the end of the thesis a reliable, verified and validated model poses a solid foundation for further extensions of GRILLIX.

5.1 SUMMARY AND CONCLUSIONS

In chapter 2 the theoretical foundation of the new plasma model in GRILLIX is developed from the foundation of the Braginskii equations. A series of simplifications are made to the system of plasma-fluid equations to reduce the computational cost and make them suitable for numerical implementation. Only slower drift dynamics is kept in the system. The Boussinesq approximation is discussed in depth, and in particular how it breaks energy-conservation

if applied in a non-conservative way. This is incompatible with the use of a global electrodynamic model and as such the Boussinesq approximation was relaxed in the model. In particular the treatment of the terms without the Boussinesq approximation was by far more complex. The use of staggered grids and a multigrid solver were needed. All equations were shown in a systematic discretized way. The simple slab geometry reduced the complexity and enabled the transition to more complex geometries. The method of manufactured solutions successfully verified GRILLIX and indicated the correct numerical implementation.

In chapter 3 the model was initially tested for the case of plasma blobs, which are high-amplitude events in the SOL. Blobs benefit from being able to be treated relatively simply analytically, and as such allow for comparison between theory and numerical implementation in GRILLIX. By deriving and comparing analytical expressions for blob dynamics against the results of a simulation, it is shown that the new model in GRILLIX is able to successfully simulate blobs across the range of turbulence-relevant plasma parameters. The blob case also allowed for testing of the novel features of the model, particularly the removal of the Boussinesq approximation and temperature dependent sheath boundary conditions. It was found that the effect of the Boussinesq approximation was strongly dependent on the plasma-parameters and the blob regime.

The experiences with an electrostatic model showed a heavy limitation of the time step, due to fast collisional dissipation processes, which finally motivated the extension of GRILLIX to an electromagnetic model. Analytical predictions were used in order to test the Alfvén dynamics and the Helmholtz multigrid solver. The very good agreement of GRILLIX results with the analytical predictions showed that the Helmholtz solver performs well and that the electromagnetic dynamics are treated correctly.

The new model was then used to study turbulence in slab geometry. Periodic slab geometry was used to verify energy and particle conservation in GRILLIX and to compare to the case where conservation was broken through the use of the Boussinesq approximation. It was seen that breaking the conservation properties typically led to very strong poloidal flows, which either crashed the simulation or gave unphysical results for turbulence suppression.

The tested and verified global electromagnetic model was applied on the Large Plasma Device (LAPD), a linear pulsed cathode-source device which could be modeled in slab geometry. The LAPD modeling efforts from other works, which used the non-conservative Boussinesq approximation and an electrostatic model, were taken one step further. By running simulations

at parameters which matched experimental conditions, it was possible to validate the simulation results through direct comparison to the experimental result. Comparison of profiles, turbulent fluctuation levels, the power spectrum and skewness all showed reasonable agreement, suggesting that the simulation was accurately reflecting the dominant physical dynamics of the experiment. Observed deviations appear to originate due to the omission of neutral dynamics in GRILLIX, and due to experimental uncertainties which make direct comparisons difficult. The effect of switching back on the Boussinesq approximation for the comparison between model results and experimental data was minor for cases with shallow gradients, but gave significant deviation for cases with steep gradients.

Finally the tested, verified and validated global electromagnetic model was used in the full three-dimensional tokamak geometry in chapter 4. The investigations were performed on the closed-field-line region, since the treatment of sheath boundary conditions in FCI remains an open research question. Nevertheless, the effect of the X-point could be studied due to the elongation of flux surfaces in the surrounding region. Profiles, fluctuation levels and turbulent transport levels were compared between single-null, double-null and circular geometries. It was found that the inclusion of elongated regions stabilized the high-field side (HFS) of the torus, leading to steeper gradients and lower transport, while simultaneously the low-field side (LFS) was destabilized compared to circular geometry. The stretched region enhances the transport imbalance and damps fluctuations on the HFS. The more stable plasma on HFS rotates into LFS, where it is transported strongly outwards. Additionally, the single-null and double-null geometries were found to have reduced shear of the poloidal flow which is known to strongly affect turbulent dynamics.

5.2 OUTLOOK

Having established and implemented the global electromagnetic model in GRILLIX, the extension of the model to diverted geometries is the next research goal of the GRILLIX project. In particular the implementation of the parallel boundary conditions poses a major challenge within FCI. The reason for this is the location of the parallel boundary e.g. divertor plates. It lies neither on the magnetic field line nor on the grid. The subtle points regarding the implementation of the parallel boundary conditions are listed in [46]. Consequently the implementation of the sheath-boundary conditions within the FCI approach was beyond the scope of this thesis. First steps were done in the GRILLIX group by A. Stegmeir and T. Body, using the

volume penalization method [126] in collaboration with the GBD group [127]. Promising results are shown in figure 5.2.1.

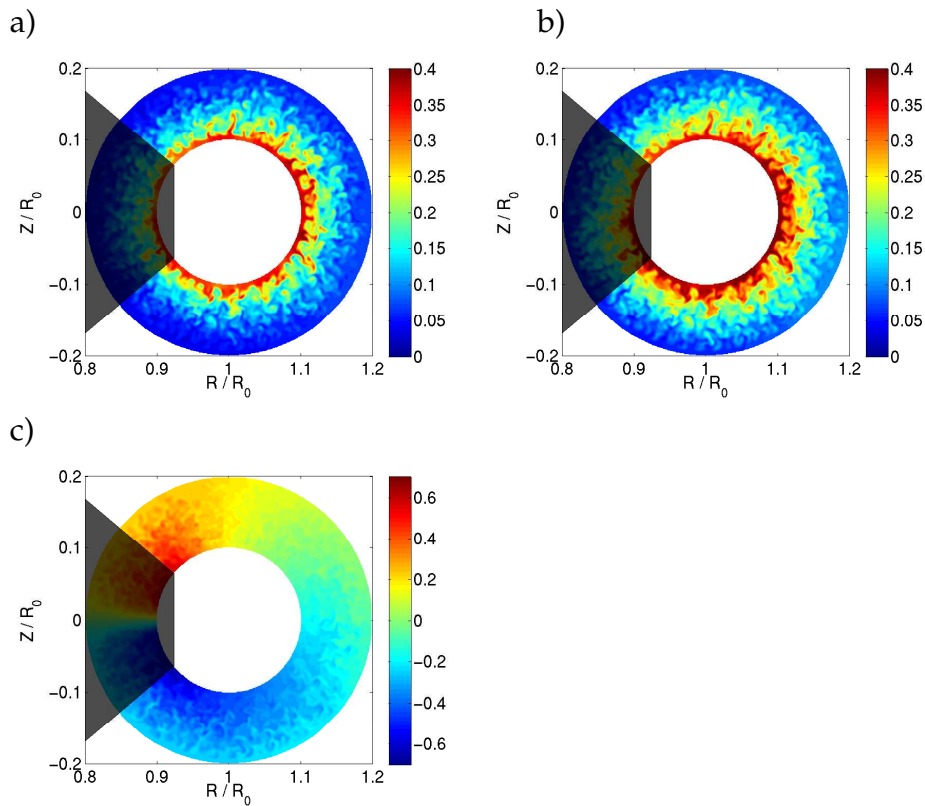


Figure 5.2.1: Penalization method applied to FCI for limited circular geometry. a) density b) electron temperature c) parallel ion velocity. Grey area poses the limiter.

The boundary conditions will allow the transition across the separatrix and finally the simulation of the X-point. This work has already been started. Moreover, once the parallel boundary conditions are implemented, GRILLIX can be extended to non-axisymmetric geometries e.g. stellarator.

On the model side, there is also room for further extensions. The dynamics of the neutrals plays a crucial role in the SOL. Phenomena like recycling and detachment can only be studied if the model will be extended to incorporate with neutrals. This project is also currently under active development, testing a fluid neutrals model in LAPD geometry. The linear device can also facilitate the transition from postdiction to prediction. For this a collaboration with the experimental side has to be established.

Furthermore, the cold ion assumption also needs to be relaxed. Therefore two paths are possible. One can implement the ion temperature equation from the

Braginskii system, or a gyro-fluid model might even be better suited for this task. Also on the electromagnetic model side, there is room for improvement. The Alfvén dynamics had a big impact on the simulations, however the transport is still electrostatic. The inclusion of magnetic flutter in the model will provide a more complete picture of plasma transport. Connected with that, the FCI approach can be applied to a temporally varying magnetic field lines, finally simulating a self-consistently developing magnetic equilibrium. For such sophisticated simulations better computational performance is desired. The constraint of using only a single MPI process per poloidal plane needs to be relaxed. In terms of performance, the use of a more advanced time stepping scheme e.g. super time step may be needed and has to be tested.

5.3 CONCLUSION

The use of simulation as a tool to both interpret and also predict experimental results is a significant challenge. It requires the derivation and implementation of a physically accurate plasma model, the treatment of the derived equations in a consistent and numerically stable method, and the numerical solution of the equations in a reasonable time on modern supercomputers. Consequently, the path to a virtual plasma is a long one and a lot of work is still needed. At the same time, all of the mentioned challenges are solvable within FCI. The global electromagnetic model significantly improves the physical accuracy of the GRILLIX code, providing an important step on the path to a virtual tokamak with *reliable, validated* and *predictive* capabilities.

BIBLIOGRAPHY

- [1] Y. Xu *Matter Rad. Extreme.*, vol. 1, pp. 192–200, 2016.
- [2] <https://quasaricsolutions.com/blog/2016/1/22/understanding-heat-dissipation-in-magnetic-confinement-fusion>.
- [3] A. C. C. Sips *et al. Plasma Phys. Control. Fusion*, vol. 47, pp. A19–A40, 2005.
- [4] <http://www.ruceni.info/2018/tokamak-technology-is-related-to.html>.
- [5] U. Stroth, *Plasmaphysik Phaenomene, Grundlagen und Anwendungen*. Springer Spektrum, 2018.
- [6] A. H. Boozer *Phys. of Plasmas*, vol. 19, p. 058101, 2012.
- [7] F. Wagner, G. Becker, K. Behringer, *et al. Phys. Rev. Lett.*, vol. 49, p. 1408, 1982.
- [8] P. Stangeby, *The Plasma Boundary of Magnetic Fusion Devices*. Institute of Physics Publishing, 2000.
- [9] A. Stegmeir, *GRILLIX: A 3D turbulence code for magnetic fusion devices bason on a field line map*. dissertation, Technische Universitaet Muenchen, 2015.
- [10] W. Fundamenski, *Power Exhaust in Fusion Plasmas*. Cambridge University Press, 2010.
- [11] A. J. Wootton, B. A. Carreras, H. Matsumoto, *et al. Phys. Fluids*, vol. 2, p. 2879, 1990.
- [12] J. Horacek, R. A. Pitts, J. Adamek, *et al. Plasma Phys. Control. Fusion*, vol. 58, p. 074005, 2016.
- [13] T. Eich, B. Sieglin, A. Scarabosio, *et al. Phys. Rev. Lett.*, vol. 107, p. 215001, 2011.
- [14] T. Eich, A. W. Leonard, R. A. Pitts, *et al. Nucl. Fusion*, vol. 53, p. 093031, 2013.

- [15] F. D. Halpern, J. Horacek, R. A. Pitts, *et al.* *Plasma Phys. Control. Fusion*, vol. 58, p. 084003, 2016.
- [16] G. Federici, R. Kemp, D. Ward, *et al.* *Fusion Eng. Des.*, vol. 89, p. 882889, 2014.
- [17] F. Nespoli, *Scrape-Off Layer physics in limited plasmas in TCV*. dissertation, Ecole Polytechnique Federale de Lausanne, 2017.
- [18] A. Loarte, B. L. Lipschultz, A. S. Kukushkin, *et al.* *Nucl. Fusion*, vol. 47, p. 203263, 2007.
- [19] A. W. Leonard *Plasma Phys. Control. Fusion*, vol. 60, p. 044001, 2018.
- [20] R. H. Cohen, N. Mattor, and X. Xu *Contrib. Plasma Phys.*, vol. 34, pp. 232–246, 1994.
- [21] P. Ricci, F. D. Halpern, S. Jolliet, *et al.* *Plasma Phys. Control. Fusion*, vol. 54, p. 124047, 2012.
- [22] A. Masetto, F. D. Halpern, S. Jolliet, *et al.* *Phys. Plasmas*, vol. 20, p. 092308, 2013.
- [23] P. Ricci and B. Rogers *Phys. Plasmas*, vol. 20, p. 010702, 2013.
- [24] B. Rogers and P. Ricci *Phys. Rev. Lett.*, vol. 104, p. 225002, 2010.
- [25] B. D. Dudson, M. Umansky, X. Xu, *et al.* *Comput. Phys. Commun.*, vol. 180, p. 1467, 2009.
- [26] T. Xia, X. Xu, and P. Xi *Nucl. Fusion*, vol. 53, p. 073009, 2013.
- [27] T. Xia, X. Xu, and P. Xi *Nucl. Fusion*, vol. 55, p. 113030, 2015.
- [28] B. D. Dudson and J. Leddy *Plasma Phys. Control. Fusion*, vol. 59, p. 054010, 2017.
- [29] P. Tamain, H. Bufferand, G. Ciraolo, *et al.* *J. Comput. Phys.*, vol. 321, p. 606, 2016.
- [30] C. Baudoin, P. Tamain, H. Bufferand, *et al.* *Contrib. Plasma Phys.*, vol. 0, p. 00168, 2018.
- [31] B. Zhu, M. Francisquez, and B. N. Rogers *Phys. Plasmas*, vol. 24, p. 055903, 2017.

-
- [32] W. D. Dhaeseleer, W. N. G. Hitchon, J. D. Callen, *et al.*, *Flux Coordinates and Magnetic Field Structure*. Springer, 1990.
- [33] F. Jeffrey, *Ideal Magnetohydrodynamics*. Plenum Press, 1987.
- [34] V. D. Shafranov *Rev. Plasma Phys.*, vol. 2, p. 103, 1966.
- [35] H. Grad and H. Rubin *Proceedings of the 2nd UN Conf. on the Peaceful Uses of Atomic Energy*, vol. 31, p. 190, 1958.
- [36] S. Hamada *Nucl. Fusion*, vol. 2, p. 23, 1962.
- [37] A. H. Boozer *Phys. Fluids*, vol. 24, p. 1999, 1981.
- [38] P. Paruta, P. Ricci, C. Wersal, *et al.* submitted, 2018.
- [39] B. Lipschultz, B. LaBombard, E. S. Marmor, *et al.* *Nucl. Fusion*, vol. 24, p. 977, 1984.
- [40] A. Hatayama, H. Segawa, R. Schneider, *et al.* *Nucl. Fusion*, vol. 40, p. 2009, 2000.
- [41] A. Stegmeir, D. Coster, O. Maj, *et al.* *Comp. Phys. Commun.*, vol. 198, pp. 139–153, 2016.
- [42] A. Stegmeir, D. Coster, O. Maj, *et al.* *Comput. Phys. Commun.*, vol. 198, p. 139, 2016.
- [43] F. Hariri and M. Ottaviani *Comput. Phys. Commun.*, vol. 184, p. 2419, 2013.
- [44] A. Stegmeir, D. Coster, A. Ross, *et al.* *Plasma Phys. Control. Fusion*, vol. 60, p. 035005, 2018.
- [45] A. Stegmeir, O. Maj, D. Coster, *et al.* *Comput. Phys. Commun.*, vol. 213, pp. 111–121, 2017.
- [46] A. Stegmeir, *GRILLIX Documentation*. 2018.
- [47] B. W. Shanahan, P. Hill, and B. D.udson *J. Phys.: Conf. Ser.*, vol. 775, p. 012012, 2016.
- [48] A. Hasegawa and M. Wakatani *Phys. Rev. Lett.*, vol. 50, p. 682, 1983.
- [49] A. Stegmeir, D. Coster, O. Maj, *et al.* *Poster presented at 26th IAEA Fusion Energy Conference (FEC 2016), Kyoto, 2016.*

- [50] S. J. Zweben, W. M. Davis, S. M. Kaye, *et al.* *Nucl. Fusion*, vol. 55, p. 093035, 2016.
- [51] W. Fundamenski *Plasma Phys. Control. Fusion*, vol. 47, p. R163, 2005.
- [52] B. Scott, *Low Frequency Fluid Drift Turbulence in Magnetised Plasmas*. habilitation, Heinrich-Heine-Universitaet, 2000.
- [53] A. Zeiler, J. F. Drake, and B. Rogers *Phys. Plasmas*, vol. 4, p. 2134, 1997.
- [54] S. I. Braginskii *Rev. Plasma Phys.*, vol. 1, 1965.
- [55] D. D. Gray and A. Giorgini *J. Heat Mass Transfer*, vol. 19, p. 545, 1976.
- [56] G. Schmidt, *Physics of High Temperature Plasmas*. Academic Press, 1979.
- [57] F. Jenko, D. Told, T. Görler, *et al.* *Nucl. Fusion*, vol. 53, p. 073003, 2013.
- [58] W. Wan, S. E. Parker, Y. Chen, *et al.* *Phys. Rev. Lett.*, vol. 109, p. 185004, 2012.
- [59] Z. Menglong, *Towards a More Complete Description of Tokamak Edge Plasmas: SOLPS Simulations with Kinetic Electron Effects*. dissertation, Technische Universitaet Muenchen, 2018.
- [60] A. V. Chankin and D. P. Coster *J. Nucl. Mater.*, vol. 463, p. 498, 2015.
- [61] J. Loizu, *The role of the sheath in magnetized plasma turbulence and flows*. dissertation, Ecole Polytechnique federale de Laussane, 2013.
- [62] P. C. Stangeby *Phys. of Plasmas*, vol. 2, p. 702, 1995.
- [63] F. Nespoli, I. Furno, B. Halpern, B. Labit, *et al.* *Nucl. Mater. Energy*, vol. 12, pp. 1205–1208, 2017.
- [64] N. R. Walkden, L. Easy, F. Militello, *et al.* *Plasma Phys. Control. Fusion*, vol. 58, p. 115010, 2016.
- [65] W. H. Press, *Numerical Recipes*. Cambridge University Press, 2007.
- [66] A. Arakawa *J. Comput. Phys.*, vol. 135, p. 103, 1997.
- [67] G. Karniadakis, M. Israeli, J. Orszag, *et al.* *J. Comput. Phys.*, vol. 97, p. 414, 1991.
- [68] A. Meister, *Numerik linearer Gleichungssysteme*. Vieweg und Teubner, 2011.

-
- [69] U. Trottenberg, W. C. Oosterlee, and A. Schuller, *Multigrid: Basics, Parallelism and Adaptivity*. Academic Press, 2000.
- [70] J. H. Bramble, *Multigrid Methods*. Longman, 1993.
- [71] W. Hackabus, *Multi-Grid Methods and Applications*. Springer-Verlag, 1980.
- [72] R. C. J. Oberkampf, W J, *Verification and Validation in Scientific Computing*. Cambridge University Press, 2010.
- [73] R. Riva, P. Ricci, F. D. Halpern, *et al. Phys. Plasmas*, vol. 21, p. 062301, 2014.
- [74] B. D. Dudson, J. Madsen, J. Omotani, *et al. Phys. Plasmas*, vol. 23, p. 062303, 2016.
- [75] A. Ross, A. Stegmeir, and D. Coster *Contrib. Plasma. Phys.*, vol. 0, pp. 1–6, 2018.
- [76] G. Y. Antar, S. I. Krasheninnikov, P. Devynck, *et al. Phys. Rev. Lett.*, vol. 87, p. 065001, 2001.
- [77] G. Y. Antar, G. Counsell, Y. Yu, *et al. Phys. Plasmas*, vol. 10, p. 419, 2003.
- [78] B. D. Dudson, N. Ben Ayed, A. Kirk, *et al. Plasma Phys. Control. Fusion*, vol. 50, p. 124012, 2008.
- [79] M. Endler, H. Niedermeyer, L. Giannone, *et al. Nucl. Fusion*, vol. 35, p. 1307, 1995.
- [80] A. J. Thornton, G. Fishpool, and A. Kirk *Plasma Phys. Control. Fusion*, vol. 57, p. 115010, 2015.
- [81] B. LaBombard, R. L. Boivin, M. Greenwald, *et al. Phys. Plasmas*, vol. 8, p. 2107, 2001.
- [82] N. Vianello, V. Naulin, R. Schrittwieser, *et al. Phys. Rev. Lett.*, vol. 106, p. 125002, 2011.
- [83] D. A. Russell, J. R. Myra, *et al. Phys. Plasmas*, vol. 16, p. 122304, 2009.
- [84] S. I. Krasheninnikov, D. A. Dippolito, and J. R. Myra *J. Plasma Physics*, vol. 74, pp. 679–717, 2008.

- [85] D. A. DiIppolito, J. R. Myra, and S. J. Zweben *Phys. Plasmas*, vol. 18, p. 060501, 2011.
- [86] O. E. Garcia *Plasma Fusion Res.*, vol. 4, p. 019, 2009.
- [87] S. I. Krasheninnikov *Phys. Lett.*, vol. 283, p. 368, 2001.
- [88] O. E. Garcia, N. H. Bian, and W. Fundamenski *Phys. Plasmas*, vol. 13, p. 082309, 2006.
- [89] J. Omotani, F. Militello, L. Easy, *et al.* *Plasma Phys. Control. Fusion*, vol. 58, p. 014030, 2015.
- [90] C. Theiler, I. Furno, P. Ricci, *et al.* *Phys. Rev. Lett.*, vol. 103, p. 065001, 2009.
- [91] O. E. Garcia, V. Naulin, A. H. Nielsen, *et al.* *Phys. Rev. Lett.*, vol. 92, p. 165003, 2004.
- [92] D. A. Russell, J. R. Myra, and D. A. DiIppolito *Phys. Plasmas*, vol. 16, p. 122304, 2009.
- [93] A. Stegmeir, D. Coster, A. Ross, *et al.* *43rd EPS Conference on Plasma Physics, Leuven*.
- [94] F. Militello, W. Fundamenski, V. Naulin, *et al.* *Plasma Phys. Control. Fusion*, vol. 54, p. 095011, 2012.
- [95] F. Militello, V. Naulin, and A. H. Nielsen *Plasma Phys. Control. Fusion*, vol. 55, p. 074010, 2013.
- [96] J. R. Angus, M. V. Umansky, and S. I. Krasheninnikov *Phys. Rev. Lett.*, vol. 108, p. 215002, 2012.
- [97] J. R. Angus, S. I. Krasheninnikov, and M. V. Umansky *Phys. Plasmas*, vol. 19, p. 082312, 2012.
- [98] F. Easy, L. Militello, J. Omotani, N. R. Walkden, *et al.* *Phys. Plasmas*, vol. 23, p. 012512, 2016.
- [99] N. R. Walkden, B. D. Dudson, and G. Fishpool *Plasma Phys. Control. Fusion*, vol. 55, p. 105005, 2013.
- [100] N. R. Walkden, B. D. Dudson, L. Easy, *et al.* *Nucl. Fusion*, vol. 55, p. 113022, 2015.

-
- [101] P. Ricci, F. Riva, C. Theiler, *et al.* *Phys. Plasmas*, vol. 22, p. 055704, 2015.
- [102] P. Tamain, H. Bufferand, G. Ciraolo, *et al.* *Contrib. Plasma. Phys.*, vol. 54, p. 555, 2014.
- [103] L. Easy, F. Militello, J. Omotani, B. Dudson, *et al.* *Phys. Plasmas*, vol. 21, p. 122515, 2014.
- [104] L. Easy, F. Militello, J. Omotani, *et al.* *Phys. Plasmas*, vol. 23, p. 012512, 2016.
- [105] F. Militello, N. R. Walkden, T. Farley, *et al.* *Plasma Phys. Control. Fusion*, vol. 58, p. 105002, 2016.
- [106] F. Militello, B. Dudson, L. Easy, *et al.* *Plasma Phys. Control. Fusion*, vol. 59, p. 125013, 2017.
- [107] G. Q. Yu, S. I. Krasheninnikov, and P. N. Guzdar *Phys. Plasmas*, vol. 13, p. 042508, 2006.
- [108] J. R. Angus and S. I. Krasheninnikov *Phys. Plasmas*, vol. 21, p. 112504, 2014.
- [109] J. R. Angus and M. V. Umansky *Phys. Plasmas*, vol. 21, p. 012514, 2014.
- [110] B. Scott *Plasma Phys. Control. Fusion*, vol. 39, p. 1635, 1997.
- [111] B. Scott *Phys. Rev. Lett.*, vol. 65, p. 3289, 1990.
- [112] P. J. Catto, A. M. Nadi, C. S. Liu, *et al.* *Nucl. Fusion*, vol. 14, p. 405, 1974.
- [113] A. Hasegawa and L. Chen *Phys. Fluids*, vol. 19, p. 1924, 1976.
- [114] A. Hasegawa *Proc. Indian Acad. Sci*, vol. 86, pp. 151–174, 1977.
- [115] W. Gekelman, P. Pribyl, J. Lucky, *et al.* *Rev. Sci. Instrum.*, vol. 87, p. 025105, 2018.
- [116] P. Popovich, M. V. Umansky, T. Carter, *et al.* *Phys. of Plasmas*, vol. 17, p. 122312, 2010.
- [117] D. Pace, *Spontaneous Thermal Waves and Exponential Spectra Associated with a Filamentary Pressure Structure in a Magnetized Plasma*. dissertation, University of California, 2009.
- [118] B. Friedman, *Simulation Analysis of Zero Mean Flow Edge Turbulence in LAPD*. dissertation, University of California, 2013.

- [119] T. A. Carter and J. E. Maggs *Phys. of Plasmas*, vol. 16, p. 012304, 2009.
- [120] J. Leddy, B. Dudson, and H. Willett *Nucl. Mater. Energy*, vol. 12, pp. 994–998, 2017.
- [121] M. Shashkov and S. Steinberg *J. Comput. Phys.*, vol. 118, pp. 117–131, 1995.
- [122] M. Shashkov, *Conservative Finite-Difference Methods on General Grids*. CRC Press, 1996.
- [123] P. J. McCarthy *Phys. Plasmas*, vol. 6, p. 35543560, 1999.
- [124] A. Lebschy, R. M. McDermott, C. Angioni, *et al.* *Nucl. Fusion*, vol. 58, p. 026013, 2017.
- [125] P. W. Terry *Rev. Mod. Phys.*, vol. 72, pp. 0034–6861, 2000.
- [126] R. Mittal and G. Laccarino *Rev. Fluid Mech.*, vol. 37, pp. 239–261, 2005.
- [127] B. Zhu, M. Francisquez, and B. N. Rogers *Comput. Phys. Commun.*, 2018.
- [128] B. LaBombard, M. V. Umansky, R. L. Boivin, *et al.* *Nucl. Fusion*, vol. 40, p. 2041, 2000.
- [129] F. Riva, C. Colin, J. Denis, *et al.* *Plasma Phys. Control. Fusion*, vol. 58, p. 044005, 2016.
- [130] A. N. Simakov and P. J. Catto *Phys. Plasmas*, vol. 10, p. 4744, 2003.
- [131] D. A. Russell, D. A. D'Ippolito, and J. R. Myra *B. Am. Phys. So., 54th Annual Meeting of the APS Division of Plasma Physics*, vol. 57, 2012.
- [132] J. Olsen, J. Madsen, A. H. Nielsen, *et al.* *Plasma Phys. Control. Fusion*, vol. 58, p. 044011, 2016.
- [133] D. A. Russell, D. A. D'Ippolito, and J. R. Myra *B. Am. Phys. So., 54th Annual Meeting of the APS Division of Plasma Physics*, vol. 57, 2012.
- [134] K. Bodi, G. Ciruolo, F. Schwander, *et al.* *38th EPS Conference on Plasma Physics*, 2011.
- [135] J. D. Lawson *Proc. Phys. Soc.*, vol. 70, p. 6, 1957.
- [136] F. Jeffrey, *Plasma Physics and Fusion Energy*. Cambridge University Press, 2007.

-
- [137] C. L. Woods, *Theory of Tokamak Transport: New Aspects for Nuclear Fusion Reactor Design*. Wiley, 2006.
- [138] W. Weymiens, H. J. Blank, G. M. D. Hogeweij, *et al.* *Phys. of Plasmas*, vol. 19, p. 072309, 2012.
- [139] S. Ku, C. S. Chang, R. Hager, *et al.* *Phys. of Plasmas*, vol. 25, p. 056107, 2018.
- [140] A. Yoshizawa, S. Itoh, K. Itoh, *et al.* *Plasma Phys. Control. Fusion*, vol. 43, p. R1, 2001.
- [141] M. Greenwald *Plasma Phys. Control. Fusion*, vol. 44, pp. R27–R80, 2002.
- [142] Y. H. Xu, S. Jachmich, and R. R. Weynants *Plasma Phys. Control. Fusion*, vol. 47, p. 1841, 2005.
- [143] M. Ottaviani *Phys. Lett. A*, vol. 375, p. 1677, 2011.
- [144] G. Q. Yu, S. I. Krasheninnikov, and P. N. Guzdar *Phys. Plasmas*, vol. 13, p. 042508, 2006.